

# Searches for Non-Resonant New Physics in the High Energy Dielectron Spectrum with ATLAS at the LHC

Liam Aaron Keall Duguid

Department of Physics,  
Royal Holloway, University of London



A thesis submitted to the University of London for the  
Degree of Doctor of Philosophy

July 1, 2014

# DECLARATION

I confirm that the work presented in this thesis is my own. Where information has been derived from other sources, I confirm that this has been indicated in the document.

Liam Duguid

## Abstract

Presented is a search in the high mass dielectron spectrum for beyond the Standard Model physics exhibiting a non resonant behaviour. The new physics, four fermion contact interactions and the ADD model with large extra dimensions, are searched for with the ATLAS detector using proton-proton collisions from the Large Hadron Collider at CERN. Results from two data sets are presented, the main results presented come from a data set with  $\sqrt{s} = 8$  TeV and an integrated luminosity of  $20.3 \text{ fb}^{-1}$ , these results are compared to a data set with  $\sqrt{s} = 7$  TeV and an integrated luminosity of  $4.9 \text{ fb}^{-1}$  completed prior. The main analysis completed a search in the dielectron invariant mass distribution as well as the angular variable  $\cos\theta^*$ , while the 7 TeV analysis searched in the dielectron invariant mass.

No significant signal is found in either data set and so lower limits are set on the scale of new physics for several formalisms of each model. For the 7 TeV analysis limits on the scale of new contact interactions ( $\Lambda$ ) are set for the bench mark formalism of LL contact interactions of  $\Lambda > 12.7$  TeV and  $\Lambda > 9.63$  TeV for the model for constructive and destructive interference with the Drell-Yan background respectively. In the same analysis limits are set on the ADD model scale of new physics ( $M_S$ ) of  $M_S > 3.0$  TeV on the benchmark formalism GRW.

The 8 TeV analysis sets higher limits on the LL formalism of  $\Lambda > 21.55$  TeV and  $\Lambda > 19.61$  TeV for constructive and destructive interference. Limits are also set on other formalisms with the highest limits set on the LR formalism of  $\Lambda > 26.25$  TeV and  $\Lambda > 23.77$  TeV for constructive and destructive interference. Limits are set on the ADD GRW formalism of  $M_S > 4.79$  TeV with limits on other formalisms also presented. At the time of writing these are the highest public limits set on either theoretical models.

## **Acknowledgements**

First I would like to thank my supervisor Dr Tracey Berry for her support and guidance throughout my PhD and for always aiming to get the best from and for me.

I would like to thank the Science and Technology Facilities Council (STFC) for their financial support throughout my PhD along with Royal Holloway for the organisation and funding of my time working at CERN.

I must also thank the other staff within the Royal Holloway ATLAS group; Prof Pedro Teixeira-Dias, Prof Glen Cowan and Dr Veronique Boisvert for their advice and questions throughout my PhD. I would like to thank everyone within the office at Royal Holloway throughout my years there for always answering and discussing problems and contributing heavily to the success of my work. Particularly I would thank both Daniel Hayden and Graham Savage with whom I worked closely during their time at Royal Holloway.

I would also like to thank my parents for their support throughout my academic pursuits and always wanting the best for me and the freedom to choose what interested me most.

Last but by no means least I would like to thank Natasha for putting up with me throughout my PhD, for making all the trips out to Geneva so we could be together and for supporting me while I remained a student. I love you and I'm glad to tell you I'm now finished.

---

# Contents

<b>Abstract</b>	<b>3</b>
<b>Acknowledgements</b>	<b>4</b>
<b>Contents</b>	<b>5</b>
<b>Preface</b>	<b>8</b>
<b>1 Theory</b>	<b>12</b>
1.1 Standard Model . . . . .	12
1.1.1 Fundamental Forces . . . . .	14
1.2 Non-resonant New Physics . . . . .	18
1.2.1 Contact Interaction Theory . . . . .	18
1.2.2 ADD Theory . . . . .	21
1.3 Past Searches . . . . .	24
<b>2 Experiment</b>	<b>26</b>
2.1 The Large Hadron Collider . . . . .	26
2.2 ATLAS - A Toroidal LHC Apparatus . . . . .	29
2.2.1 Inner Detector . . . . .	30
2.2.2 Calorimeters . . . . .	33
2.2.3 Magnet System . . . . .	35
2.2.4 Muon Spectrometer . . . . .	37
<b>3 The Trigger &amp; Data Acquisition</b>	<b>39</b>
3.1 Level-1 Trigger . . . . .	40

3.2	Higher Level Trigger . . . . .	42
3.3	Data Acquisition . . . . .	43
3.4	Trigger Menu and Rates . . . . .	45
3.4.1	The “ $e/\gamma$ ” Trigger Menu . . . . .	46
3.4.2	Trigger Rates in High Luminosity Regime . . . . .	47
<b>4</b>	<b>Event Reconstruction</b>	<b>50</b>
4.1	Electron Reconstruction and Identification . . . . .	51
<b>5</b>	<b>Event Selection</b>	<b>54</b>
5.1	Analysis Selection . . . . .	54
5.2	Isolation Requirement . . . . .	55
5.3	Opposite Sign requirement . . . . .	57
5.4	Energy Scale Correction . . . . .	58
5.5	Selection Acceptance $\times$ Efficiency . . . . .	58
<b>6</b>	<b>Background Estimate</b>	<b>61</b>
6.1	Monte Carlo samples . . . . .	62
6.1.1	MC Corrections . . . . .	63
6.2	Fake Factor Multi-Jet Estimate . . . . .	64
6.2.1	Real Electron Efficiency Estimation . . . . .	67
6.2.2	Fake Electron Rate Estimation . . . . .	67
6.2.3	Properties of Multi-Jet Background . . . . .	68
6.2.4	Other Methods and Estimation of Error . . . . .	69
6.3	Total Background Estimate . . . . .	70
<b>7</b>	<b>Signal and Results</b>	<b>71</b>
7.1	Signal Monte Carlo . . . . .	71
7.2	Signal Parametrisation . . . . .	72
7.3	Results . . . . .	73
<b>8</b>	<b>Statistical Analysis</b>	<b>81</b>
8.1	Systematics . . . . .	83

8.2	Angular Analysis Optimisation . . . . .	85
8.2.1	Effect of the Opposite Sign Requirement on Analysis Reach . . . . .	85
8.2.2	Optimisation of Search Bins in $\cos\theta^*$ . . . . .	86
8.3	Signal Search & $p$ -Values . . . . .	86
8.4	Setting Limits . . . . .	87
8.5	Combination with the Muon Search . . . . .	88
<b>9</b>	<b>Non-Resonant 7 TeV Analysis</b>	<b>93</b>
9.1	Data and Background Processes . . . . .	93
9.2	Electron Identification and Selection . . . . .	95
9.2.1	Data and Background Comparison . . . . .	97
9.2.2	New Physics Signal Expectation . . . . .	98
9.3	Statistical Analysis . . . . .	101
<b>10</b>	<b>Conclusion</b>	<b>103</b>
10.1	Looking Forward . . . . .	104
	<b>Appendices</b>	<b>105</b>
<b>A</b>	<b>Extra Results &amp; Control Plots</b>	<b>106</b>
<b>B</b>	<b>Signal Parametrisations</b>	<b>111</b>
<b>C</b>	<b>Statistical Analysis Plots</b>	<b>124</b>
	<b>Bibliography</b>	<b>140</b>

---

# Preface

This thesis describes the work carried out for an analysis searching for new non-resonant physics with the ATLAS detector. It focuses on the search within the electron decay channel using ATLAS's 8 TeV data set. This is compared and contrasted with the previous ATLAS search using the 7 TeV data set in chapter 9 showing the evolution from this previous analysis. For the 7 TeV analysis the author was the only electron channel analyst while they were one of two analysts for the 8 TeV analysis. The author made a major contribution to these two analyses that are detailed in the 7 TeV [1] and 8 TeV [2] publications. The 8 TeV non-resonant analysis discussed in this thesis was primarily carried out within a group of four students, one researcher and four academics working on ATLAS. The search within the electron channel was primarily carried out by two students with the author focusing on the Contact Interaction model and necessarily this dictates the focus on this model within this thesis. Both theoretical models (Contact Interactions and ADD) are presented however as the search methods strongly complement each other and the comparison is seen as important. The author also aided in another analysis contributing to a 7 TeV [3] and an 8 TeV [4] publication searching for new resonant physics in the dilepton channel. This resonant analysis has strong ties with the analysis presented here and the author worked on the dielectron analysis for both. The author also made a major contribution to work in the electron photon triggering group detailed in section 3.4.2. This work composed part of an ATLAS note [5] with the author presenting a related poster [6] at the Computing High Energy Particle physics conference (CHEP) in 2012 in New York. The author's service task on ATLAS was composed of this work and maintenance of the associated high level trigger code.

Following is an overview of this thesis describing the contents of each chapter. Chapters 1 to 4 contain background to the theory and the ATLAS experiment and do not contain work



carried out by the author apart from a section on trigger rates at high luminosity referenced above. Chapters 5 to 11 detail analysis work carried out by the author where related work not completed by the author has been indicated. The thesis is followed by an appendix containing additional material and information not contained in the body of the thesis.

- **Chapter 1: Theory**

This chapter covers an overview of the Standard Model (SM) of particle physics and then continues on to Beyond the Standard Model (BSM) phenomena. The main focus is on the idea of non-resonant excesses in the dilepton Drell-Yan (DY) spectrum of which two examples are discussed. The first example is Contact Interactions, a model which describes many BSM phenomena that can show as four fermion contact interaction that exhibit a divergence from the SM DY spectrum. The example shown is that of a quark-lepton composite model where quarks and leptons are found to be composed of smaller particles. The second example given is the Arkani-Hamed, Dimopoulos, and Dvali (ADD) model. This is a Graviton theory with the addition of large extra spacial dimensions to dilute gravity. These large extra spacial dimensions create Kaluza-Klein resonances of the graviton very close to each other and so exhibit signs of non-resonance behaviour. A look at past results for similar searches is also discussed here.

- **Chapter 2: Experiment**

This chapter is an overview of the ATLAS experiment and the LHC with important detector and LHC components discussed. A particular focus is given to the inner tracking detector and energy calorimeters of ATLAS as these systems are the parts used in the detection of di-electron events used in this analysis.

- **Chapter 3: The Trigger & Data Acquisition**

This chapter focuses on the triggering system for selecting data events in the ATLAS detector. An overview of the whole system will be given but a focus made on the “egamma” trigger which selects electron and photon events. A slight detour will be made discussing the effect of increases in the luminosity of the LHC collisions through the 2011-2012 data-taking period and efforts taken to reduce high rates of data acquisition this led to in the “egamma” chain.

- **Chapter 4: Event Reconstruction**

This chapter details the algorithms used in reconstructing electrons and photons from the detector output. It also contains a discussion on ATLAS assignments of *tight*, *medium* and *loose* electrons.

- **Chapter 5: Event Selection**

This chapter covers the main event selection of di-electron events for the non-resonance analysis using the  $20\text{ fb}^{-1}$  recorded in 2012. There is also a discussion of the necessary corrections applied to energy measurements.

- **Chapter 6: Background Estimate**

This chapter discusses the estimate of the background processes to the non-resonant signal. It covers the Monte Carlo (MC) samples generated to estimate these backgrounds as well as corrections applied to match MC to the data collection conditions used and corrections to account for next to next to leading order generator effects.

- **Chapter 7: Signal and Results**

This chapter shows the search for new physics in the data collected in the 2012 data taking period. This includes a description of the MC used to predict the signals as well as comparison between the Data and the MC prediction of the background. Also looked at are the significance or  $p$ -value of any divergences from the SM background prediction.

- **Chapter 8: Statistical Analysis**

This chapter discusses the statistical treatment of the results. First discussed is possible sources of systematic error in the analysis as well as levels of statistical error. Then there is a look at the complications introduced with the angular analysis in  $\cos\theta^*$ . Last a Bayesian approach is taken to search for signs of new physics and then setting lower limits on the scale of new physics predicted by this analysis.

- **Chapter 9: Non-Resonance 7 TeV Analysis**

This chapter looks at the first non-resonant analysis completed on the 7 TeV data set from 2011 with a luminosity of  $4.9\text{ fb}^{-1}$ . An overview of the full event selection and limits set are included along with some comparisons between this and the 8 TeV

analysis. This analysis is presented after the 8 TeV analysis as a comparison to show the evolution of the analysis and highlight the authors work.

- **Chapter 10: Conclusion**

This final chapter discusses the conclusions obtained from this analysis with an overview of the results and a comparison between the limits set and previous results. Finally there is a look forward to the future of searches of non-resonant physics within ATLAS and the LHC.

---

# Chapter 1

## Theory

The Standard Model (SM) of particle physics has proven excellent at describing particle interactions up to the energy scale of modern colliders ( $\sim \text{TeV}$ ) and with the discovery of a Standard Model like Higgs Boson at the Large Hadron Collider (LHC) the theory will be able to claim completeness up to the energy scale of modern colliders. However the Standard Model is known to be incomplete, with observations such as neutrino mass, the lack of anti-matter in the observable universe and the lack of a quantum gravity description with the related hierarchy problem<sup>1</sup>, the Standard Model is far from a theory of Everything. This then leaves the possibility of new physics beyond the SM that could appear in the energy scope of the LHC. Following is an overview of the Standard Model [7] followed by a description of the theoretical models searched for in this thesis.

### 1.1 Standard Model

The Standard Model of particle physics is a quantum field theory describing the interaction of particles and forces at a fundamental level. These forces and particles are so far seen to be the most fundamental components in nature describing all known quantum systems but with the absence of gravity. Particles are split between fermions, the matter particles, and gauge bosons, the force carriers in the model. There is also the additional scalar boson the Higgs, discussed later. The gauge bosons are split between the three fundamental forces Strong, Weak and Electromagnetic while the fermions are split in to two different categories

---

<sup>1</sup>The hierarchy problem highlights the drastic difference in force strength between gravity and the other fundamental forces seen in the Standard Model.

leptons and quarks according to which forces they interact with. Fermions have the property of having spin 1/2 while bosons have an integer spin of either 0 or 1. Each particle has an associated anti-particle with opposite charge.

## Leptons

Leptons only interact with other particles via the electromagnetic and weak forces with neutrinos only interacting via the weak force. There are 6 leptons in total organised in to 3 flavours, the electron (e), muon ( $\mu$ ) and tau ( $\tau$ ) as well as the neutrinos, electron neutrino ( $\nu_e$ ), muon neutrino ( $\nu_\mu$ ) and tau neutrino ( $\nu_\tau$ ). All the leptons along with their mass and charge can be seen in table 1.1. It is important to note that the standard model predicts neutrinos to be massless while experiment has proven neutrinos to have mass via observations of neutrino oscillations between flavours.

Charge ( $q$ )	Generation		
	I	II	III
-1	electron <b>e</b> $m = 0.51 \text{ MeV}$	muon <b><math>\mu</math></b> $m = 105.7 \text{ MeV}$	tau <b><math>\tau</math></b> $m = 1.777 \text{ GeV}$
0	electron neutrino <b><math>\nu_e</math></b> $m < 2.2 \text{ eV}$	muon neutrino <b><math>\nu_\mu</math></b> $m < 0.17 \text{ MeV}$	tau neutrino <b><math>\nu_\tau</math></b> $m < 15.5 \text{ MeV}$

Table 1.1: The leptons found in the Standard Model.

## Quarks

Quarks interact with other particles via all three forces electromagnetic, weak and strong. Again there are 6 quarks organised in to 3 flavours: up (u), down (d), charm (c), strange (s), top (t) and bottom (b). The charge and mass of the six quarks is shown in table 1.2. Quarks also come with a property called colour charge important in how the strong interaction works. The strong force leads to the property called colour confinement found in quarks causing quarks to hadronise quickly with only colour neutral particles seen. These colour neutral or “colourless” particles referred to as hadrons are composed of quarks and come in two configurations baryons and mesons with three and two quarks each respectively.

Protons and neutrons are baryons containing the quark configurations uud and udd which appear within the nucleus of atoms. Many other configurations of quarks form different baryons but none are stable. Mesons are composed of one quark and one anti-quark but none are found to be stable in nature.

Charge ( $q$ )	Generation		
	I	II	III
$+\frac{2}{3}$	up quark <b>u</b> $m \approx 2.3 \text{ MeV}$	charm quark <b>c</b> $m \approx 1.275 \text{ GeV}$	top quark <b>t</b> $m \approx 173.07 \text{ GeV}$
$-\frac{1}{3}$	down quark <b>d</b> $m \approx 4.8 \text{ MeV}$	strange quark <b>s</b> $m \approx 95 \text{ MeV}$	bottom quark <b>b</b> $m \approx 4.18 \text{ GeV}$

Table 1.2: The quarks found in the Standard Model.

## Gauge Bosons

There are 4 bosons in the Standard Model as well as the newly observed candidate for the fifth the Higgs Boson. The Higgs boson is discussed later but for now we will look at the force carriers or gauge bosons. The gauge bosons consist of the gluon ( $g$ ) carrier of the strong force, the photon ( $\gamma$ ) carrier of the electromagnetic force and then the W and Z bosons carriers of the weak force. All gauge bosons have a spin of 1 with only the W boson having a electric charge and therefore the only particle with a distinguishable particle and antiparticle. All gauge bosons and their properties can be seen in table 1.3.

### 1.1.1 Fundamental Forces

The Standard Model is described as a local gauge theory meaning observables remain unchanged under transformations be they global transformations, a uniform transformation over all space and time, or local transformations, a transformation as a function of space and time. This is also described as gauge symmetry or gauge invariance and held as an important trait for quantum field theories to possess. The first fundamental force to gain a gauge theory was Quantum Electrodynamics with the U(1) symmetry referring to a theory

Force	Charge	Boson
Electromagnetic	0	photon $\gamma$ $m = 0$
Weak	0	Z boson $Z$ $m = 91.2 \text{ GeV}$
	$\pm 1$	W boson $W$ $m = 80.4 \text{ GeV}$
Strong	0	gluon $g$ $m = 0$

Table 1.3: The gauge bosons found in the Standard Model.

symmetric under unitary  $1 \times 1$  group transformations. The weak theory and Quantum Chromodynamics followed with symmetries of SU(2) and SU(3) transformations respectively. SU(n) refers to a group of  $n \times n$  special unitary matrices (Special refers to the matrices all having a determinant of 1). This is why the SM is referred to as a  $U(1) \times SU(2) \times SU(3)$  group theory after the unification of the forces.

### Quantum Electrodynamics

Quantum Electrodynamics (QED) describes the interactions of the photon with charged fermions. Photons are massless meaning the electromagnetic force has infinite reach. The theory describes the interaction strength between the photon and both quarks and charged leptons. The quantity conserved in these interactions is particle electric charge. QED is important in calculating the  $qq \rightarrow \gamma \rightarrow \ell\ell$  process which is a main background to this analysis in the form of Drell-Yan. The photon has no charge so there are no self interactions between photons. The fundamental QED interaction vertex can be seen figure 1.1.

### The Weak Interaction

The Weak interaction describes interactions involving the neutral  $Z^0$  boson and the charged  $W^\pm$  boson. These bosons both have mass limiting the range of the weak interaction. This theory allows for the interaction between all fermions including neutrinos (which only in-

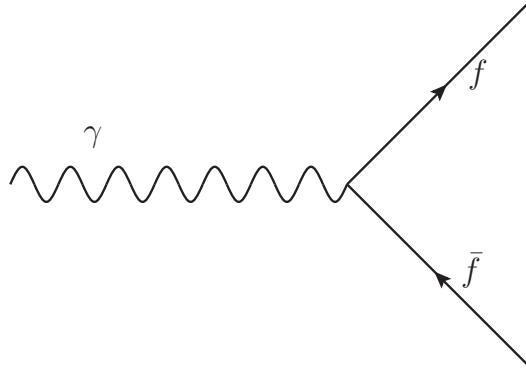


Figure 1.1: Fundamental QED interaction vertex, where  $f$  can be any charged fermion.

interact via the weak force) and self interaction between  $Z$  and  $W$  bosons. This is important for this analysis because of the diboson background to signal consisting of production of  $ZZ$   $WZ$  and  $WW$  events decaying to electrons as well a simple  $Z$  boson decaying to two electrons. The fundamental weak interaction vertices can be seen in figure 1.2.

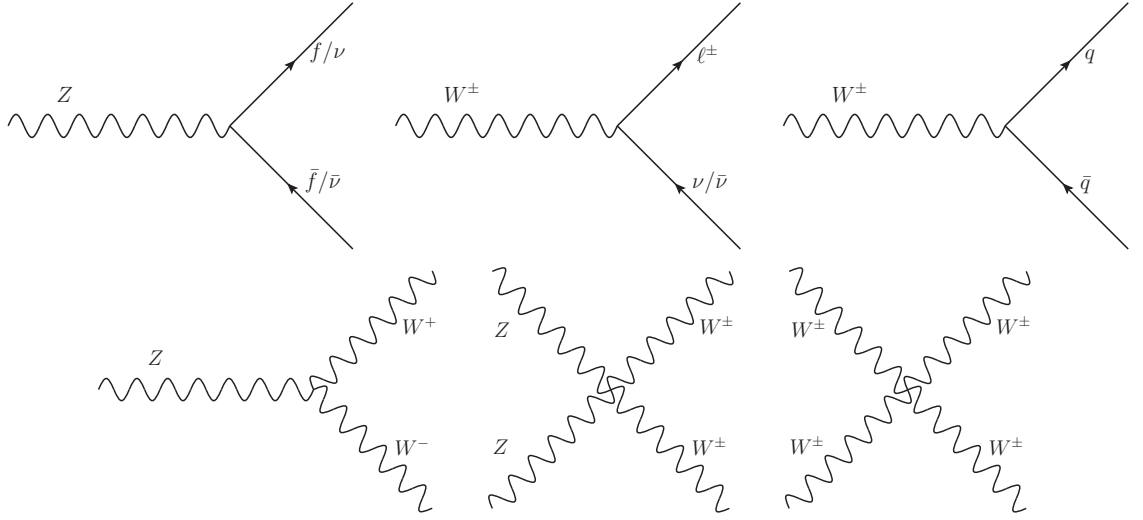


Figure 1.2: Fundamental weak interaction vertices, where  $f$  can be any charged fermion,  $\ell$  can be any charged lepton and  $q$  can be any quark as long as charge is conserved in each case.

### Electroweak Unification & Symmetry Breaking

The electromagnetic and weak theories were united by Glashow, Weinberg and Salam [8, 9, 10] showing that at high energy (past the electroweak unification/phase transition energy  $\sim 246$  GeV) the forces can be considered as one and conserves a combined quantum number,



weak hypercharge  $Y = 2(Q - I_3)$  where  $I_3$  is the weak isospin and  $Q$  is the electric charge. This combination of the forces is the  $U(1) \times SU(2)$  symmetry. This conserved symmetry then gives rise to 4 gauge fields  $W^1$ ,  $W^2$ ,  $W^3$  and  $B^0$ . The first three originating from symmetries in  $SU(2)$  and the last from  $U(1)$ . The gauge bosons we observe in experiment are then obtained by a mixing of these gauge fields as found in equations 1.1 and 1.2 where  $\cos \theta_w = m_W/m_Z$ .

$$W^\pm = \frac{W^1 \mp iW^2}{\sqrt{2}} \quad (1.1)$$

$$\begin{pmatrix} \gamma \\ Z^0 \end{pmatrix} = \begin{pmatrix} \cos \theta_w & \sin \theta_w \\ -\sin \theta_w & \cos \theta_w \end{pmatrix} \begin{pmatrix} B^0 \\ W^3 \end{pmatrix} \quad (1.2)$$

However electroweak unification alone causes a problem by predicting W and Z bosons as massless contradicting experimental results and implying electroweak symmetry must be broken. The solution to this problem comes about by the introduction of the Higgs mechanism [11, 12, 13]. The Higgs mechanism makes the prediction of a new complex doublet of scalar fields referred to as the Higgs field. This Higgs field has a non zero vacuum expectation value allowing symmetry in the  $U(1) \times SU(2)$  group at high energy, however below the electroweak phases transition the Higgs potential has a non zero minima we call the vacuum expectations energy. This induces a spontaneous symmetry breaking allowing the weak gauge bosons to have mass while photons remain massless. This Higgs field also gives rise to a massive scalar boson referred to as the Higgs boson. A scalar boson fitting the description of the Higgs boson was recently discovered at the two main LHC experiments proving that electroweak symmetry breaking of this form exists [14, 15].

### Quantum Chromodynamics

Quantum Chromodynamics (QCD) is the theory associated with the strong force. It describes a interactions between particles conserving a quantum number called colour. The  $SU(3)$  symmetric group gives rise to 8 massless gauge bosons referred to as gluons. Gluons interact with only coloured particle which include quarks and themselves. The strong interaction is different in the way it strengthens with increasing distance and weakens to asymptotic freedom at small distances. This increase in interaction strength with increasing distance is referred to as colour confinement discussed previously where as quarks separate

the interaction energy increases to the point that  $q\bar{q}$  pairs form combining again to form colourless baryons and mesons. The fundamental QCD interaction vertices can be seen in figure 1.3.

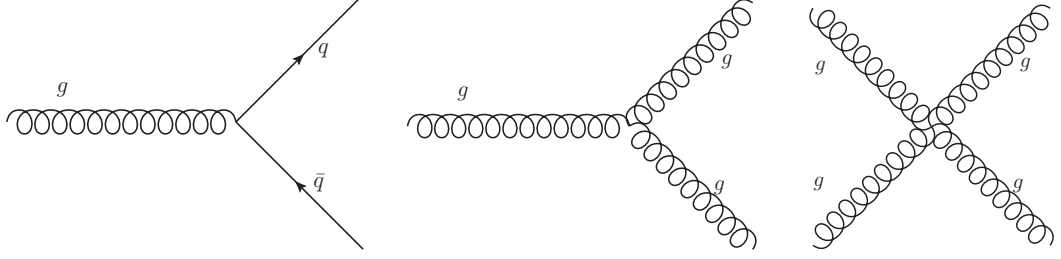


Figure 1.3: Fundamental QCD interaction vertices, where  $q$  can be any quark.

## 1.2 Non-resonant New Physics

Beyond the Standard Model (BSM) or new physics models is a staple of the physics programs of the LHC detectors. Any theoretical models not contained within the Standard Model (SM) can fall in to this category and LHC experiments aim to search for as many of these models as are feasible within their scope (proton-proton collisions and within the energy range of the LHC). Within the detection channel of two lepton decays (dilepton) non-resonant signals could be a signature of new physics. This physics would show as a divergence from the SM background prediction in the dilepton mass spectrum contrasted with resonant signals of particles such as the Z boson which shows as a peak in the dilepton mass spectrum.

Non-resonant signals could be the results of many BSM theoretical models but two main theories are presented here and their searches compose the rest of this thesis.

### 1.2.1 Contact Interaction Theory

The SM assumes quarks and leptons to be fundamental particles in nature. This assumption is not without compelling argument but like the proton beforehand there is no reason quarks and leptons should not be composite structures or bound states of more fundamental particles, often referred to as preons [16], only observable at an energy scale  $\Lambda$  we have yet to reach.

One way quark and lepton compositeness would exhibit itself is in 4-fermion contact interactions between two quarks from the incoming protons producing two final state leptons ( $q\bar{q} \rightarrow \ell^-\ell^+$ ). This is the compositeness signal searched for at the ATLAS detector. As can be seen in the Feynman diagrams in figure 1.4 4-fermion contact interaction are indistinguishable from the main background process Drell-Yan.<sup>2</sup>

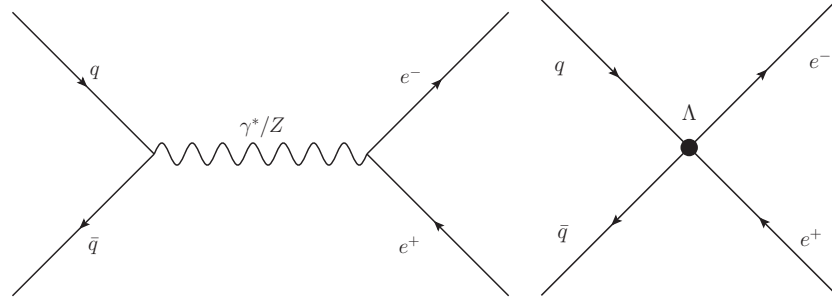


Figure 1.4: Feynman diagrams of the predominant background SM process Drell-Yan (left) and by comparison the contact interaction (right).

Without knowing the intermediate process one can write a Lagrangian describing the new interaction:

$$\mathcal{L} = \frac{g^2}{2\Lambda^2} [\eta_{LL}(\bar{\psi}_L \gamma_\mu \psi_L)(\bar{\psi}_L \gamma^\mu \psi_L) + \eta_{RR}(\bar{\psi}_R \gamma_\mu \psi_R)(\bar{\psi}_R \gamma^\mu \psi_R) + 2\eta_{LR}(\bar{\psi}_L \gamma_\mu \psi_L)(\bar{\psi}_R \gamma^\mu \psi_R)] \quad (1.3)$$

where  $g$  is the coupling constant,  $\Lambda$  is the energy scale of new physics and  $\psi_L$  and  $\psi_R$  are the left and right handed fermionic fields respectively. The sign of  $\eta$  defines whether the new interaction interferes constructively ( $\eta = -1$ ) or destructively ( $\eta = +1$ ) with DY and is always unity. For previous analyses [17, 18, 1] a benchmark model of just the Left-Left (LL) component has been used and is defined by  $\eta_{LL} = \pm 1$  and  $\eta_{RR} = \eta_{LR} = 0$ . This thesis discusses both an analysis searching for only LL (found in chapter 9) and one with an investigation of each of the three parameters (found in the rest of the thesis). Due to the symmetry of left handed and right handed interactions both the LL and RR cases predict similar distributions however the LR case exhibits a different angular dependence than either of the other formalisms or the DY background. This difference is the primary reason for the inclusion of the angular search variables described later in the analysis. The

<sup>2</sup>Drell-Yan (DY) describes of the annihilation of a quark and antiquark forming a virtual photon or Z boson which then decays in to a lepton pair ( $q\bar{q} \rightarrow \gamma^*/Z \rightarrow \ell^-\ell^+$ ).

discriminating variables used are therefore dilepton invariant mass and cosine of the decay angle  $\theta^*$ . The angle  $\theta^*$  is defined in the Collins-Soper frame [19] which is defined with the  $x$ -axis perpendicular to the incoming parton momentum frame and the  $z$ -axis bisecting the angle between the two incoming parton momenta. Since the incoming parton information is understandably unavailable the  $z$ -axis is taken as the direction of the incoming quark (as opposed to anti-quark) obtained from the boost in to the dilepton frame. The angle  $\theta^*$  is then defined as the angle between this  $z$ -axis and the momentum of the outgoing negatively charged lepton (or electron in this analysis).

Figure 1.5 shows the difference expected between the LR CI models and DY background from a truth Monte-Carlo study. The variables used are forward backwards asymmetry ( $A_{FB}$ ) and dilepton invariant mass, where  $A_{FB}$  is defined in relation to  $\cos\theta^*$  as:

$$A_{FB} = \frac{N_F - N_B}{N_F + N_B} \quad (1.4)$$

where  $N_F$  and  $N_B$  are number of events found with  $\cos\theta^*$  greater than 0 and less than 0 respectively.

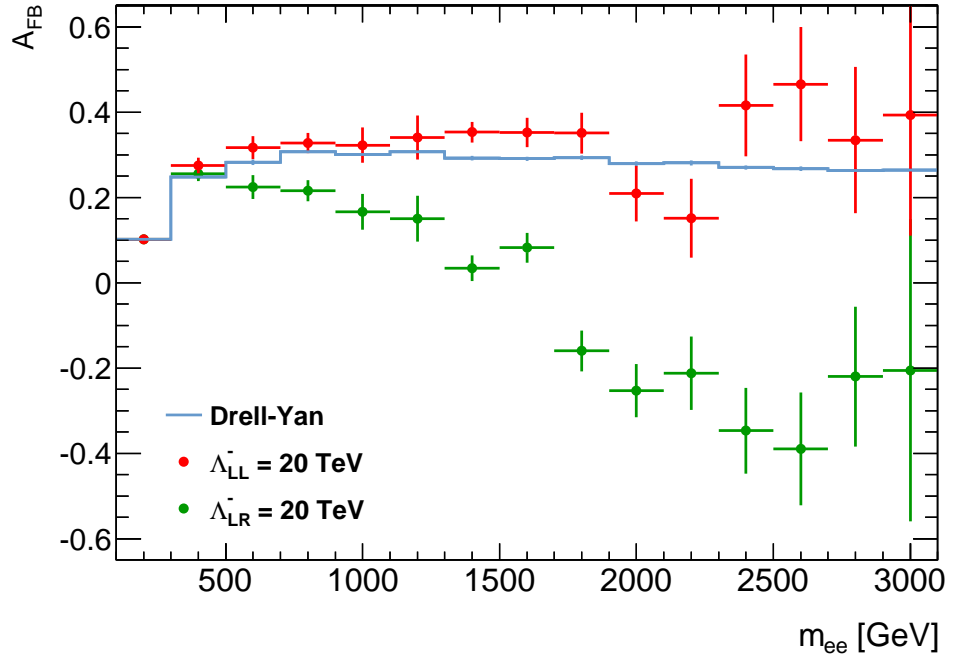


Figure 1.5: Monte-Carlo truth level comparison between the forward backwards asymmetry of DY and of a CI LR signal.

A differential cross section for this interaction,  $q\bar{q} \rightarrow \ell^-\ell^+$  ( $qq\ell\ell$ ), is given by

$$\frac{d\sigma}{dm_{\ell\ell}} = \frac{d\sigma_{DY}}{dm_{\ell\ell}} - \eta \frac{F_I}{\Lambda^2} + \frac{F_C}{\Lambda^4}, \quad (1.5)$$

where  $m_{\ell\ell}$  is the dilepton mass and  $\Lambda$  is the scale of the new physics. In the case of quark/lepton compositeness  $\Lambda$  refers to the point at which fermions stop being bound as SM quarks and leptons.  $F_I$  and  $F_C$  define the interference DY-CI term and the pure CI term respectively. The scale of the interference and pure term vary with both the dilepton invariant mass as well as the scale of new physics  $\Lambda$ .

Experimentally this interaction would be seen as a deviation from the Standard Model Drell-Yan dilepton mass spectrum as seen in figure 1.6.

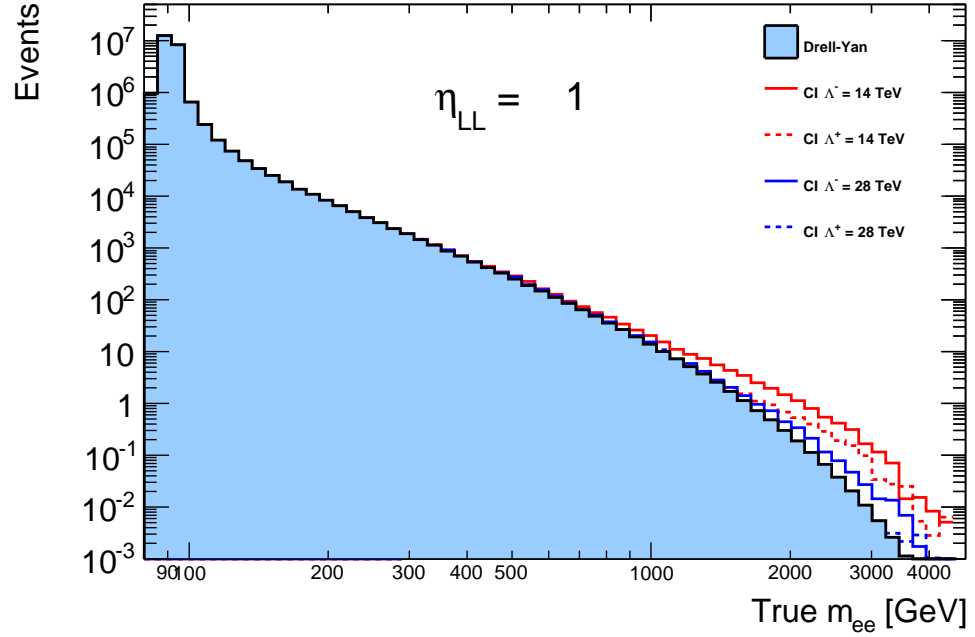


Figure 1.6: Monte-Carlo truth level comparison between DY spectrum with and without CI signal.

### 1.2.2 ADD Theory

Arkani-Hamed, Dimopoulos, and Dvali (ADD) [20] described a model with large extra dimensions proposed to solve the hierarchy problem and bring the energy scale associated with gravity (the Planck scale  $M_{Pl} \sim 10^{16}$  TeV) down to the level of the electroweak energy

scale ( $M_{EM} \sim 10^{-1}$ ). This is achieved with the introduction of  $n$  additional compactified spacial dimensions with radius  $R$ . This then gives a new scale in the  $4+n$  dimensional space,  $M_D$ , which is related to the Planck scale by  $M_{Pl} = M_D^{n+2} R^n$ . If both the radius of the extra dimensions  $R$  and number  $n$  are large enough this solves the hierarchy problem by bringing  $M_D$  down to the level of  $M_{EM}$ . Large extra dimensions are distinct from other extra dimensions theories due to their relatively large radius  $R$ . One version of the ADD model proposes a Graviton that propagates the extra dimensions acquiring Kaluza-Klein (KK) modes that show as a broad excess above the SM background. The Graviton is the only propagator in these extra  $n$  dimensions with each dimension resulting in a new KK mass splitting of the Graviton mass. The mass splitting occurs with an interval of  $1/R$  and since  $R$  is required to be large by the theory this pushes the mass splitting together causing a continuous peak like structure analogous to a non-resonant excess. The sum over these virtual KK modes has to be regularised by an “ultra violet” cutoff ( $\Lambda_T$ ) and it is convention to equate this cutoff to the onset of quantum gravity ( $M_S$ ) only below which the theory is valid. The scale  $M_S$  is used as the scale of new physics for the ADD theory below which ADD is a low energy effective theory. This scale can be related to the new  $n$  dimensional Planck scale ( $M_D$ ) by:

$$M_S = 2 \sqrt{\pi} [\Gamma(n/2)]^{1/(n+2)} M_D \quad (1.6)$$

where  $\Gamma$  is the decay width. Below the scale  $M_S$  virtual Graviton exchange would lead to a broad excess over the SM Drell-Yan dilepton mass spectrum. The Feynman diagrams of this graviton exchange are seen in figure 1.7.

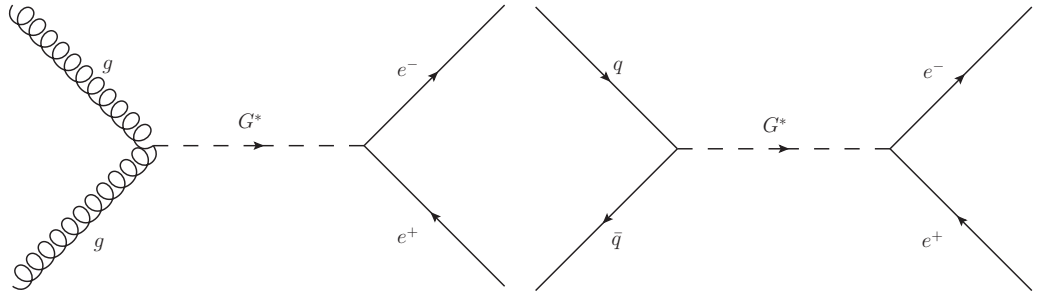


Figure 1.7: Feynman diagrams of Graviton exchange in the ADD theory coming from both gluon (left) and quark (right) annihilation.

The total differential cross-section for the dilepton SM DY and virtual Graviton ex-

change is then:

$$\frac{d\sigma}{dm_{\ell\ell}} = \frac{d\sigma_{DY}}{dm_{\ell\ell}} + \mathcal{F} \frac{F_I}{M_S^4} + \mathcal{F}^2 \frac{F_G}{M_S^8} \quad (1.7)$$

where  $\sigma_{DY}$  is the SM DY cross-section,  $F_I$  and  $F_G$  are the Graviton-DY interactions term and pure virtual Graviton exchange term respectively while  $\mathcal{F}$  is a formalism dependent parameter and also dimensionless. Three formalisms are commonly used to describe ADD theory, these are Giudice, Rattazzi, and Wells (GRW) [21], Han, Lykken, and Zhang (HLZ) [22] and Hewett [23]. Defining  $\mathcal{F}$  these formalisms alter the cross-section of virtual Graviton exchange with HLZ depending on the number of extra dimensions,  $n$ , introduced by the ADD theory. All three formalisms are detailed in equation 1.8

$$\begin{aligned} \mathcal{F} &= 1, & (\text{GRW}) \\ \mathcal{F} &= \begin{cases} \log\left(\frac{M_S^2}{m_{\ell\ell}^2}\right), & (n=2) \\ \frac{2}{n-2}, & (n>2) \end{cases}, & (\text{HLZ}) \\ \mathcal{F} &= \frac{2\lambda}{\pi} = \frac{\pm 2}{\pi}, & (\text{Hewett}) \end{aligned} \quad (1.8)$$

The variable  $\lambda$  found in the Hewett formalism defines the constructive or destructive nature of the gravitational interaction with the SM DY processes.  $\lambda$  is always of order unity with +1 and -1 being constructive and destructive respectively. The GRW and HLZ with  $n=2$  are the two formalisms explicitly searched for in this analysis with a conversion of limits done to assess the other formalisms in the statistical analysis chapter (chapter 8).

It is important to note the differences between this and the Randall Sundrum [24] Graviton model which predicts a Graviton signal as a peak structure at a single mass point due to different spacing of KK towers in the theory.

Experimentally this interaction would be seen as a deviation from the SM DY ( $q\bar{q} \rightarrow \gamma/Z \rightarrow \ell^-\ell^+$ ) dilepton mass spectrum but with a cut-off where quantum gravity is assumed take effect. This can be seen in figure 1.8.

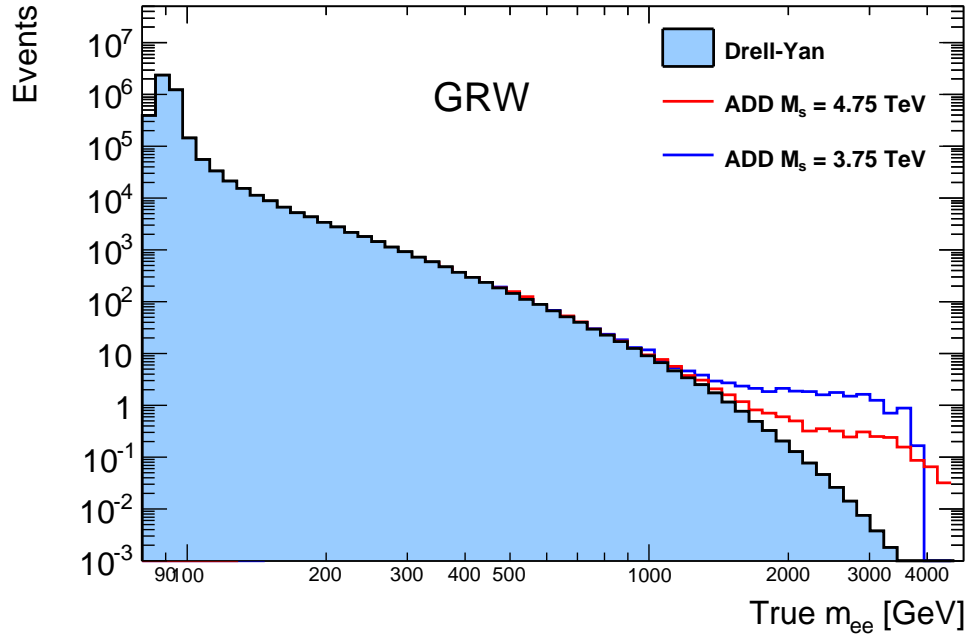


Figure 1.8: MC truth level comparison between DY spectrum with and without ADD signal.

## 1.3 Past Searches

### Contact Interaction

Several previous CI analyses have been done at hadron colliders including the LHC [1, 25, 26, 27] and the Tevatron [17, 18, 28, 29, 30, 31, 32]. Searches were also performed at the electron-proton collider HERA [33, 34, 35], previous lepton colliders [36, 37, 38, 39, 40] and neutrino scattering experiments [41]. Of the results comparable to this analysis searching for  $qq\ell\ell$  contact interactions in the absence of signal the highest limits set on the scale of new physics  $\Lambda$  come from the previous ATLAS analysis the author worked on [1] detailed in chapter 9. This analysis set a limit of  $\Lambda > 12.7$  TeV and  $\Lambda > 9.63$  TeV for the dilepton LL CI model for constructive and destructive interference respectively. The limits obtained for the electron channel for comparison to this analysis were  $\Lambda > 11.6$  TeV for constructive and  $\Lambda > 8.76$  TeV for destructive interference. By comparison the CMS results on the same 2011 data [26] set limits of  $\Lambda > 13.1$  TeV and  $\Lambda > 9.5$  TeV for constructive and destructive isolation. Before the LHC the highest limits on  $qq\ell\ell$  contract interactions came from CDF at the Tevatron [18] (with  $0.45 \text{ fb}^{-1}$  of data) that set limits



on  $qqee$  contact interactions for the LL,  $\Lambda > 5.9$  TeV and  $\Lambda > 3.7$  TeV, RR,  $\Lambda > 5.6$  TeV and  $\Lambda > 3.9$  TeV, and LR formalism,  $\Lambda > 5.8$  TeV and  $\Lambda > 4.7$  TeV, for constructive and destructive interference respectively.

## ADD

The highest dilepton ADD limits set on the formalism normally used as a benchmark, GRW, are that of the previous ATLAS analysis on which the author worked [1] discussed in chapter 9. This analysis set a limit of  $M_S > 3.0$  TeV on the scale of new physics ( $M_S$ ). Other previous analyses have also been carried out searches for large extra dimensions with the ADD model. These analyses have come from the LHC [1, 42, 43, 44], from the Tevatron [45, 46, 17], as well as from electron-proton collider HERA [34, 33] and electron-positron collider LEP [47, 48, 49, 50, 31, 32]. The highest limit before the LHC were those set by D0 on the Tevatron [45] which set limits of  $M_S > 1.45$  TeV on the GRW model in the electron and photon channels.

---

## Chapter 2

# Experiment

This chapter will explore the ATLAS experiment in order to explain how data specific to this analysis is obtained. First however is a discussion of the Large Hadron Collider which supplies the ATLAS experiment with proton collisions.

### 2.1 The Large Hadron Collider

The Large Hadron Collider (LHC) [52] is the largest and most powerful particle collider in the world with a circumference of 27 km and design centre of mass collision energy of 14 TeV. During the 2012 run the accelerator was run at a centre of mass energy of 8 TeV while providing an integrated luminosity of just above  $20 \text{ fb}^{-1}$  throughout the year to its two general purpose experiments, CMS and ATLAS, that latter of which provided data for this analysis. An analysis is also presented in this thesis looking at the 7 TeV data set from the 2011 run. This data set provided just above  $4.5 \text{ fb}^{-1}$  of data. Figure 2.2 shows the luminosity collected throughout the the 2011-2012 period.

The LHC itself is built in the same tunnel (see figure 2.1) as was used by the Large Electron-Positron (LEP) collider. Based at CERN (Centre of European Nuclear Research) the 27 km tunnel is between 50 to 175 m underground and like CERN itself crosses the French-Swiss border just outside Geneva. Construction of the LHC started in 2001 after the LEP collider was decommissioned and dismantled with excavation of the caverns for the LHC's four main experiments starting slightly before in 1998. The LHC is a synchrotron machine requiring 1,232 super-conducting Niobium-Titanium dipole magnets each provid-

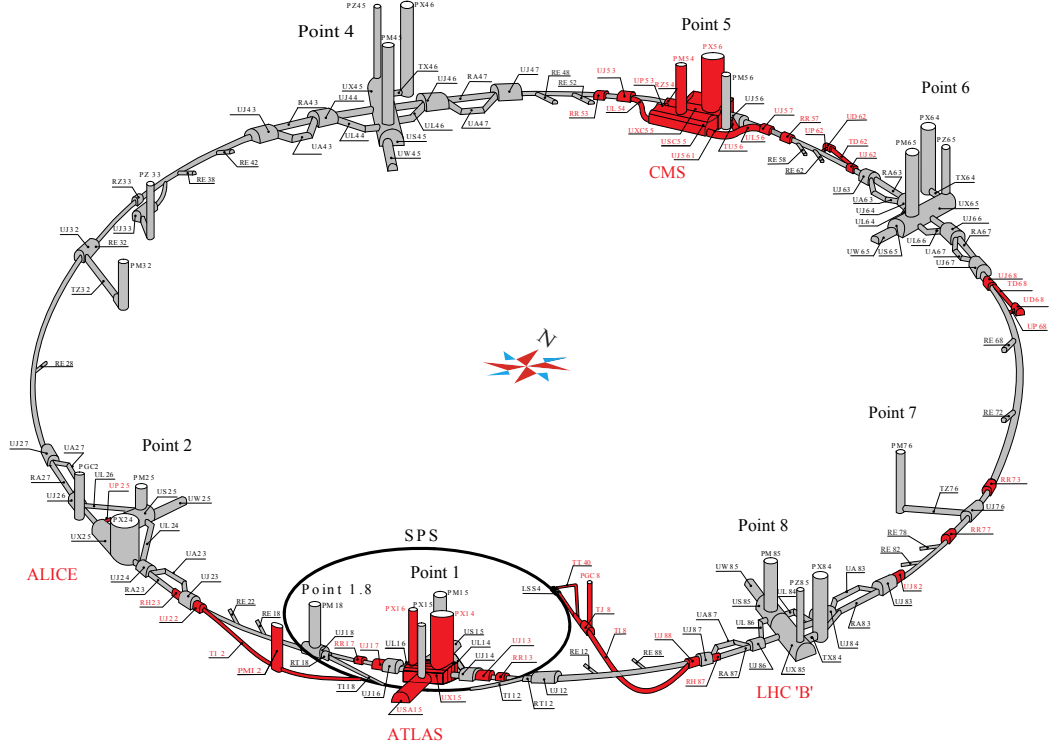


Figure 2.1: Schematic of LHC tunnel with all its caverns showing those added in preparation for the LHC. This shows the position of the LHC's 4 main detectors and SPS ring [51].

ing an 8.33 T magnetic field to direct the proton beams around its loop and an additional 392 quadrupole magnets of the same type to focus the beams for the collision points. The superconducting magnets operate at 1.9 K with the whole accelerator requiring 96 tonnes of liquid helium to remain cooled.

For the 8 TeV run the LHC ran with 1380 proton bunches travelling in each direction which were accelerated around the LHC with an interval of 50 ns between bunches and with each bunch composed of  $\sim 1.15 \times 10^{11}$  protons. These run conditions gave a peak instantaneous luminosity of  $6.6 \times 10^{33} \text{cm}^{-2} \text{s}^{-1}$  at the start of a run which slowly degraded during a run as protons collided. The 7 TeV run had a peak instantaneous luminosity of  $3.6 \times 10^{33} \text{cm}^{-2} \text{s}^{-1}$

However the LHC can not run in isolation to provide beams for its 4 main experiments, instead it is the last and newest accelerator in a chain of accelerators which extract protons from a hydrogen canister with little to no momentum and inject them in to the LHC as a 450 GeV beam. The proton source is a device called a Duoplasmatron which injects hydrogen gas in to a strong electric field stripping electrons from their nuclei. The remaining

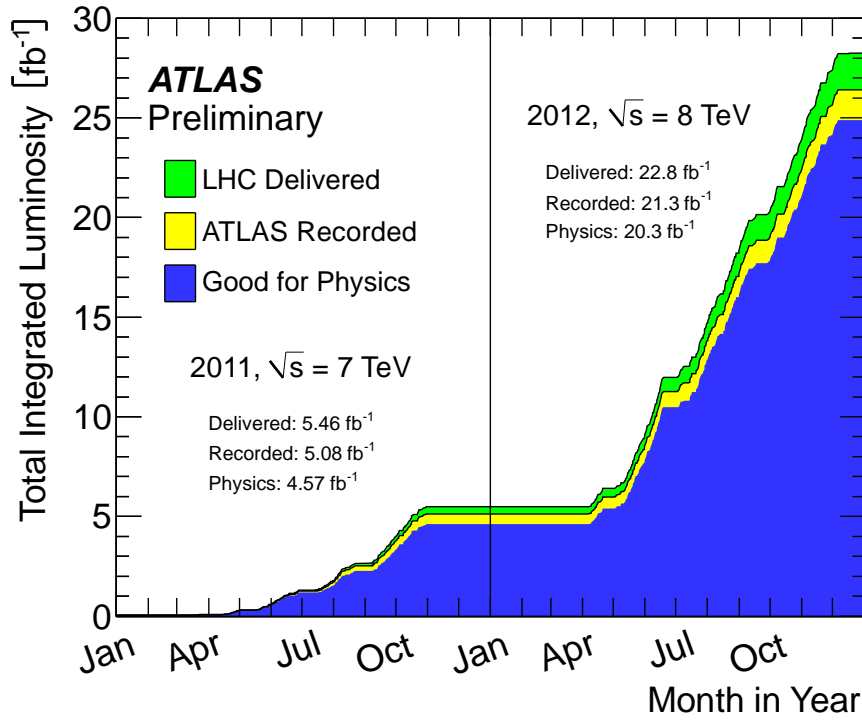


Figure 2.2: Cumulative luminosity versus time delivered to (green), recorded by ATLAS (yellow), and certified to be good quality data (blue) during stable beams and for pp collisions at 7 and 8 TeV centre-of-mass energy in 2011 and 2012. [53]

protons are injected in to Linac 2, a linear accelerator which accelerates them to an energy of 50 MeV. The BOOSTER or Proton Synchrotron Booster (PBS) comes next in the chain and accelerates protons from 50 MeV to 1.4 GeV to be injected in to the main Proton Synchrotron (PS). The PS accelerates protons up to an energy of 25 GeV and again injects them in to another accelerator, the Super Proton Synchrotron (SPS). The SPS (seen in figure 2.1) is the final stage before injection in to the LHC ring and pushes protons to an energy of 450 GeV. Protons from the SPS then get injected in to the LHC in both counter revolving directions and accelerated to their final collision energy. For the data used in the analysis the final proton beam energy is 3.5 TeV and 4 TeV for the 2011 and 2012 runs giving a final centre of mass collision energy of 7 TeV and 8 TeV respectively.

Four collision points exist around the circumference of the LHC providing collisions to the four main experiments (see figure 2.1); ATLAS (A Toroidal LHC Apparatus), CMS (Compact Muon Solenoid), ALICE (A Large Ion Collider Experiment) and LHCb (Large Hadron Collider beauty). ATLAS and CMS are both general purpose experiments designed

to look for a variety of physics. ALICE is designed specifically to study quark-gluon plasma in heavy ion collisions scheduled for the end of each LHC run period while LHCb looks for beauty mesons in searches for CP-violation. There are also three additional LHC detectors in various stages of deployment without their own collision points; TOTEM (Total Elastic and diffractive cross-section Measurement), LHCf (LHC forward) and MoEDAL (Monopole and Exotics Detector at the LHC) which measure separate beam properties. TOTEM shares CMS's collision point aiming to measure the proton cross-section very accurately while LHCf shares ATLAS's collision point measuring the very forward region of collision with the hope of investigating the source of ultra-high-energy cosmic rays. MoEDAL shares a cavern with LHCb and is targeted to search for magnetic monopoles and other highly ionising stable massive particles.

## 2.2 ATLAS - A Toroidal LHC Apparatus

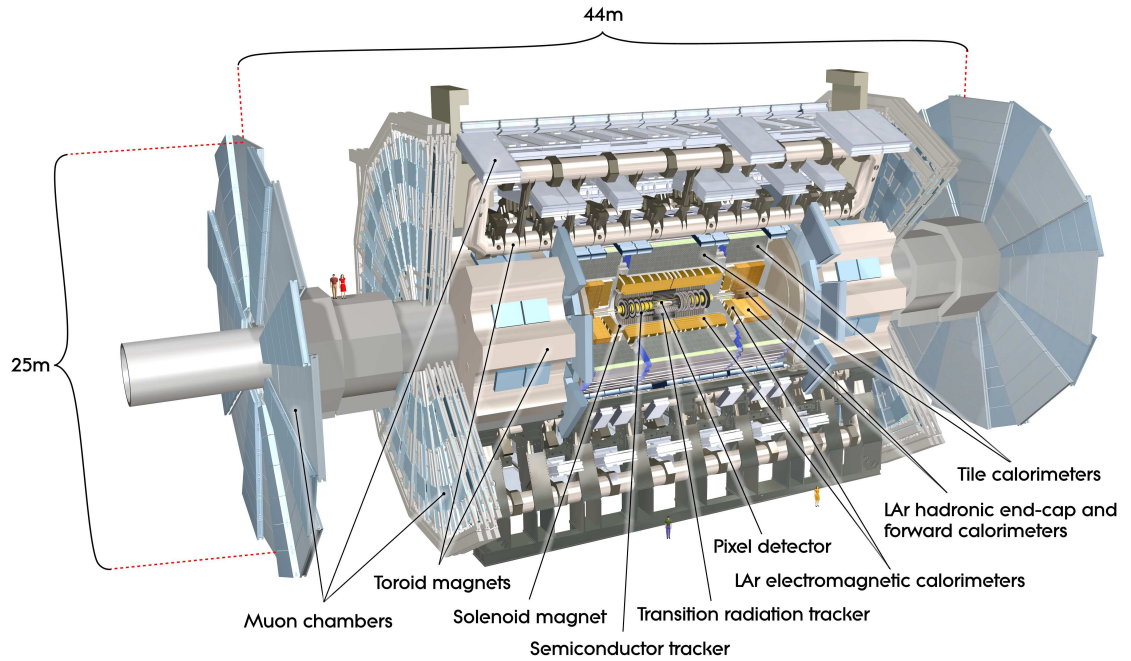


Figure 2.3: Cut-away view of the ATLAS detector. (The dimensions of the detector are 25 m in height and 44 m in length.) The overall weight of the detector is approximately 7000 tonnes [54].

The ATLAS detector [54], seen in figure 2.3, sits 100 m underground just over the road from the main CERN site and at 45 m long, 25 m in diameter and weighing over 7,000 tons

is one of largest and most complex particle physics experiments in the world. The detector itself can be divided in to four main subsystems and from the interaction point out they are; the inner detector (ID) or tracking detector, the calorimeters both electro-magnetic (EM) and hadronic (HCAL), the magnet system and the muon spectrometer (MS). There is also a small set of forward detectors, not detailed here, for accurate measurement of the integrated luminosity provided to ATLAS by the LHC named ALFA, LUCID and ZDC [54].

As a whole the detector has several different sets of coordinate systems some of which are used in analysis and some used primarily in detector design and placement. The first is  $z$  or the  $z$ -axis. This runs along the beam line through the centre of the detector with 0 existing at the very centre of the detector.  $x$  and  $y$ -axes do exist but are rarely needed as radial coordinates serve the purpose better. Here  $R$  is then the radial distance out from the beam line and  $\phi$  is the angle perpendicular to  $R$  and  $z$  measuring the angle around the barrel of the detector. The last coordinate is  $\theta$  measuring the angle off of the  $z$ -axis. This angle however is not often used and instead the angle  $\eta$  or pseudorapidity is used. Defined in equation 2.1 this quantity has the benefit of being invariant under transformation.

$$\eta = -\ln\left[\tan\left(\frac{\theta}{2}\right)\right] \quad (2.1)$$

Broadly the detector is also divided in to the barrel region (cylinder surrounding the interaction point) and endcap regions (circles covering the ends of the barrel region) which use slightly different configurations and technology in order to cover a full range in  $\eta$ . The barrel is found below an  $\eta$  of 1.37 and the endcaps above 1.52 and below 2.47. Following is a description of each main subsystem while focusing particularly on both the Inner Detector and EM calorimeter as these are the important systems in identification of electrons used for this analysis [54].

### 2.2.1 Inner Detector

The Inner Detector is ATLAS's main tracking detector which is fitted closest to the interaction point. A tracking detector is needed to trace charged particles from the interaction point out to the calorimetry system and give two bits of information; a charged particle's position to match with the calorimeters (or Muon Spectrometer in the case of muons) and

Detector component	Required resolution	$\eta$ coverage	
		Measurement	Trigger
Inner Detector	$\sigma_{p_T}/p_T = 0.05\% p_T \oplus 1\%$	$ \eta  < 2.5$	N.A
EM calorimetry	$\sigma_E/E = 10\%/\sqrt{E} \oplus 0.7\%$	$ \eta  < 3.2$	$ \eta  < 2.5$
Hadronic calorimetry barrel and end-cap forward	$\sigma_E/E = 50\%/\sqrt{E} \oplus 3\%$	$ \eta  < 3.2$	$ \eta  < 3.2$
	$\sigma_E/E = 100\%/\sqrt{E} \oplus 10\%$	$3.1 <  \eta  < 4.9$	$3.1 <  \eta  < 4.9$
Muon spectrometer	$\sigma_{p_T}/p_T = 10\%$ at $p_T = 1$ TeV	$ \eta  < 2.7$	$ \eta  < 2.4$

Table 2.1: Detector components design resolution requirements and  $\eta$  ranges for triggering and readout [54].

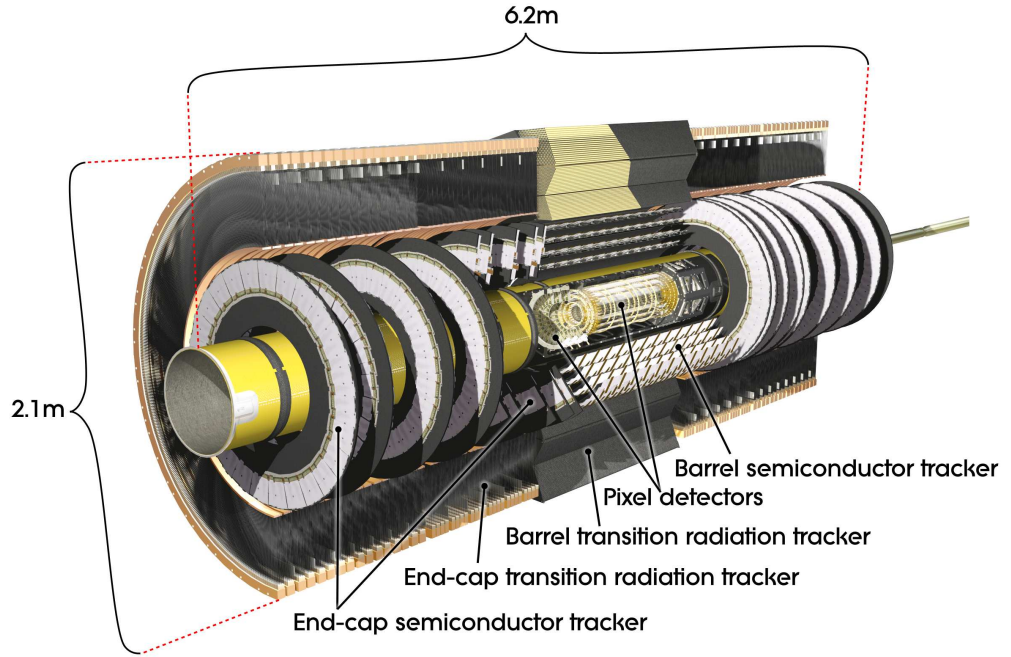


Figure 2.4: Cut-away view of the ATLAS inner detector [54].

when a magnetic field is present an estimate of a particle's momentum to compare with the calorimeter obtained from the radius of its curve. The ATLAS tracking system is composed of three different tracking technologies in order going out from the collision point; the Pixel Detector (PD), the Semiconductor Tracker (SCT) and the Transition Radiation Tracker (TRT). The Inner Detector was designed to precisely measure charged tracks in the energy range 0.5 GeV - 150 GeV while complimenting the energy measurements of the calorimetry system. Covering a range of  $|\eta| < 2.5$  and full range in  $\phi$  the Inner Detector with the help of the 2 T magnetic field imposed by the solenoid magnet (discussed



below) has a design momentum resolution of  $\sigma_{p_T}/p_T = 0.05\% p_T \oplus 1\%$  for charged tracks. In its design it was also important for the Inner Detector to be able to distinguish between multiple primary vertices at the collision point, referred to as pile-up, as well as secondary vertices from sources such as the hadronisation of b quarks. A schematic of the inner detector with all its subsystems can be seen in figure 2.5.

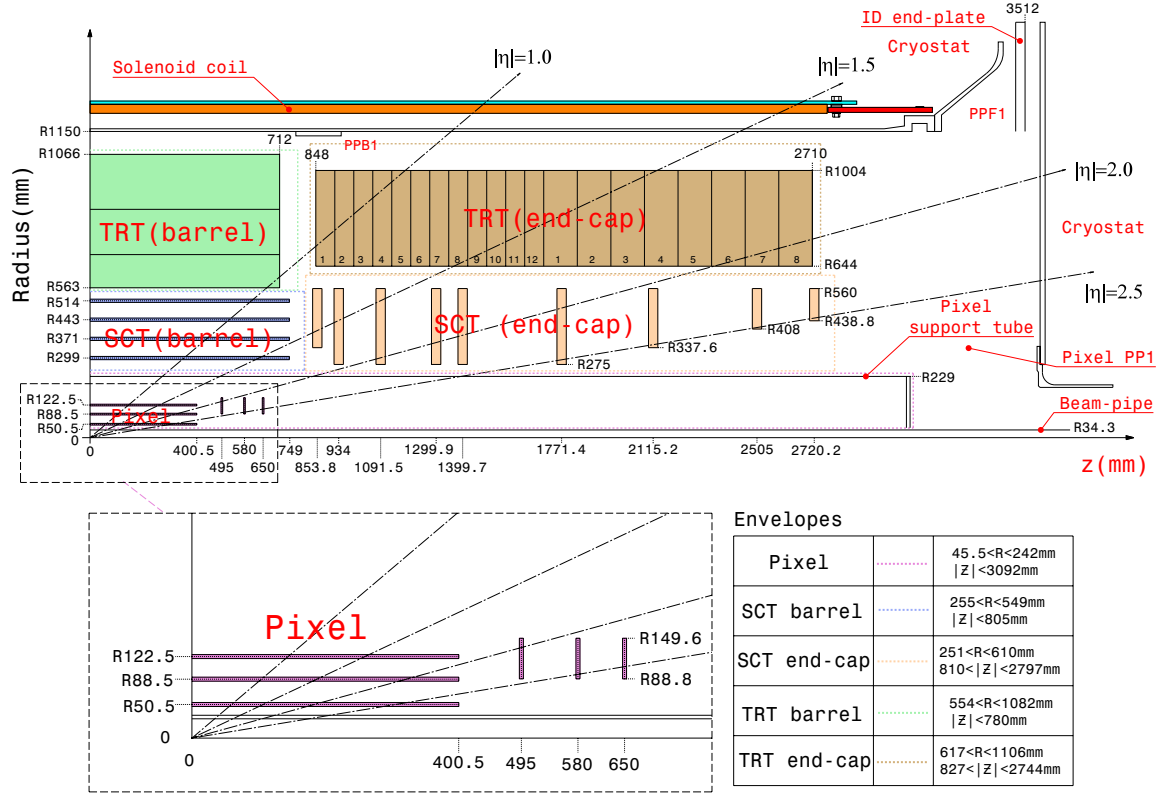


Figure 2.5: Plan view of a quarter-section of the ATLAS inner detector showing each of the major detector elements with its active dimensions and position in  $z$  and  $R$  detector coordinates [54].

### Pixel Detector

The Pixel Detector is the first layer and closest to the beam line consisting of three layers of silicon pixels. Because of its proximity to the beam line the pixel detector is designed to be heavily radiation hard and understood to the degree that its performance can be predicted over an extended period of radiation exposure. The Pixel Detector is made of a barrel and two endcaps composed of 1744 modules all together.



### **Semiconductor Tracker**

The SCT consists of the same technology as the PD but is organised in to 4 layers in the barrel region and 9 layers in each endcap. Due to the packed nature of these electronics cooling is important in this layer and so the sensors in each module are glued to each side of a thermally conductive spine that gives the SCT both structure and allows transport of heat out via the mounting point of each module keeping them at their operating temperature of  $-7^{\circ}\text{C}$ .

### **Transition Radiation Tracker**

The TRT uses a completely different tracking technology to the rest of Inner Detector using straw detectors composed of 4 mm diameter polyimide tubes each with a  $31\text{ }\mu\text{m}$  diameter gold plated Tungsten-Rhenium wire. Due to the small diameter of the straws the TRT can obtain the high read-out rate needed for experiments at the LHC. The barrel region consists of 50,000 of these straws with a readout at each end providing 100,000 readout channels. The endcaps contain another 320,000 straws only read out a one end giving the TRT a total of 420,000 channels. Each channel measures drift time giving a design resolution of  $170\text{ }\mu\text{m}$  in each straw. The straws are filled with a high Xenon concentration ( $\text{Xe}(70\%)\text{CO}_2(27\%)\text{O}_2(3\%)$ ) of gas in order to detect electrons via radiated photons as they traverse the material between straws. This is achieved by giving each straw two timing thresholds, the lower to discriminate tracking hits (direct hits) while the higher threshold discriminates transition radiation hits.

### **2.2.2 Calorimeters**

While the Inner Detector only measures charged particles, the calorimeters (seen in figure 2.6) measure both neutral and charged particles and are split in to two sections for particles with differing properties. The inner Electromagnetic Calorimeter is designed primarily to measure electrons and photons as well as pions while the outer Hadronic Calorimeter looks for hadrons such as neutrons and protons. In analyses the Hadronic Calorimeter is primarily used to look for jet objects (a collection of particles issuing from the decay of one mother particle). The primary method of identifying charged particles is to look for an associated

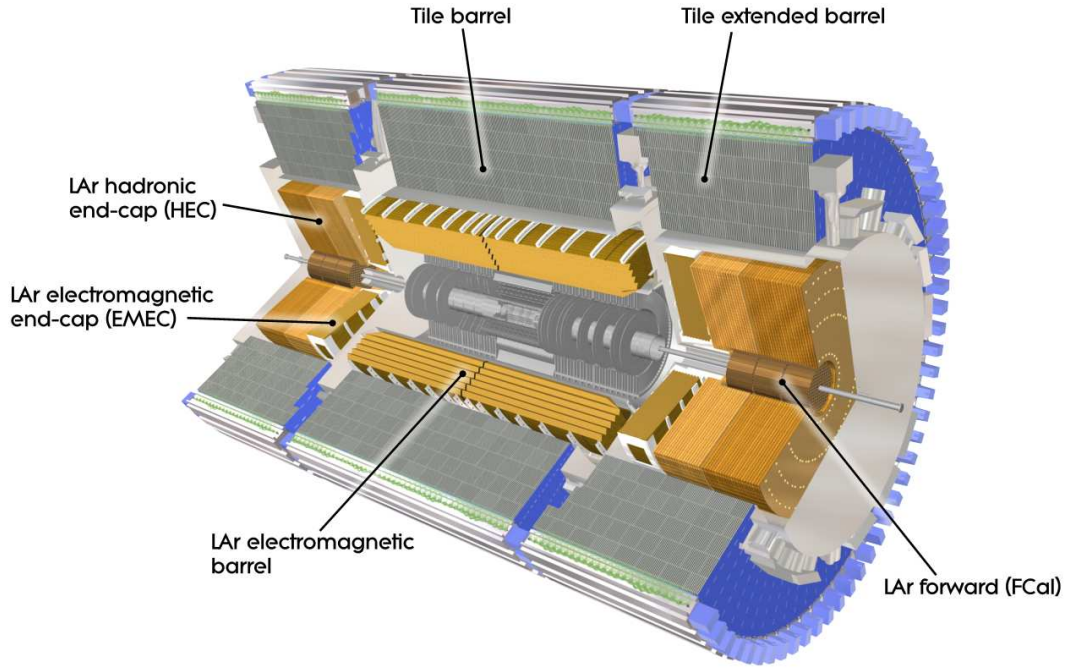


Figure 2.6: Cut-away view of the ATLAS calorimeter system [54].

track within the Inner Detector although the shape of the energy deposit in the calorimeters also helps with identification. Figure 2.8 shows a cross section view of the calorimeter layout where the crack region between the barrel and endcap regions can be seen.

### Electromagnetic Calorimeter

The Electromagnetic Calorimeter (ECAL) is designed to fully stop all electromagnetic showers within its volume. Split in to a barrel section and two endcaps the ECAL uses Liquid Argon (LAr) as a detecting medium with lead as the absorber. The lead is arranged in an accordion fashion (seen in figure 2.8) to ensure consistent performance throughout  $\phi$ . In the barrel section a presampler of LAr type is found before the main calorimeter to correct for dead material. The barrel contains three layers of LAr modules of decreasing size in towards the collision point in order to keep good position resolution. The endcap only contains two layers of modules with the the inner layer containing smaller modules for the same reason as the barrel region.

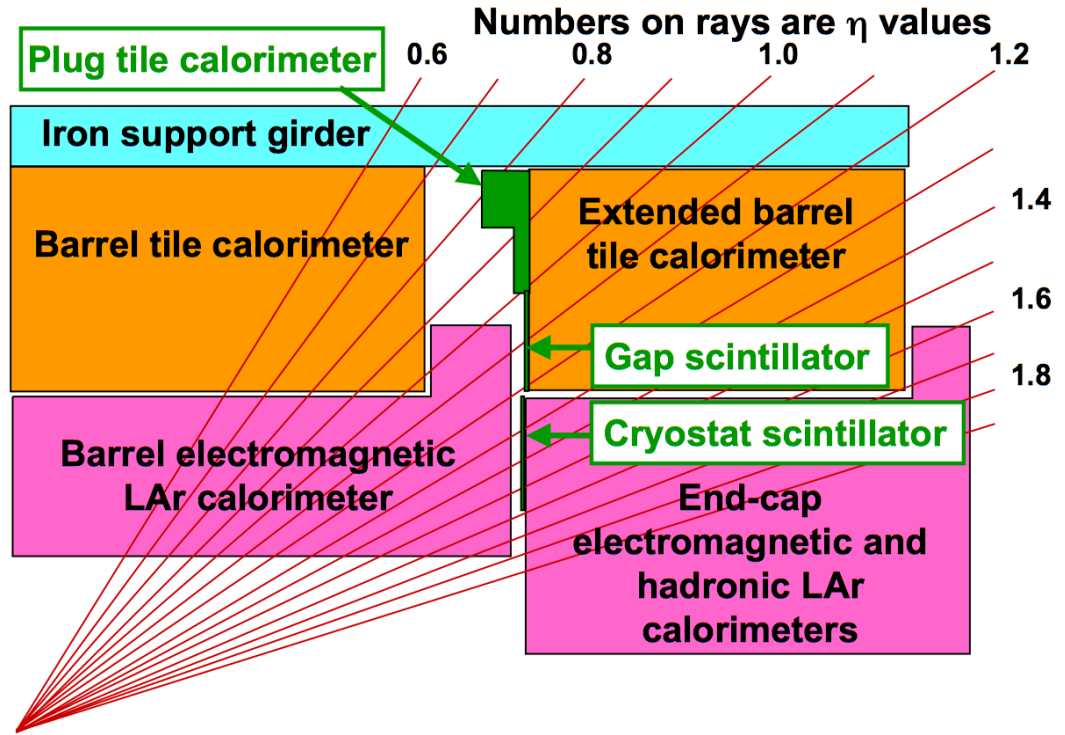


Figure 2.7: Schematic of the transition region between the barrel and endcap cryostats [54].

### Hadronic Calorimeter

The Hadronic Calorimeter is designed to stop all hadronic showers within its volume and consists of two parts, the Tile Calorimeter (HCAL) in the barrel and the LAr Hadronic Endcap (HEC). The HCAL is a tile calorimeter consisting of alternating layers of scintillator and steel as the active medium and absorber respectively. The HEC on the other hand uses the same technology as the ECAL with copper plates filled with LAr as the detecting medium. As the Hadronic Calorimeter sits directly behind the ECAL it is used to select good electron candidates using hadronic isolation or the amount of leakage in to the HCAL from a electron shower in the ECAL.

### 2.2.3 Magnet System

The ATLAS detector has two main magnet systems, seen in figure 2.9, the inner solenoid magnet found between the TRT and the ECAL and the outer toroid magnets found interleaved with the Muon Spectrometer.

The solenoid system is a superconducting magnet which is kept at 4.6 K to provide the

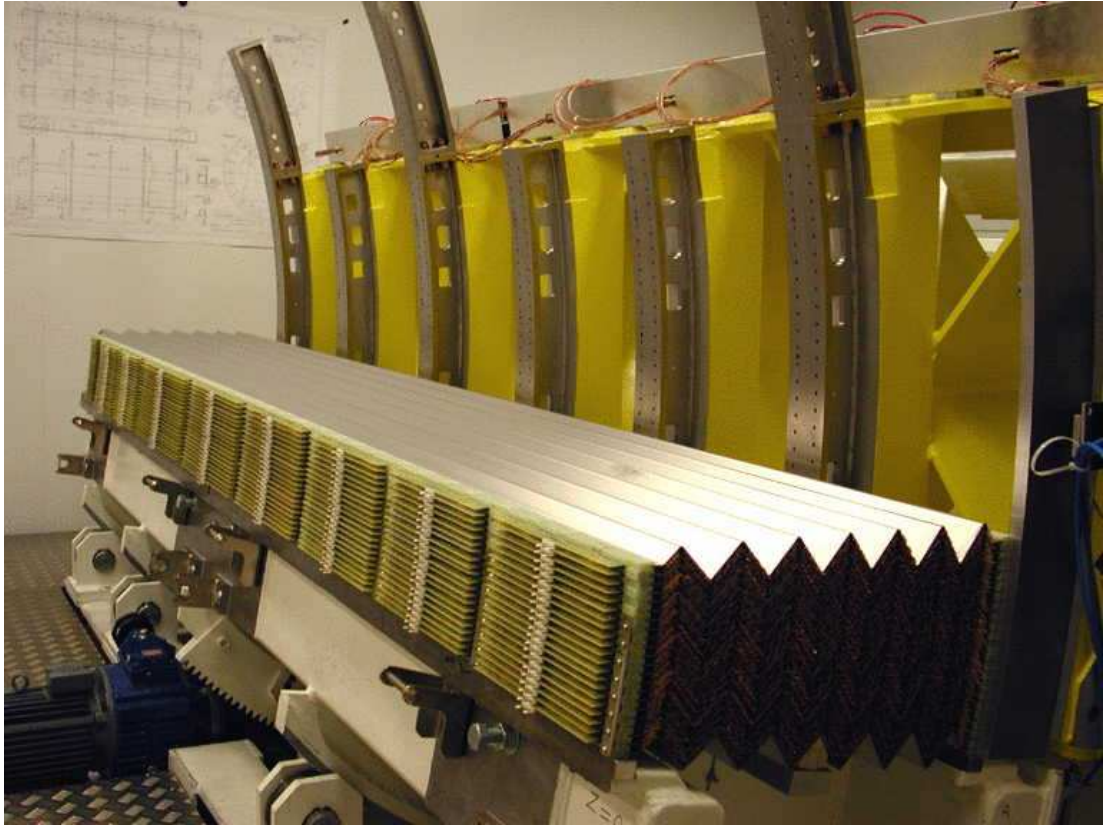


Figure 2.8: Photograph of the stacked electromagnetic LAr modules [54].

2 T magnetic field required by the inner detector to curve high energy particles found at the LHC. As the solenoid is found inside the calorimetry system it is important radiative thickness is minimised to reduce efficiency losses in energy measurements. In order to achieve this it was designed to minimise dead material and shares its cryostat vessel with the ECAL reducing the need for two and therefore contributing only 0.63 radiation lengths.

The outer toroid system provides a magnetic field for the muon spectrometer and consists of a barrel and two endcap systems each with eight coils assembled radially around the beam axis. The coils are all aluminium stabilised Niobium-Titanium (NbTi) superconductors with each coil in the barrel contained in its own cryostat while each of the coils in the endcap systems are contained in one single cryostat. The peak field provided by these toroids are 3.9 T and 4.1 T in the barrel and endcaps respectively.



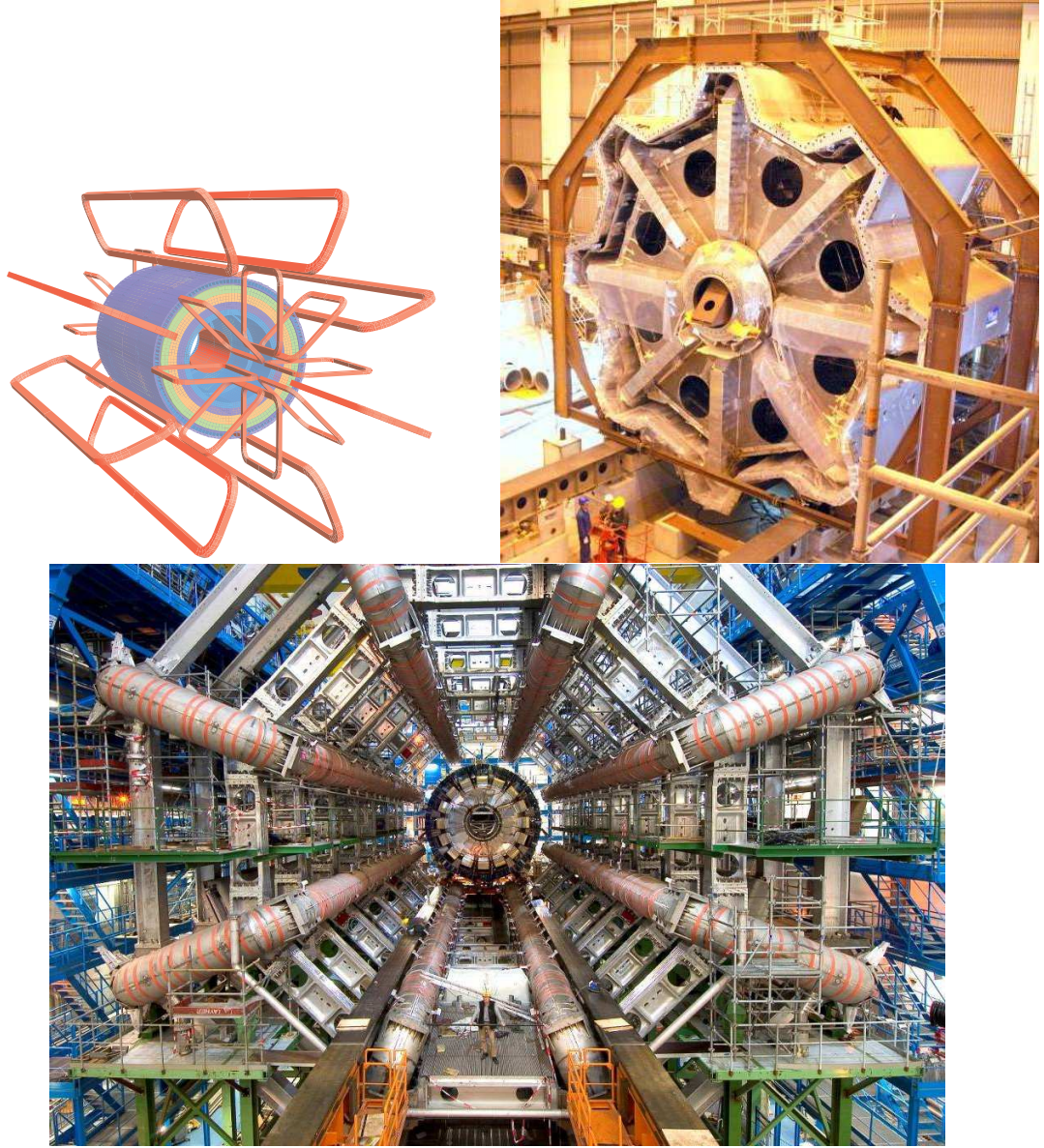


Figure 2.9: Geometry of magnet windings and tile calorimeter steel (upper left), end-cap toroid cold mass inserted into the cryostat (upper right) and barrel toroid as installed in the underground cavern (bottom) [54].

#### 2.2.4 Muon Spectrometer

Due to the penetrative nature of muons, all the layers of detector discussed above do not induce the showering of high energy muons. Therefore the outermost detector is another tracking detector specifically for muons. It uses the outer toroid magnet system to bend muon paths and measure muon momentum. The Muon Spectrometer is composed of 4 different technologies; Monitor Drift Tubes (MDT), Cathode Strip Chambers (CSC), Re-

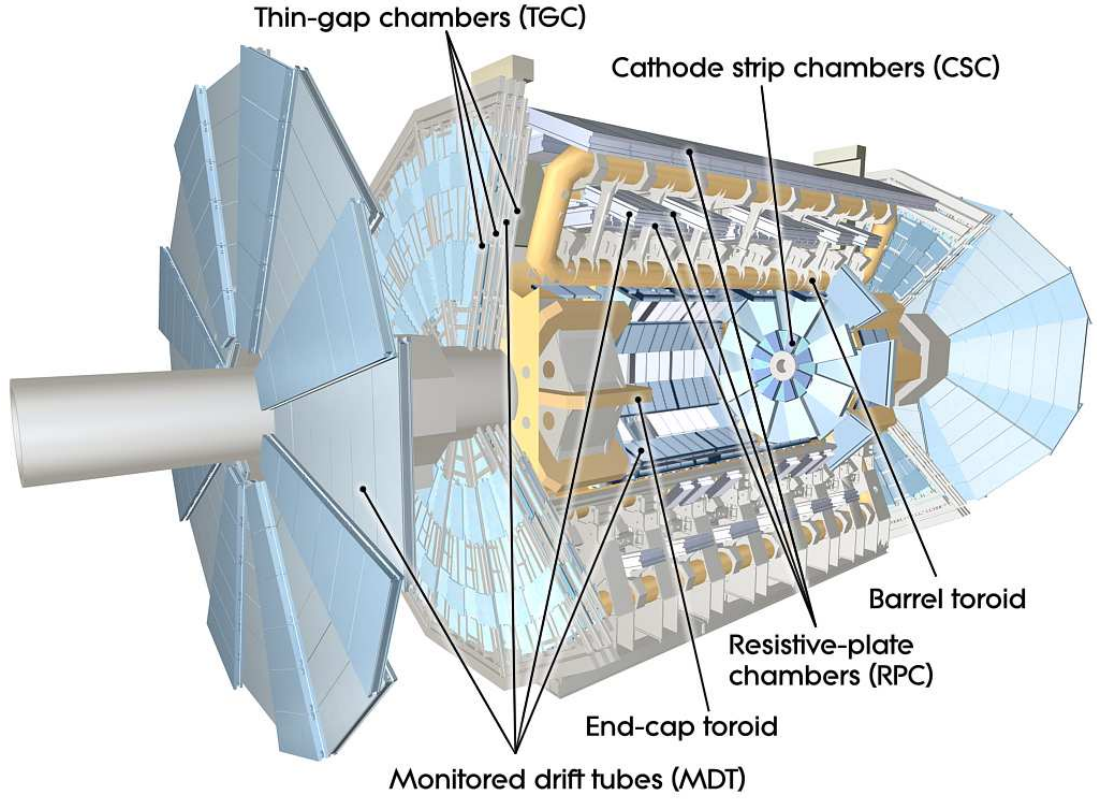


Figure 2.10: Cut-away view of the ATLAS muon system [54].

sistive Plate Chambers (RPC) and Thin Gap Chambers (TGC) all seen in figure 2.10. Both the MDT and the CSC boast precision tracking but both have slow readout times. The RPCs and TGCs have the job of triggering muons and providing additional track measurements. The RPCs are found in the barrel region ( $|\eta| < 1.05$ ) while the TGC trigger in the endcap region ( $1.05 < |\eta| < 2.4$ ). The MDT covers a full range in  $\eta$  ( $|\eta| < 2.7$ ) with complementary measurements from the CSC at  $2.0 < |\eta| < 2.7$ .

---

## Chapter 3

# The Trigger & Data Acquisition

The trigger system within ATLAS [54] is designed to manage the high rate of events produced by the LHC and bring them down to a total rate that can be written to permanent storage by selecting “interesting” events. The related Data Acquisition (DAQ) system controls the flow of data from detector hardware through the trigger system to permanent storage at CERN and the worldwide tier 1 grid sites.

The trigger system is made up of three main decision levels; Level 1, Level 2 and Event Filter. Level 1 (L1) is mainly hardware based using limited detector information to locate regions of interest (RoIs) and pass them the Level 2. The Level 2 (L2) system checks the RoIs with full detector granularity and precision and the last stage the Event Filter (EF) uses analysis reconstruction techniques to further select “interesting” events down to the level of 400-500 Hz. Both the L2 and EF triggers compose what is called the High-Level-Trigger (HLT) together with the event building software needed by the EF. Figure 3.1 shows the over all trigger system and how data flows through it.

Following is a description of each of the sections of the trigger while focusing on the selection of electron objects that are relevant for this analysis. Following this is a discussion of how the trigger menu is formed so bandwidth can be shared between the differing physics goals as well as how ATLAS handles the continued high luminosity push of the LHC.

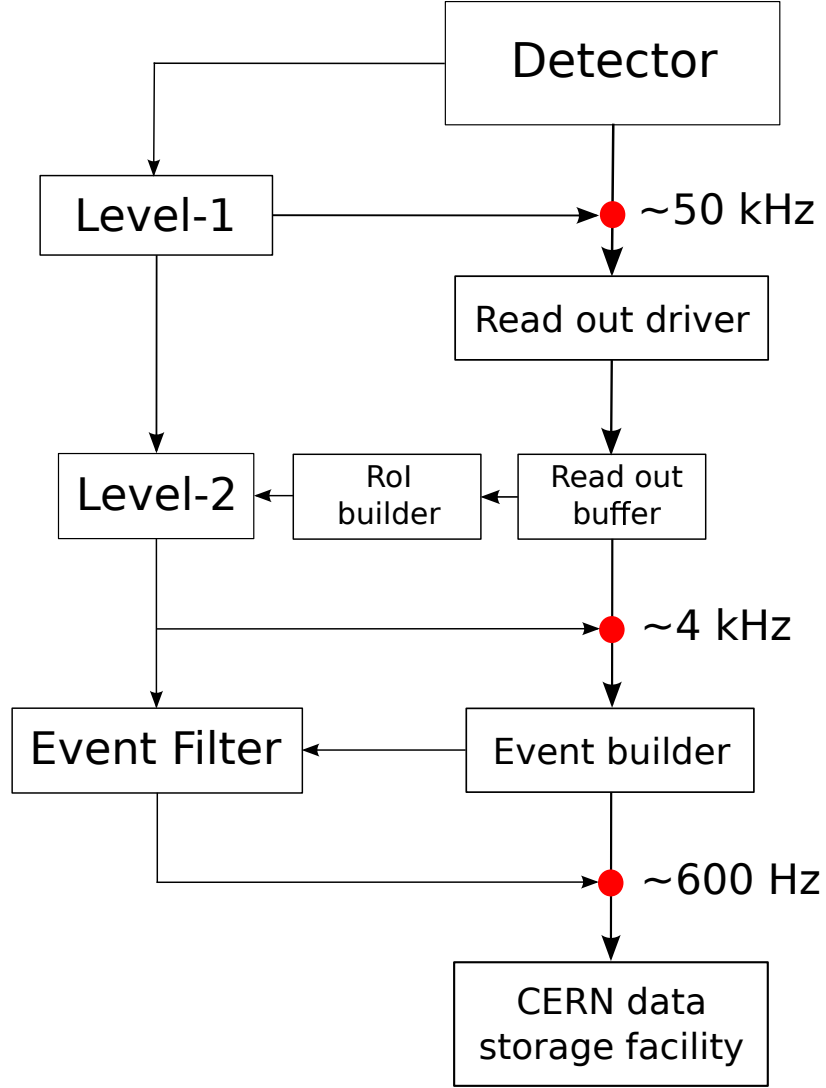


Figure 3.1: Diagram showing the different stages of the trigger and how they interact. Red points indicate point of acceptance for each trigger and numbers show the approximate number of events accepted per second at the end of the 8 TeV run in 2012.

### 3.1 Level-1 Trigger

The Level 1 (L1) trigger searches for RoI's consisting of strong signatures, i.e. high energy, muons, electron/photons or jets. The L1 trigger also searches for events with a large missing transverse energy ( $E_T^{miss}$ ) or large total transverse energy ( $\Sigma E_T$ ). Due to the decision speed required only some parts of the detector can be used at L1 (and at a much coarser granularity than is possible). For muon acceptance only the RPC's and TGC's can be used while for electromagnetic clusters and jets as well as large  $E_T^{miss}$  and  $\Sigma E_T$  the full calorimetry system can be used. The Inner Detector can not be used in L1 decisions due to the time constraint.



With a beam crossing interval of 50 ns latency is required to be less than  $2.5\ \mu\text{s}$  with a target of  $2.0\ \mu\text{s}$ . However half of this quota, about  $1.0\ \mu\text{s}$ , is accounted for by the cable propagation of signals.

The L1Calo system uses trigger towers with a granularity reduced to roughly  $0.1 \times 0.1$  in  $\Delta\eta \times \Delta\phi$  in most of the detector range from both the electromagnetic and hadronic calorimeters. The ECAL produces almost 3500 of these trigger towers via summation of the analogue signals from a range of trigger cells. This trigger tower data is then sent to the Cluster Processor (CP) to identify electron/photon and tau candidates with  $E_T$  above a required threshold and passing isolation requirements, which are labelled as RoI's.

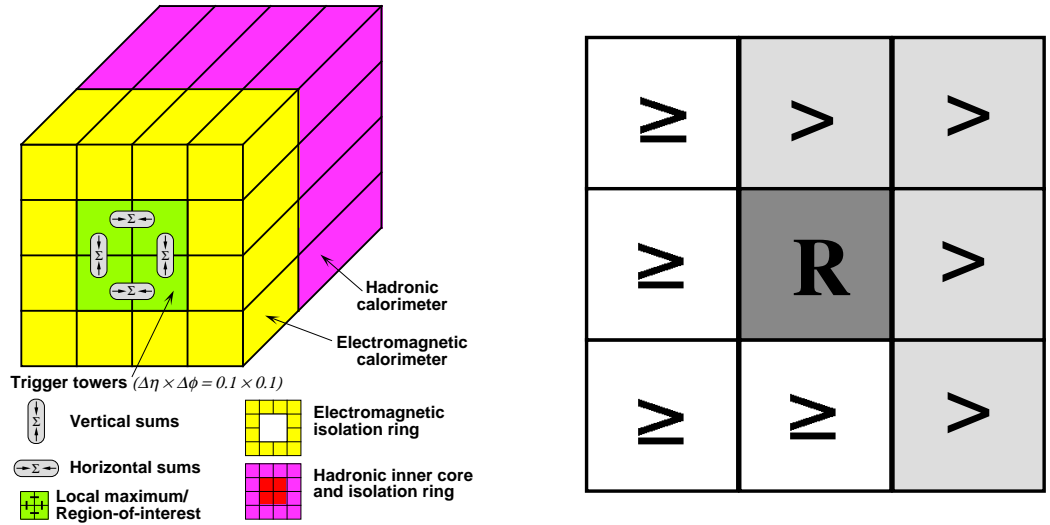


Figure 3.2: Electron/photon and tau trigger algorithms (left) and  $E_T$  local-maximum test for a cluster/RoI candidate (right). (The eta-axis runs from left to right, and the phi-axis from bottom to top. The symbol R refers to the candidate  $2 \times 2$  region being tested.)

Figure 3.2 shows how the electron/photon trigger clustering algorithm works by identifying  $2 \times 2$  clusters of trigger towers within which two adjacent towers sum to greater than the triggering threshold defined in the trigger menu (seen in section 3.4). Also shown is how three forms of isolation can be applied at this stage: the 12-tower surrounding ring, the  $2 \times 2$  hadronic core behind the RoI and the 12-tower surrounding ring in the hadronic calorimeter. Only the hadronic core isolation has so far been used in electron/photon triggers within ATLAS. As all possible  $2 \times 2$  clusters are observed in this way it is possible to have double counting of RoIs and so the sum of each  $2 \times 2$  RoI must be greater than each of its eight nearest overlapping neighbours. Figure 3.2 also shows how this local-maxima

is tested to avoiding identical sums through use of ‘greater than’ and ‘greater than or equal to’ in differing  $\eta$  and  $\phi$  directions. So if two adjacent  $2 \times 2$  clusters have the same combined energy sum the one to the top or right is chosen so as not to delay the trigger process. The final L1 trigger decision is made by the Central Trigger Processor (CTP) which takes information from both the CP and jet algorithm as well as the L1 muon trigger. If an accept decision is made then RoI’s are sent to the RoI builder which seeds the L2 trigger system and all L1 sub-systems are read out via Readout Drives (ROD’s)(discussed in section 3.3) to the DAQ system for monitoring of the L1 trigger system.

## 3.2 Higher Level Trigger

### Level-2 Trigger

The Level-2 (L2) trigger is seeded by and only makes decisions based on the RoI’s supplied by the L1 trigger. However it does this with full detector information and so the first stage of this trigger is a RoI builder. The RoI builder requests detector information for all relevant detectors for the observed RoI, including at this level the Inner Detector. In the case of electrons this includes the inner tracking detector, the electromagnetic calorimeter and the hadronic calorimeter. It is at L2 that a distinction between electrons and photons can be made due to existence of an associated track in the ID to the RoI in the ECAL. The RoI builder identifies calorimeter clusters and nearby tracks in order for the L2 trigger to make its decision based on algorithms reconstructing shower shapes, track-cluster matching and  $E_T$  thresholds with isolation. The list of these requirements are held within trigger chains each designed to accept specific physics signatures (see section 3.4.1). The general idea is simply to check if RoI’s still exist under closer inspection in order to reduce the rate of events before full event building takes place in the Event Filter.

### Event Filter

The Event Filter (EF) does not differ to the L2 trigger it is purely a further test of the signals handed over from L2. At this level a full reconstruction of the event takes place and EF trigger requirements with slightly more stringent thresholds are applied to the event. This

is the final decision for whether the event is going to be copied to permanent storage and so the EF reduces the final acceptance rate down to the 400 - 600 Hz required by CERN's computing systems. The requirements at the EF level are also those used in ATLAS analysis so as to treat MC and data samples the same. These requirements are discussed in section 3.4.1.

### 3.3 Data Acquisition

The Data Acquisition (DAQ) system is the set of systems that control the flow of data from detectors, through the trigger and in to permanent storage. The first stage of this process is the Readout System (ROS) a set of 145 PC's or nodes which manages the collection of all detector sub-system data and L1 trigger output from ATLAS. This system is helped by Readout Drivers (ROD's) which interface directly with detector components and Readout Links (ROL's), direct point-to-point readout connecting the ROD's with the ROS's. Table 3.1 shows the number of readouts for each component of the detector and L1 system.

Each ROS PC contains Readout Buffer Module's (ROBIN's), custom PCI-X cards, each containing three Readout Buffers (ROB's), at the end of each ROL. The ROB's is where event data is stored while the L2 trigger makes its decision which comes from the set of 10 L2 Supervisor (L2SV) nodes. This decision is then made by the DataFlow Manager (DFM) on input from all the L2SV nodes and sends a command to the ROS's to either expunge data or forward it on to the event building nodes (or Sub farm Input, SFI). Once a event fully built it is sent forward to the HLT farm which makes the EF decision, then and only then is a message sent back down via the DFM for the ROS's to fully delete all data from the event. The HLT farm is the largest computing resource in the DAQ system with 1116 nodes each containing 8 CPU's. These nodes can either be configured to run as the EF or L2 Processing Units (L2PU's) for the L2SV and are reconfigured as need dictates. As the final step if an event is accepted by the EF all data is passed to the Sub Farm Output (SFO) where it is stored before transfer to CERN's central data-recording facility. In the case that this connection to CERN is offline for some reason ATLAS is able to store about 24 hours worth of data in the SFO's so no data is lost. Table 3.2 shows the number of each DAQ component used within ATLAS all of which are found in the USA15 service cavern next to

Detector Partition			Number of RODs	Number of ROLs	Number of ROSs
Inner detector	Pixel	Layer 0	44	44	4
		Disks	24	24	2
		Layers 12	64	64	6
	SCT	End-cap A	24	24	2
		End-cap C	24	24	2
		Barrel A	22	22	2
		Barrel C	22	22	2
	TRT	End-cap A	64	64	6
		End-cap C	64	64	6
		Barrel A	32	32	3
		Barrel C	32	32	3
	Calorimetry	Tile	Barrel A	8	16
Barrel C			8	16	2
Extended barrel A			8	16	2
Extended barrel C			8	16	2
LAr		EM barrel A	56	224	20
		EM barrel C	56	224	20
		EM end-cap A	35	138	12
		EM end-cap C	35	138	12
		HEC	6	24	2
		FCal	4	14	2
Muon spectrometer	MDT	Barrel A	50	50	4
		Barrel C	50	50	4
		End-cap A	52	52	4
		End-cap C	52	52	4
	CSC	End-cap A	8	8	1
End-cap C		8	8	1	
L1	Calorimeter	CP	4	8	1
		JEP	2	8	1
		PP	8	32	3
	Muon RPC	Barrel A	16	16	2
		Barrel C	16	16	2
	Muon TGC	End-cap A	12	12	1
		End-cap C	12	12	1
	MUCTPI		1	1	1
CTP		1	1	1	
Total			932	1574	145

Table 3.1: Numbers of readout drivers (RODs), readout links (ROLs) and readout systems (ROSs) per detector partition at design [54].

the ATLAS cavern.

Component	Number of nodes	Number of racks	Number of CPUs/node
ROS	145	16	1
DFM	12	1	2
L2SV	10	1	2
SFI	48	3	2
HLT	1116	36	8
SFO	6	2	2
Monitoring	32	4	4
Operations	20	4	2

Table 3.2: The main data-acquisition system components deployed for initial operation: the readout system (ROS), the event-building node (SFI), the data flow manager (DFM), the L2 supervisor (L2SV), the high-level trigger (HLT) and the event filter output nodes (SFO) [54].

### 3.4 Trigger Menu and Rates

In its simplest form a single trigger is an energy threshold designed to select a high percentage of particles of a selected type. ATLAS contains many of these thresholds to select many interesting physics objects which are roughly grouped in to similar signatures called streams. The trigger streams are egamma ( $e/\gamma$ ) triggers to select electrons and photons, JetTauEtMiss triggers to select hadronic decays, tau decays and large missing transverse energy, Muon triggers to select muons, MinBias trigger to check no bias's exist in other triggers and cosmics triggers to selected signals of cosmic radiation. Each stream has a given bandwidth allocated for readout from the trigger so all triggers need to be optimised so total acceptance rates are within requirements. Each trigger at the HLT level is designed to select a specific type of signal while those a L1 are more general and seed many HLT triggers. A full run through all three stages of the trigger is called a trigger chain. Each trigger in a trigger chain needs to not only be optimised to fulfil acceptance rate but also optimised for high acceptance efficiency in the valid region. In terms of energy threshold this means an increasing threshold through the trigger chain so that each level is selecting within the range close to 100% efficient from the previous requirement when taking in to account the different accuracy of energy measurement provided by each level. This section focuses on the egamma trigger stream as all objects in this analysis where selected using it.

### 3.4.1 The “ $e/\gamma$ ” Trigger Menu

The  $e/\gamma$  trigger menu that is used in this analysis refers to trigger chains designed to select electron and photon objects detailing requirements for all three stages of the trigger. ATLAS uses its own terminology to name these triggers with the name giving a description of the requirements used. At L1 electron and photon objects are selected with triggers bearing the name EMXY where; ‘EM’ refers to EM calorimeter, X is the value of the energy threshold required of RoIs in GeV and Y refers to any other specification. Other specifications can be ‘V’, a threshold varying in detector geometry ( $\eta$ ) around the given value to optimise selection, or ‘H’, indicating hadronic isolation applied behind the RoI, both of which are discussed in section 3.4.2. An example of a L1 trigger is then L1\_EM18VH which is a trigger with an energy threshold of 18 GeV which is varied slightly through the detector and has an hadronic isolation requirement. L2 and EF use the same terminology but are prepended with either L2 or EF. They take the form such as e22vh\_medium where ‘e’ represents an electron (g is used for photons), ‘vh’ represents the same as above and ‘medium’ refers to an associated set of shower shape and tracking requirements. As well as ‘medium’, ‘loose’ and ‘tight’ are also defined giving looser and tighter requirements respectively. These shower shape and tracking requirements are discussed in section 4.1. Section 3.4.2 discusses the development of the L1\_EM16VH trigger which feeds in to L2\_e20vh\_medium and then in to EF\_e22vh\_medium.

The 8 TeV analysis discussed in this thesis uses a photon trigger even though searching for electrons. This is because photon and electron triggers are identical save for tracking requirements for electrons and for the 2012 run the lowest energy triggers without hadronic isolation that were applicable for high energy dielectron decays was a diphoton trigger chain. It is important that the trigger used did not have hadronic isolation due to the very high energy nature of the electrons in this analysis which have a higher chance of leaking through in to the hadronic calorimeter. The trigger used for the 8 TeV analysis is EF\_g35\_loose\_g25\_loose which selects two photon objects with thresholds of 35 GeV and 25 GeV while both requiring ‘loose’ shower shape requirements. This trigger is seeded by L2\_g30\_loose\_g20\_loose which itself is seeded by L1\_2EM12\_EM16V. EF\_g35\_loose\_g25\_loose reaches close to 100% efficiency of selecting two electron just above an electron energy of 40 GeV and maintains this to very high energy. The 7 TeV

analysis used the trigger EF\_g20\_loose.

### 3.4.2 Trigger Rates in High Luminosity Regime

Due to the bandwidth limitations of the trigger each level is restricted to a certain output rate. During 2011 the L1 output rate was kept below 60 kHz, L2 below 5 kHz and the EF output rate at  $\sim 400$  Hz averaged over the LHC fills. The bandwidth allocated to the  $e/\gamma$  triggers was approximately 30% of the total EF output rate however throughout 2011 the luminosity continued to increase putting pressure on the trigger's ability to control the output rate. Several methods were employed to reduce the trigger rate and in the  $e/\gamma$  trigger a variable threshold and hadronic core isolation were investigated to reduce the rate of the Level-1 trigger. In order to keep within timing constraints only a low resolution of  $0.4 \eta$  is available at L1. Threshold requirements were therefore investigated varying every  $0.4 \eta$ . The effect of a hadronic core isolation was also investigated on the selection of electrons which defines a region in the hadronic calorimeter behind the  $e/\gamma$  candidate in which a minimum amount of energy is required to be deposited in order to distinguish between jets and  $e/\gamma$  objects.

A study in to introducing these new requirements [55] at L1 was carried out using data from the trigger stream with a “tag & probe” study to calculate the efficiency of an array of new L1 requirements. Objects selected with “tag & probe” were organised in to bins of  $0.4$  in  $\eta$  and threshold of 16, 17, 18 and 19 GeV were applied as a L1 trigger. Within each  $0.4 \eta$  bin acceptance efficiency verses reconstructed transverse energy was studied. The highest threshold for which close to 100% efficiency was reached by a transverse energy of 22 GeV (threshold at EF) was then selected as the threshold in that region. The results of this optimisation can be seen in table 3.3 where the threshold for each eta region is given.

$ \eta $ region	Level-1 threshold [GeV]
$< 0.8$	18
$0.8 - 1.2$	17
$1.2 - 1.6$	16
$1.6 - 2.0$	17
$2.0 - 2.4$	18
$> 2.4$	16

Table 3.3: Optimised L1 thresholds for the L1 EM16 trigger.

Hadronic core isolations was investigated for isolation less than 1, 2 and 3 GeV. A hadronic core isolation of less than 1 GeV was chosen as this was seen to have a less than 1% effect on acceptance. Both of these requirements then went in to the specification of the L1\_EM16VH trigger.

Figure 3.4 shows the performance of the trigger after these changes had been made. It can be seen that a minimal impact of these new requirements is felt in efficiency for both  $\eta$  and number of primary vertices. Most importantly the “turn on” curve for efficiency as a function of  $E_T$  shows the point at which 100% efficiency is reached is not that much higher than EM16. This then introduced the new lowest threshold electron trigger chain used in ATLAS. The effect of this introduction can be seen during the middle of the year in figure 3.3 where a significant decrease in the event filter acceptance rate is seen with the introduction of this and several other trigger strategies.

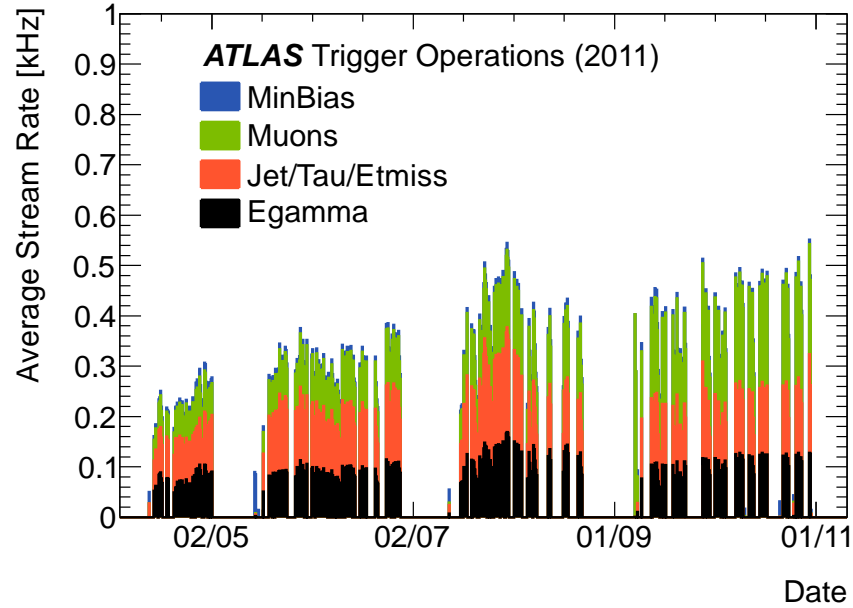


Figure 3.3: Event Filter stream recording rates from 2011. [56]

For the 2012 run this trigger went through a revision raising the thresholds of each trigger in the chain to accommodate higher luminosity at 8 TeV, this chain is discussed in section 3.4.1. This study was completed by the author as a part of the ATLAS service task and became part of a ATLAS conference note [55].



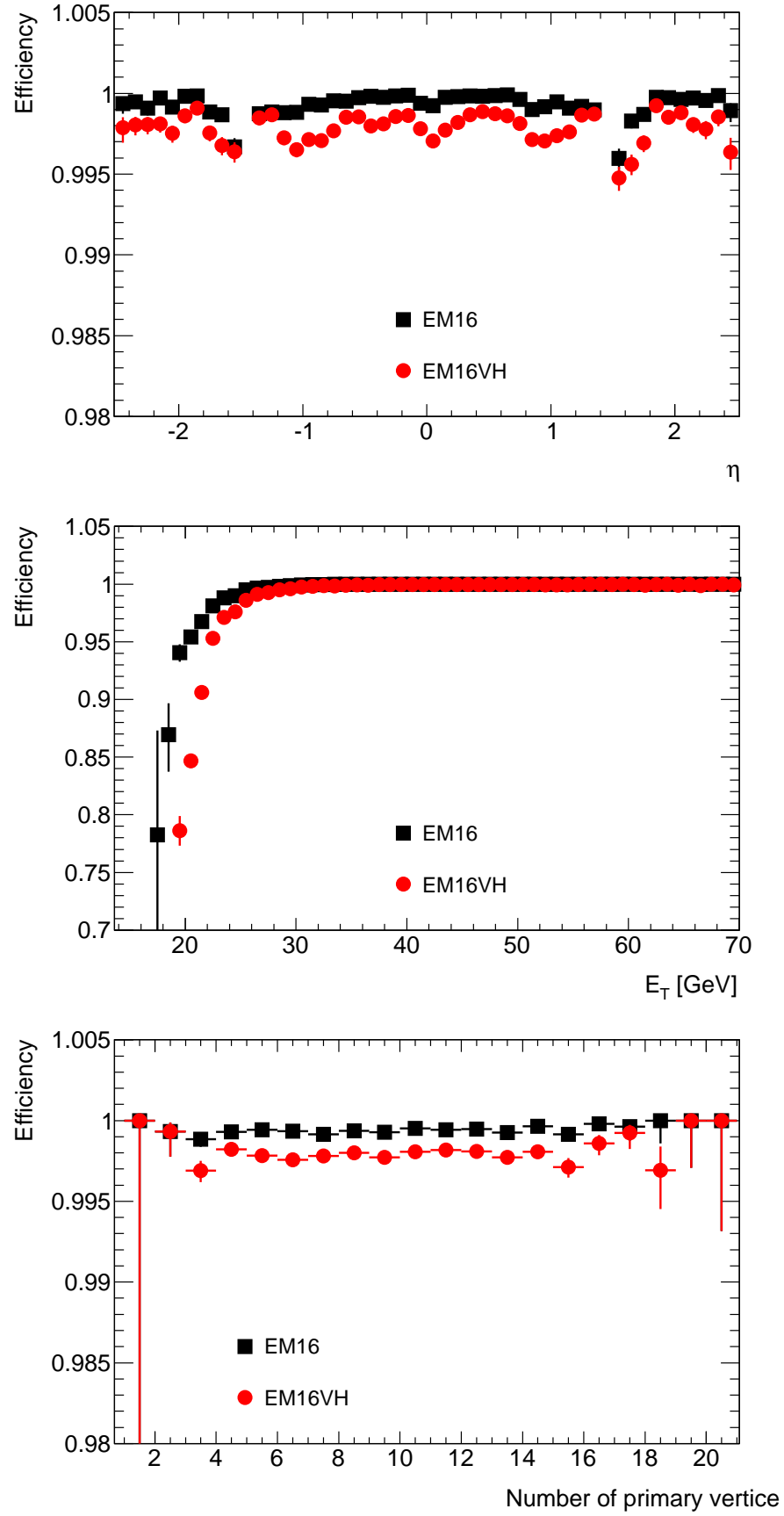


Figure 3.4: Performance of the first level of the ATLAS  $e/\gamma$  trigger before (EM16) and after (EM16VH) variable thresholds and hadronic core isolation are applied. Efficiency verse  $\eta$  (top),  $E_T$  (middle) and number of primary vertices (bottom).

---

## Chapter 4

# Event Reconstruction

Reconstruction is the process and algorithms that attempt to reform information about collision events and their decay products from detector signals. This process is done at several points in the ATLAS analysis procedure. First partial reconstruction of RoI's is done at the Level-2 trigger while a mostly full detector reconstruction is done at the EF. After the data has been permanently stored full reconstruction of all possible signatures in each event as well as whole event variables can be completed if it failed to finish live during the trigger decision.

The other main source of reconstruction is done in a process called reprocessing. After data has been stored updates to sub-detector calibrations and optimisations can take place and so reconstruction of entire data sets takes place to update variables to more accurate measurements.

The Data format used in this analysis is an internal ATLAS format called a D3PD. This format is a type of ROOT [57] ntuple, or sequence of ordered lists, which stores ATLAS event data. The data used has past through ATLAS software reconstruction while the Monte-Carlo (MC) background estimate samples have gone through a GEANT 4 [58] detector simulation as well as ATLAS reconstruction. This means analysis of these D3PD's with root requires only minor corrections.

Some of the many variables reconstructed are event specific and one of the more important of these is the number of interactions per bunch crossing. As more than one proton collision takes place with each bunch collision a lot of physics background can appear in an event. This makes the search harder and needs to be predicted properly by background

estimates. The problem is referred to as pile-up and corrections needed to accommodate it are discussed in section 6.1.1. Figure 4.1 shows the distribution of number of interactions per bunch crossing seen in the 7 TeV and 8 TeV ATLAS data sets.

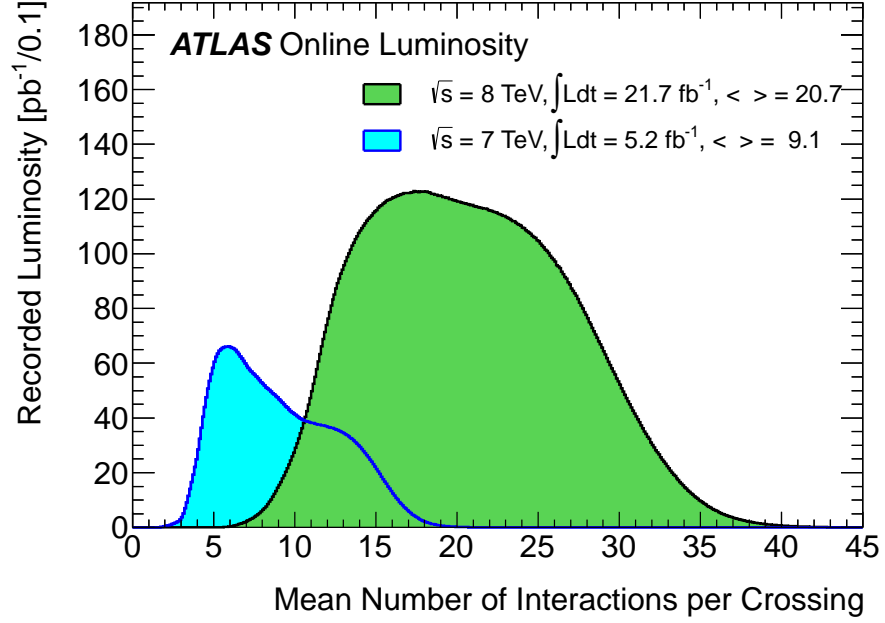


Figure 4.1: Luminosity-weighted distribution of the mean number of interactions per crossing for the 2011 and 2012 data. [59, 60]

Below will mainly be a discussion of the reconstruction of electron (and related photon) objects as these are the decay products searched for in this analysis.

## 4.1 Electron Reconstruction and Identification

During reconstruction each EM calorimeter energy signature with an associated track in the inner detector get listed as an electron object. These objects get selected via a clustering algorithm in the EM calorimeter which defines the energy and is then matched to a track. These objects then have a list of associated variables derived from detector readouts on which an analysis selection for ‘good’ electrons can be made. These variables range from simple values of position and energy to more complex derived values such as isolation. A few variables will be listed below relevant to this analysis and how they are derived.

- $\eta$  &  $\phi$ , a particle trajectory or position in detector. These are the main variables for measuring the direction the particle went in the detector and for electrons can be mea-

sured in two ways. Either via cluster location in the EM calorimeter or measurement in the inner detector.

- $p_T$  or transverse momentum.  $p_T$  is the main measure of energy used for particles where  $p_T = |p| \cosh \eta$ . Here  $\eta$  comes from either the inner detector or calorimeter cluster hit location and the choice is dependent on how many hits the track made travelling through the inner detector and therefore how accurate the measurement is.
- $E_{T\text{cone}20}$ . This is a cluster isolation variable measuring the sum of energy found around the region of interest minus the electron cluster for  $R < 0.20$  where  $R = \sqrt{\eta^2 + \phi^2}$ .  $E_{T\text{cone}20}$  is used to check cone isolation in order to eliminate jet like signatures from the analysis which often create large showers in the calorimeters.
- Electron Charge. By measuring the direction the electron curves in the inner detector the charge of an electron can be seen. However as discussed in chapter 5 this can be hard for very high energy electrons.
- loose, medium, tight. These are definitions given to a set of selections defining how certain it is the object is an electron. The selections and variables associated with this are discussed below.

Loose, medium and tight define an increasing series of selections for identifying good electron signatures in the detector. The selections vary between shower shape variables to track quality and track cluster matching. Some of the important associated variables are discussed in table 4.1 however the full selections are two dimensional arrays of threshold for most selections. Also to note there are two different definitions of medium referred to as medium and medium++. The latter is a re-optimisation of the selection and slightly stricter than the original medium. medium++ is used in the 8 TeV analysis and medium in the 7 TeV analysis.

<b>Loose selection</b>		
Type	Description	Name
Acceptance	$ \eta  < 2.47$	$\eta$
Hadronic leakage	Ratio of $E_T$ in the first layer of the hadronic calorimeter to $E_T$ of the EM cluster (used over the range $ \eta  < 0.8$ and $ \eta  > 1.37$ )	$R_{had1}$
	Ratio of $E_T$ in the hadronic calorimeter to $E_T$ of the EM cluster (used over the range $ \eta  < 0.8$ and $ \eta  > 1.37$ )	$R_{had}$
Middle layer of EM calorimeter	Ratio of the energy in $3 \times 7$ cells over the energy in $7 \times 7$ cells centred at the electron cluster position	$R_\eta$
	Lateral shower width, $\sqrt{(\sum E_i \eta_i^2)/(\sum E_i) - ((\sum E_i \eta_i)/(\sum E_i))^2}$ , where $E_i$ is the energy and $\eta_i$ is the pseudorapidity of cell $i$ and the sum is calculated within a window of $3 \times 5$ cells	$\omega_{\eta 2}$
<b>medium &amp; medium++ selection</b> (includes loose)		
Type	Description	Name
Strip layer of EM calorimeter	Shower width, $\sqrt{(\sum E_i (i - i_{max})^2)(\sum E_i)}$ , where $i$ runs over all strips in a window of $\Delta\eta \times \Delta\phi \approx 0.0625 \times 0.2$ , corresponding typically to 20 strips in $\eta$ , and $i_{max}$ is the index of the highest-energy strip	$\omega_{stot}$
	Ratio of the energy difference between the largest and second largest energy deposits in the cluster over the sum of these energies	$E_{ratio}$
Track quality	Number of hits in the pixel detector ( $\geq 1$ )	$n_{pixel}$
	Number of total hits in the pixel and SCT detectors ( $\geq 7$ )	$n_{Si}$
	Transverse impact parameter ( $ d_0  < 5$ mm)	$d_0$
Track-cluster matching	$\Delta\eta$ between the cluster position in the strip layer and the extrapolated track ( $ \Delta\eta  < 0.01$ )	$\Delta\eta$
<b>Tight selection</b> (includes medium)		
Type	Description	Name
Track-cluster matching	$\Delta\phi$ between the cluster position in the middle layer and the extrapolated track ( $ \Delta\phi  < 0.02$ )	$\Delta\phi$
	Ratio of the cluster energy to the track momentum	$E/p$
	Tighter $\Delta\eta$ requirement ( $ \Delta\eta  < 0.005$ )	$\Delta\eta$
Track quality TRT	Tighter transverse impact parameter requirement ( $ d_0  < 1$ mm)	$d_0$
	Total number of hits in the TRT	$n_{TRT}$
	Ratio of the number of high-threshold hits to the total number of hits in the TRT	$f_{HT}$
Conversions	Number of hits in the b-layer ( $\leq 1$ )	$n_{BL}$
	Veto electron candidates matched to reconstructed photon conversions	

Table 4.1: The variables associated with definitions of loose, medium and tight [61].

---

# Chapter 5

## Event Selection

The main event selection for this analysis is based on a standard cut-flow selection used within ATLAS to select high energy di-electron events. Following will be the basic outline of each requirement an event must satisfy followed by a discussion of optimisations done to some cuts for this analysis. Finally a discussion of corrections is included; spanning minor variable corrections to data obtained by performance groups after reconstruction and more substantial corrections to MC samples to correctly estimate run conditions. The following analysis selection is applied equally to the data and MC background samples unless where noted.

### 5.1 Analysis Selection

The following selection is made to all data and MC events for this analysis. Before selection several data flags are checked to insure full operation of the detector at time of data taking.

#### Event Selection

- Event is required have passed the chosen unscaled electron trigger (EF\_g35\_loose\_g25\_loose).
- Each event is required to contain at least one reconstructed primary vertex with at least 2 traceable charged tracks.

### Electron Selection

- Electron  $|\eta| < 2.47$  and not lie within the detector crack region  $1.37 \leq |\eta| \leq 1.52$  due to a decreased energy resolution.
- Each electron is required to have a transverse momentum ( $p_T$ ) greater than 30 GeV with the highest  $p_T$  electron lying above 40 GeV.
- Electrons are required to pass identification criteria on the transverse shower shape, the longitudinal leakage into the hadronic calorimeter, and the association to an inner detector track, defined together as a medium++ electron identification (see section 4.1).

### Dielectron Selection

- Selection of two highest  $p_T$  electrons left in event.
- Lead isolation (a cone around the candidate in the calorimeter is required to have  $< 0.007 \times E_T + 5.0 \text{ GeV}$  deposited in it) of the highest  $p_T$  electron in the event is used to suppress jet background.
- Sub-leading isolation (a cone around the candidate in the calorimeter is required to have  $< 0.0022 \times E_T + 6.0 \text{ GeV}$  deposited in it) of the second highest  $p_T$  electron in the event is used to suppress more jet background.
- Dielectron invariant mass ( $m_{ee}$ ) is required to be greater than or equal 80 GeV.
- Opposite sign requirement. Require both electrons to have opposite charge.

## 5.2 Isolation Requirement

When optimising for the 8 TeV analysis a re-investigation of the isolation requirement was needed, updating the selection from its previous iteration in the di-electron analysis on 7 TeV ATLAS data. The previous threshold was a flat, less than 7 GeV, cut on the calorimeter cluster isolation ( $E_{T\text{cone}20}$ ) of the highest  $E_T$  electron in the selected pair. The first investigation was to see how this cut performed in the selection of MC signal at 8 TeV

centre of mass energy. Due to the better statistics found in the  $DY \rightarrow ee$  MC sample and this being an irreducible background and therefore indistinguishable from the signal this was used in the following investigation.

This flat cut of 7 GeV causes an increasing efficiency loss at high energy and was deemed unsuitably high for this iteration of the analysis due to the higher reach in energy expected from the higher centre of mass collision energy. The introduction of an isolation requirement on the second highest electron was also proposed which did not exist in the 7 TeV analysis.

The possibility was an isolation requirement varying with energy. The main source of background the isolation cut is imposed to reduce is jets that fake an electron signal in the detector. Jet backgrounds are estimated via a reverse ID method on data seen in section 6.2 with low statistics at high energy. For this reason it is hard to optimise the isolation requirement against rejection of this background at high energy. Therefore it was chosen to optimise the new selection against the acceptance of signal. This study was undertaken by the author to optimise the isolation requirement.

Figure 5.1 shows the distribution of DY MC events in  $E_T$  and cluster isolation. It can be seen that electrons become less isolated under this definition of isolation as energy of the electron increases. This is to be expected as higher energy electrons produce larger showers and spread out over many EM calorimeter cells.

In order to define a requirement varying in  $E_T$ , the 99% acceptance point for each  $E_T$  column was calculated and a first order polynomial fit to these points was done by eye. The 99% acceptance points can be seen in figure 5.1 and this as well as the fit can be seen in figure 5.2. The same thing was calculated for the second highest  $E_T$  electron and can be seen in figure 5.3.

The two first order polynomials shown here correspond to isolation requirements of;

$$\begin{aligned} \text{Lead Isolation} &< 0.007 \times E_T + 5.0 \text{ GeV} \\ \text{Subleading Isolation} &< 0.022 \times E_T + 6.0 \text{ GeV} \end{aligned}$$

for the highest and second highest energy electrons respectively.

An analysis of the efficiency of these cuts on signal can be seen in figures 5.4 and 5.5 where it can be seen they maintain a flat behaviour as  $E_T$  increases.



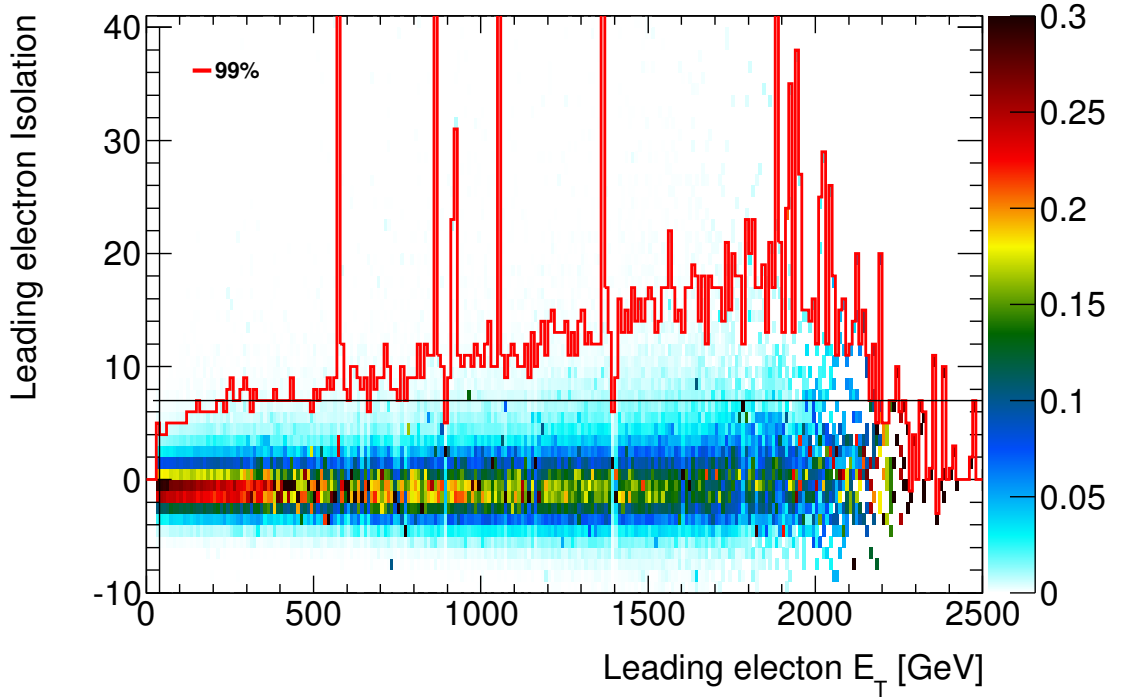


Figure 5.1: Distribution of DY MC in  $E_T$  and cluster isolation for the highest energy electron. Colour density shows the fraction of electrons from that  $E_T$  column found in the cell. The red line shows the 99% acceptance point of electrons in the  $E_T$  column. While the black vertical and horizontal lines show the  $p_T$  and old isolation cut respectively.

### 5.3 Opposite Sign requirement

The opposite sign requirement was introduced to the analysis specifically due to the use of  $\cos\theta^*$  in the search. As specified in section 1.2.1 selection of the electron and not the positron is important for the definition of  $\cos\theta^*$  and if reversed would dilute the asymmetry seen in the SM and CI LR signal as seen in figure 1.5. The effect of swapping charge at reconstruction level comes about due to two main effects, very high energy electrons with very straight tracks getting miss identified and hard bremsstrahlung from an electron undergoing decay to an electron pair which the wrong electron getting identified. These are not a small effect at high dielectron mass (15%) and so the requirement is introduced to solve the issue of miss identification. The effect of both electrons being miss identified was studied and found to have only a small chance. This requirement also does a good job in the exclusion of the Multijet background reducing by 50% throughout the signal region. The effect of the loss of acceptance attributed to this requirement is discussed in section

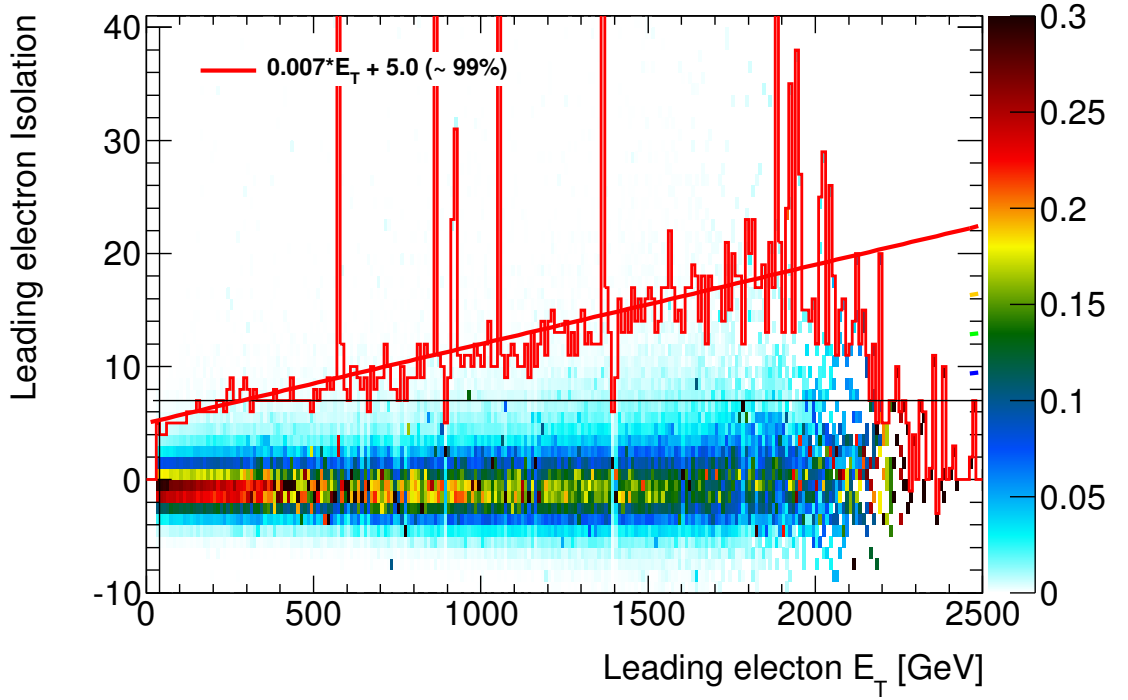


Figure 5.2: Similar plot to figure 5.1 but with a fit to 99% efficiency suggested as a possible isolation requirement.

8.2.1. As this requirement has an error associated with it a systematic is introduced to accommodate this (see section 8.1).

## 5.4 Energy Scale Correction

During the selection process an additional correction to the energy of electrons is applied that is not included in the reconstruction. This addition comes from a study done by the ATLAS electron and photon performance group at the end of the data run calibrating energies within the Z boson peak [62]. This results in a array of energy scale corrections distributed in  $E_T$  and  $\eta$  and applied before electron selection.

## 5.5 Selection Acceptance $\times$ Efficiency

Table 5.1 shows the efficiency of each part of the event selection. It can be seen that the opposite charge requirement causes a 7% drop in acceptance rate in the signal region.

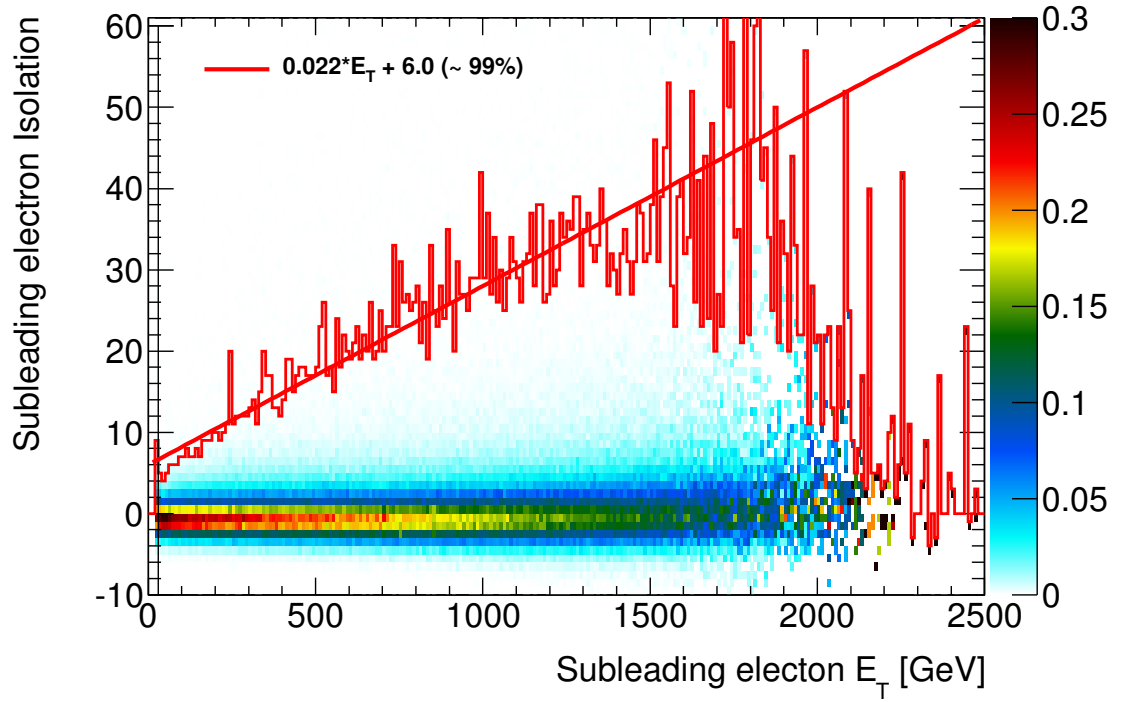


Figure 5.3: Similar plot to figure 5.2 but for second highest energy electrons after the 99% isolation efficiency selection is applied to the highest energy electron.

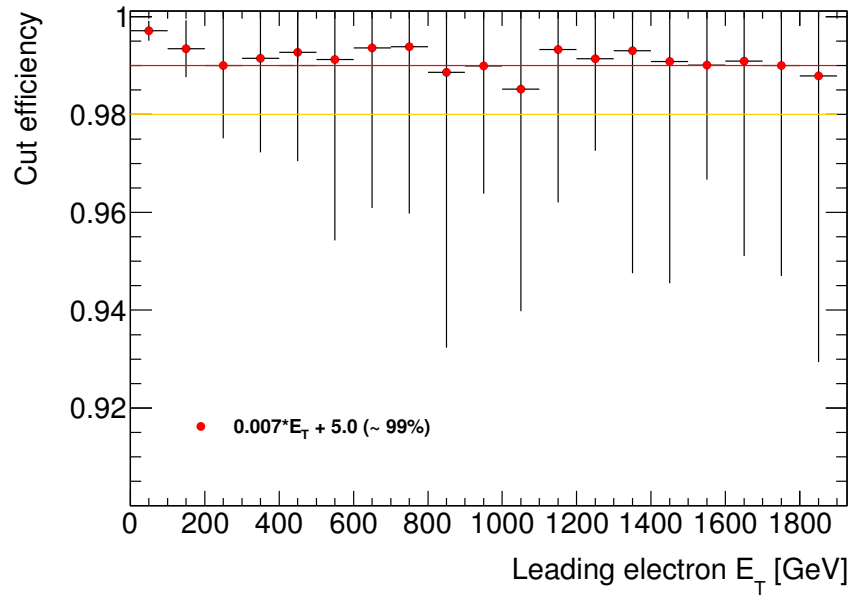


Figure 5.4: Efficiency of new leading electron isolation cut on selection of signal MC. Red and orange lines indicate the 99% and 98% efficiency levels respectively.

Although a lot it can be seen in section 8.2.1 that the effect of this drop is accommodated for by the new angular search introduced in this analysis and the reason for the selection.

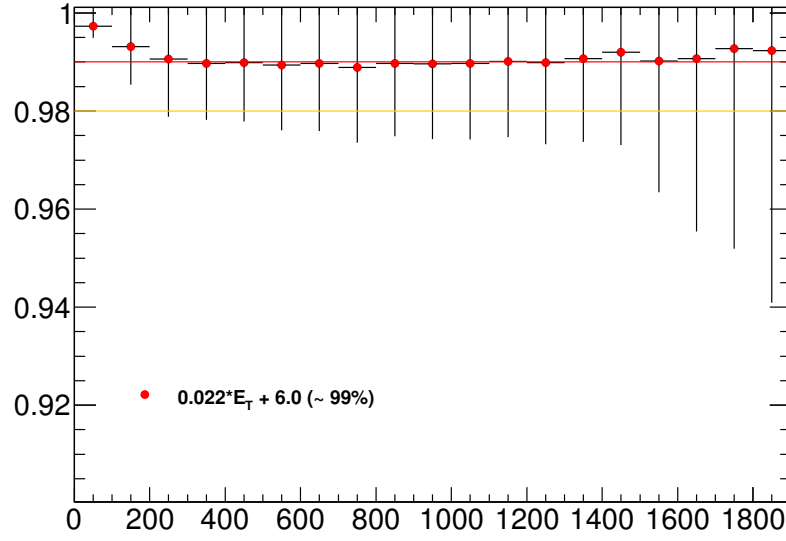


Figure 5.5: Efficiency of new subleading electron isolation cut on selection of signal MC. Red and orange lines indicate the 99% and 98% efficiency levels respectively.

Criterion	Relative Eff [%]	Cumulative Eff [%]
Trigger	$90.36 \pm 0.03$	$90.36 \pm 0.03$
$\eta$	$96.97 \pm 0.02$	$87.51 \pm 0.03$
$p_T$	$94.14 \pm 0.02$	$82.38 \pm 0.03$
Shower Shape	$90.37 \pm 0.03$	$74.45 \pm 0.04$
Isolation	$97.76 \pm 0.02$	$72.78 \pm 0.04$
Charge	$90.43 \pm 0.03$	$65.81 \pm 0.04$

Table 5.1: The efficiency of event selection on DY MC within the signal region above 400 GeV. DY MC is used due to higher statistics but is indistinguishable from signal with respect to analysis selection. Selection of number of primary vertices, of two highest  $p_T$  electrons and the invariant mass requirement of omitted due to near 100% acceptance on MC. Statistical errors are included only as a guide.

---

## Chapter 6

# Background Estimate

This chapter discusses methods used to estimate background processes to the signal. These background processes can be split up in to two categories; reducible and irreducible. Irreducible backgrounds consist of those background almost indistinguishable from our signal process namely clean high energy dielectron decays such as decays of the Z boson and the Drell-Yan (DY) spectrum. DY ( $q\bar{q} \rightarrow Z/\gamma^* \rightarrow \ell^-\ell^+$ ) is the largest background process and also interferes with the signal processes. Another irreducible background also estimated is the Photon-Induced processes ( $\gamma\gamma \rightarrow \ell^-\ell^+$ ) coming from the collision of two photons. Reducible backgrounds are those that can be reduced through event selection and three are included in this analysis. These reducible backgrounds consist of Top precesses, collisions creating single top quarks and  $t\bar{t}$  events which decay to include two electrons; Di-boson events, the creation of WW, WZ and ZZ events that decay in to two electron events; and finally Multi-jet & W+jets events where one or more electron signature is faked by jet objects. All of these backgrounds are estimated via Monte Carlo generators except for the Multi-jet & W+jets background which is estimated via a data-driven fake factor method. All background samples are summed together to create the full background estimate. MC samples are then scaled to the integrated luminosity of data collected in 2012 which is  $20.3 \text{ fb}^{-1}$ . Within the Z boson peak region (80 - 120 GeV) where it is known no new physics is found MC samples are scaled to data minus the multijet sample in order to rule out luminosity errors. This scale factor is found to be 1.048. Detailed below is the full derivation of the background estimates ready for comparison to data.

## 6.1 Monte Carlo samples

Monte Carlo (MC)<sup>1</sup> samples are produced centrally within ATLAS using MC generators specific to the generated sample which then undergo detector simulation using GEANT 4 [58] which produces a data format identical to a readout from the ATLAS detector plus additional “truth” parameters from the original MC generation. The samples then undergo the same reconstruction as data events within ATHENA producing a MC sample ready to be analysed the same as data.

### Drell-Yan

The Drell-Yan (DY) background is produced using the POWHEG + PYTHIA generator which is a next to leading order (NLO)<sup>2</sup> generation with POWHEG [63, 64] with event showering handled by PYTHIA 8 [65]. The parton density function (PDF) used is CT10 [66]. A K-factor is then used in order to weight the cross-section from NLO to next to next to leading order (NNLO). This NNLO K-factor is derived using FEWZ [67] which uses the MSTW2008 NNLO PDF [68] from which a QCD+EW mass-dependent K-factor is obtained. The DY sample is split in to 16 MC truth dilepton mass bins with bin edges at (60, 120, 180, 250, 400, 600, 800, 1000, 1250, 1500, 1750, 2000, 2250, 2500, 2750, 3000) GeV. The first bin from 60 - 120 GeV is a very high statistics sample providing a low statistical uncertainty for the region used for scaling MC in the Z boson peak.

### Photon-Induced

The Photon-Induced (PI) fraction is estimated via PYTHIA 8 [65] generator with the LO PDF MRST2004QED [69]. This sample is split in to 5 dilepton mass bins with bin edges at (60, 200, 600, 1500, 2500) GeV.

### Diboson

The Diboson MC sample is produced using HERWIG 6.510 [70] with the LO PDF CTEQ6L1 [71]. The sample is split in to the three process, WW, WZ and ZZ, with each process split in

---

<sup>1</sup>Computer algorithm designed to simulate physical systems using random sampling to obtain results for a statistical physics theories such as quantum field field theories

<sup>2</sup>LO, NLO and NNLO refer to the complexity of feynman diagrams considered when calculating the cross section of an interaction

to 3 mass-binned samples with bin edges of (60, 400, 1000) GeV. The sample is then scaled to NLO in a mass-independent way using MCFM [72] with the PDF MSTW2008 NLO [68]

### Top

The top sample is estimated using MC@NLO 3.41 [73] with NLO PDF CT10 [66] to generate matrix elements with JIMMY 4.31 [74] describing parton interactions and HERWIG [70] deriving the underlying event and parton showers. Both  $t\bar{t}$  and single Top processes are generated in two inclusive samples. A NNLO QCD K-factor is also derived using Top++ 2.0 [75, 76]. The top sample also undergoes a fit at high mass where the MC has low statistics. A dijet function ( $c_0 x^{c_1} x^{c_2 \log x}$ ) is used to fit between 200 - 700 GeV then the sample is cut at 500 GeV above which the dijet fit is used.

#### 6.1.1 MC Corrections

Corrections are applied to MC sample due to several factors including unknown run conditions within the ATLAS detector due to MC samples being run before the LHC run as well as known inefficiencies in the reconstruction of MC events. Below are listed all of the corrections which are applied on an event by event basis during the analysis of MC samples.

##### Pile-up Correction

Pile-up (PU) is the number of simultaneous proton-proton interactions within an event. MC samples are produced with a broad range of PU values which then get weighted according to run conditions within the detector. PU conditions can change throughout data taking and so the PU correction is specified for a particular set of ATLAS data. The distributions MC is weighted to can be seen in figure 4.1.

##### Vertex Position Reweighting

Vertex position is hard to predict pre-run and can therefore be weighted later once run conditions are known. This correction is not widely used within ATLAS due to its minimal effect however it was found to add better data background agreement to the  $\cos\theta^*$  distribution within the scaling and control region. The vertex position reweighting was found to have a minimal effect on the invariant mass distribution.

### Energy Smearing Correction

The energy smearing correction is used to better estimate the energy of electron signatures. This correction is derived from a Z peak calibration study [62] done within the ATLAS electron and photon performance group and matches MC to data. These corrections provide a  $\eta$  and  $E_T$  dependent smearing value applied to electron energy before electron selection.

### Electron Efficiency Scale Factor

The electron photon performance group also identified inefficiencies in electron reconstruction and identification. These form a set of scale factors applied in bins of  $E_T$  and  $\eta$  after event selection.

### Isolation and Trigger Scale Factor

Data/MC comparison for the isolation selections and the trigger requirements highlighted minor differences between data and MC. The differences were found to be below 1% yet a uniform scale factor accommodating this were applied after event selection for completeness.

## 6.2 Fake Factor Multi-Jet Estimate

One of the major sources of background to di-electron signals are di-jets or electron+jets (mainly W+jets) events where one or both selected leptons are jets faking electron signatures. The method for estimating this background, described here, is a “fake factor” or “matrix-method”. This is a data-driven method where electrons are selected by a tight ( $N_{tight}$ ) and loose ( $N_{loose}$ ) selection. The tight selection is the standard electron selection used in this analysis while the loose selection has no isolation requirement and must only pass a loose++ egamma definition (see section 4.1) with no track matching criteria.  $N_{tight}$  is therefore by design a subset of  $N_{loose}$ . Two more hidden variables are also assigned, *real* and *fake* referring to true source of each electron. This gives us two coefficients to determine from data.



$$f = \frac{N_{tight}^{fake}}{N_{loose}^{fake}} \quad r = \frac{N_{tight}^{real}}{N_{loose}^{real}} \quad (6.1)$$

The fake rate  $f$  denotes the probability that a *fake* electron which passes the loose requirement also passes tight while  $r$  refers to the probability that a *real* electron which passes the loose requirement also passes the tight. Reconstructed events are split in to two distinct groups, tight( $T$ ), and loose while failing tight( $L$ ), where *Tight* is now no longer a subset of *Loose*. This allows the reconstructed events to be related to the underling truth events via a matrix of fake rates shown in equation 6.2.

$$\begin{pmatrix} N_{TT} \\ N_{TL} \\ N_{LT} \\ N_{LL} \end{pmatrix} = \begin{pmatrix} r_1 r_2 & r_1 f_2 & f_1 r_2 & f_1 f_2 \\ r_1(1-r_2) & r_1(1-f_2) & f_1(1-r_2) & f_1(1-f_2) \\ (1-r_1)r_2 & (1-r_1)f_2 & (1-f_1)r_2 & (1-f_1)f_2 \\ (1-r_1)(1-r_2) & (1-r_1)(1-f_2) & (1-f_1)(1-r_2) & (1-f_1)(1-f_2) \end{pmatrix} \begin{pmatrix} N_{RR} \\ N_{RF} \\ N_{FR} \\ N_{FF} \end{pmatrix} \quad (6.2)$$

The first index in equation 6.2 refers to the highest  $p_T$  electron while the second index refers to the second highest  $p_T$  electron. So  $N_{LT}$  indicates the reconstructed events with highest  $p_T$  electron only passing the *Loose* selection while the second highest  $p_T$  electron passes *Tight* selection. The indices 1 and 2 refer to fake rates ( $f$ ) and efficiencies ( $r$ ) on leading and sub-leading electrons respectively.

The interesting part for this study is the contribution to  $N_{TT}$  coming from sources other than  $N_{RR}$ , these can be seen in equation 6.3.

$$\begin{aligned} N_{TT}^{\ell+jets} &= r_1 f_2 N_{RF} + f_1 r_2 N_{FR} \\ N_{TT}^{di-jets} &= f_1 f_2 N_{FF} \\ N_{TT}^{\ell+jets \text{ \& } di-jets} &= r_1 f_2 N_{RF} + f_1 r_2 N_{FR} + f_1 f_2 N_{FF} \end{aligned} \quad (6.3)$$

This function however contains unknown variables and so equation 6.2 is inverted to derive a better formalism in equation 6.4.

$$\begin{pmatrix} N_{RR} \\ N_{RF} \\ N_{FR} \\ N_{FF} \end{pmatrix} = \alpha \begin{pmatrix} (f_1 - 1)(f_2 - 1) & (f_1 - 1)f_2 & f_1(f_2 - 1) & f_1f_2 \\ (f_1 - 1)(1 - r_2) & (1 - f_1)r_2 & f_1(1 - r_2) & -f_1r_2 \\ (r_1 - 1)(1 - f_2) & (1 - r_1)f_2 & r_1(1 - f_2) & -r_1f_2 \\ (1 - r_1)(1 - r_2) & (r_1 - 1)r_2 & r_1(r_2 - 1) & r_1r_2 \end{pmatrix} \begin{pmatrix} N_{TT} \\ N_{TL} \\ N_{LT} \\ N_{LL} \end{pmatrix} \quad (6.4)$$

where,

$$\alpha = \frac{1}{(r_1 - f_1)(r_2 - f_2)} \quad (6.5)$$

The fraction of selected events with at least one fake is then given by equation 6.3 resulting in equation 6.6.

$$\begin{aligned} N_{TT}^{\ell+jets \text{ \& } di-jets} = & \alpha r_1 f_2 [(f_1 - 1)(1 - r_2)N_{TT} + (1 - f_1)r_2 N_{TL} + f_1(1 - r_2)N_{LT} - f_1 r_2 N_{LL}] \\ & + \alpha f_1 r_2 [(r_1 - 1)(1 - f_2)N_{TT} + (1 - r_1)f_2 N_{TL} + r_1(1 - f_2)N_{LT} - r_1 f_2 N_{LL}] \\ & + \alpha f_1 f_2 [(1 - r_1)(1 - r_2)N_{TT} + (r_1 - 1)r_2 N_{TL} + r_1(r_2 - 1)N_{LT} + r_1 r_2 N_{LL}] \end{aligned} \quad (6.6)$$

$$\begin{aligned} = & \alpha [r_1 f_2 (f_1 - 1)(1 - r_2) + f_1 r_2 (r_1 - 1)(1 - f_2) + f_1 f_2 (1 - r_1)(1 - r_2)] N_{TT} \\ & + \alpha f_2 r_2 [r_1(1 - f_1) + f_1(1 - r_1) + f_1(r_1 - 1)] N_{TL} \\ & + \alpha f_1 r_1 [f_2(1 - r_2) + r_2(1 - f_2) + f_2(r_2 - 1)] N_{LT} \\ & - \alpha f_1 f_2 r_1 r_2 N_{LL} \end{aligned} \quad (6.7)$$

Equation 6.7 shows the derived formula relating the multi-jet background to fake rates, efficiencies and four independent samples  $N_{TT}$ ,  $N_{TL}$ ,  $N_{LT}$  and  $N_{LL}$  which can be selected from data. Following are the details of this method used on the full  $20 \text{ fb}^{-1}$  of integrated luminosity from ATLAS's 2012 run. This method was developed centrally in the resonant analysis which the author then applied and tested for this non-resonant analysis.

### 6.2.1 Real Electron Efficiency Estimation

The real electron efficiency is defined in equation 6.1 as  $r = N_{tight}^{real}/N_{loose}^{real}$ . This is determined from MC using a mass binned Drell-Yan sample. The efficiencies are found for both the leading and sub-leading electrons and binned in eight  $p_T$  and three eta bins of  $|\eta| < 1.37$  (barrel),  $1.52 < |\eta| < 2.01$  and  $2.01 < |\eta| < 2.47$  (endcap). The efficiency is distributed between 90 - 96% as is shown in figure 6.1.

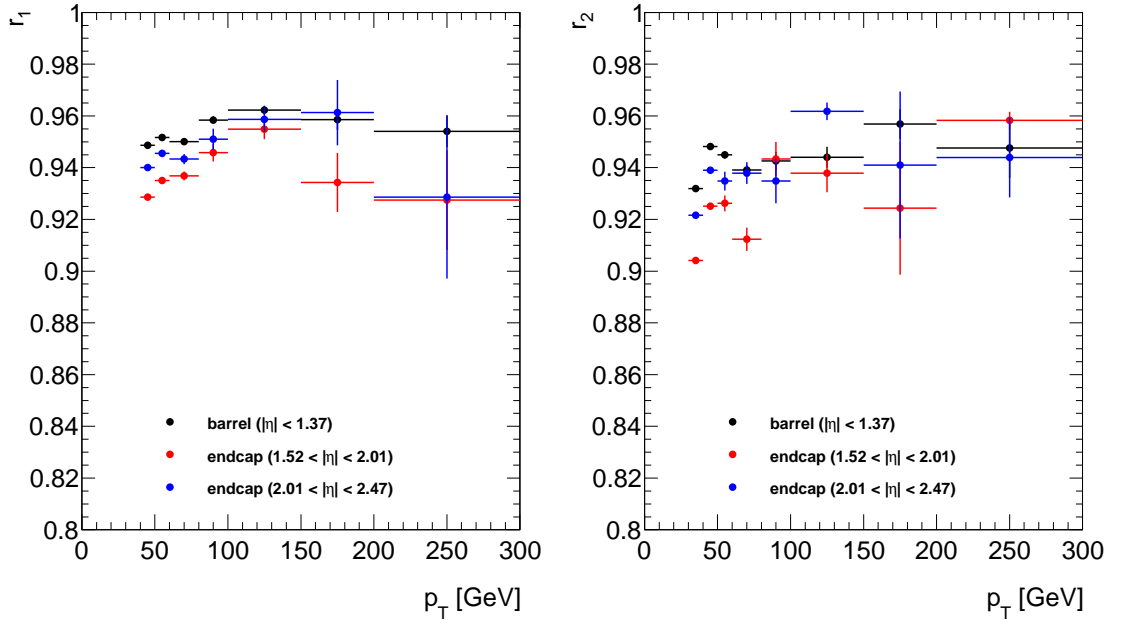


Figure 6.1: Real electron efficiencies obtained from Drell-Yan MC and binned in  $p_T$  and three coarse  $\eta$  bins covering the barrel and two endcap regions. Efficiencies for leading electrons are shown on the left while those for subleading electron are on the right.

### 6.2.2 Fake Electron Rate Estimation

The default method selected for analysing the fake rates is a single object method selection on the jet stream data. This has the advantage of more statistics and a higher energy reach compared to methods such as using tag and probe on the egamma stream data. An array of triggers are used for selecting suitable events with many different thresholds. Events are associated to groups with the lowest trigger threshold they pass as each trigger has a different prescale. Objects are selected with jet algorithms and then matched to objects in the egamma stream with a  $\Delta R < 0.1$ . Two further steps are taken to suppress real

electrons from W decays and real Drell-Yan events. A veto of  $E_{Tmiss} > 25 \text{ GeV}$  is introduced to combat the former while events with two medium++ or loose++ electrons with  $|m_{tag \& probe} - 91 \text{ GeV}| < 20 \text{ GeV}$  are vetoed to counter the real Drell-Yan.

The fake rate as defined in equation 6.1 ( $f = N_{tight}^{fake}/N_{loose}^{fake}$ ) with the  $N_{tight}^{fake}$  and  $N_{loose}^{fake}$  distributions selected using the standard event selection on the matched egamma objects. Due to the different prescales of each trigger a separate set of fake rates are calculated for each trigger, these are then combined as a weighted average of all fake rates. Figure 6.2 shows the distribution of fake rates for leading and subleading fakes. These are distributed between 3 - 20%.

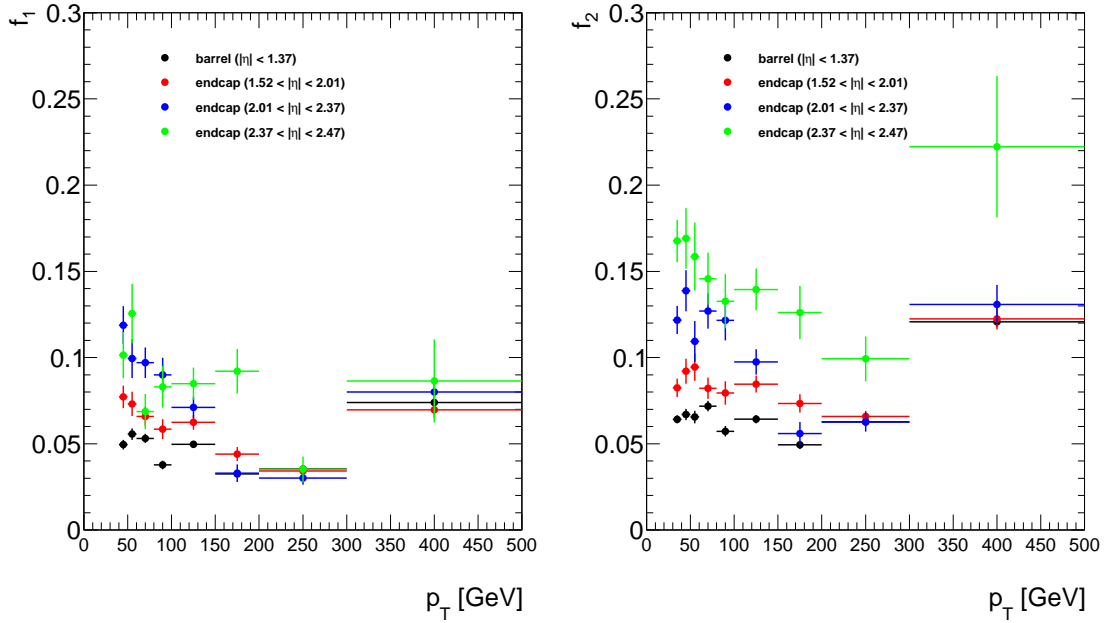


Figure 6.2: Fake rates obtained from data and binned in  $p_T$  and four coarse  $\eta$  bins covering the barrel and three endcap regions. Fake rates for leading electrons are shown on the left while those for subleading electron are on the right.

### 6.2.3 Properties of Multi-Jet Background

In order to compose the final sample data events are organised by the distributions  $N_{TT}$ ,  $N_{TL}$ ,  $N_{LT}$  or  $N_{LL}$  and weights are applied according to each electrons  $p_T$  and  $\eta$  with respect to equation 6.7 and the corresponding efficiencies and fake rates. Figure 6.3 shows these distributions before the efficiencies and fake rates are applied to weight to the final background prediction. This method is not suited to predicting the Multi-Jet background in the

Z peak region due to contamination of Z boson decays and so a fit is obtained between 120 GeV and 400 GeV and stitched from 110 GeV and below. This gives a good estimate to the integral in this region for use in scaling MC's to luminosity but is not predicted to be good at predicting other variables in this region. At high-mass statistics of the sample decline and so an additional fit is made a high mass with the lower edge of the fit varied between 425 and 600 GeV and the upper edge from 700 to 1200 GeV, with the fit used above 500 GeV.

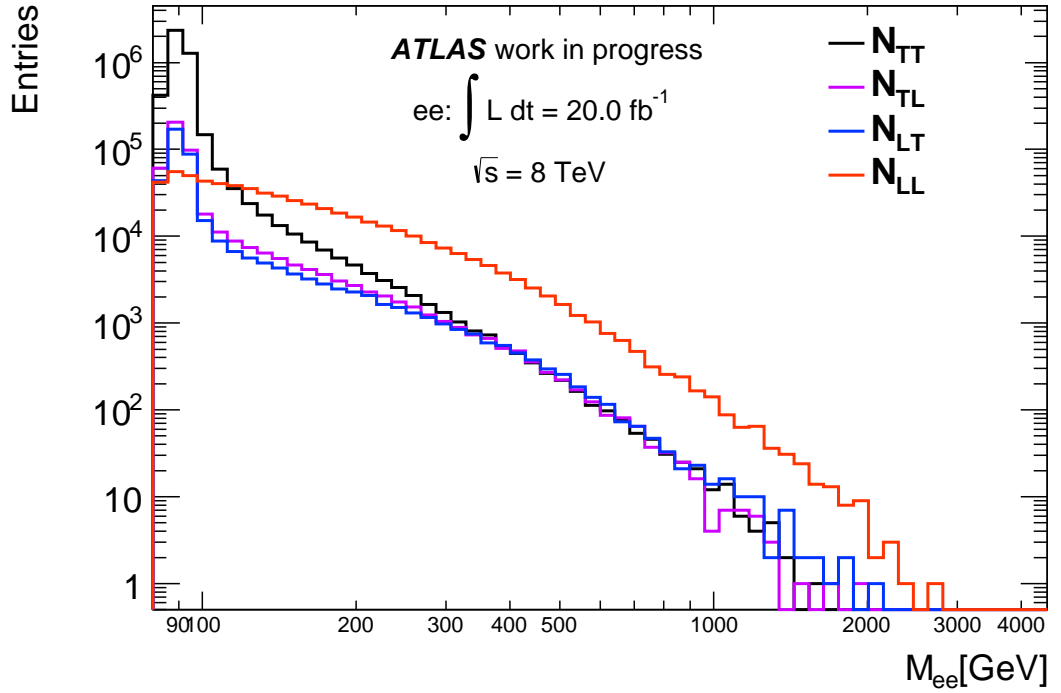


Figure 6.3: Distribution of  $N_{TT}$ ,  $N_{TL}$ ,  $N_{LT}$  and  $N_{LL}$  distributions from data with no weightings applied.

#### 6.2.4 Other Methods and Estimation of Error

Two other methods and variations upon them were used to test the validity of this method as well as estimate the systematic error of this background estimation procedure. These two methods are both tag and probe measurements; one on the jet stream of data, and another on the egamma stream where the method is more an “inverse” tag and probe with the selection of a tag with high probability of being a jet. Variations are also made on the method by

assuming  $r_1$  and  $r_2 = 1.0$  in all cases as well as changing the definition of loose but fail tight. These variations simplify the equations slightly but the method remains the same. Variations compared to the default method used to obtain the estimation were found to vary between  $\pm 20\%$  throughout the invariant mass distribution. The systematic uncertainty of the multi-jet estimate was therefore taken to be a flat 20% throughout the distribution.

### 6.3 Total Background Estimate

The total stacked summation of all the backgrounds, after all corrections and scaling within the Z peak have been applied, can be seen in figure 6.4.

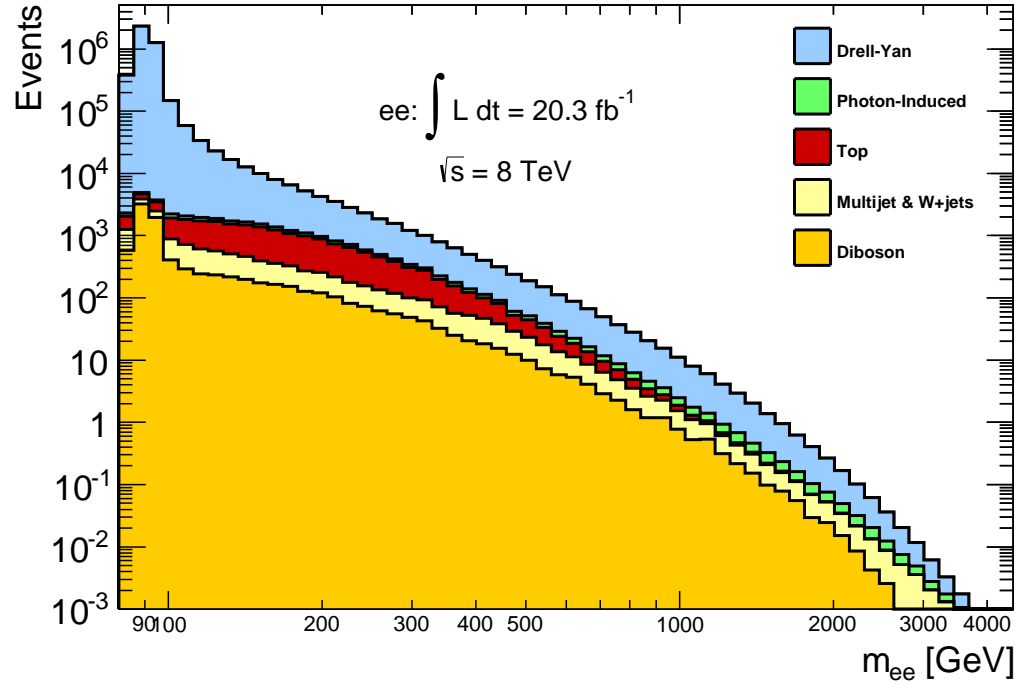


Figure 6.4: Combined background samples scaled to data in the Z peak.

---

# Chapter 7

## Signal and Results

This chapter discusses the MC generators used to model signal distributions and how these are parametrised for input to the statistical analysis. This is followed by the results of the data background comparison looking for any sign of new physics signal.

### 7.1 Signal Monte Carlo

All signal MC is produced in the same way as the background MC and then summed with the other background predictions to arrive at the full signal prediction. Each sample also gets scaled by the same factor as the background MC from the Z peak scaling.

#### Contact Interaction

Contact Interaction samples are generated using PYTHIA 8 [65] with the leading order PDF MSTW2008LO [68]. The CI MC samples also have a K-factor applied that is derived in the same way as the DY K-factor but scaling from LO to NNLO (see section 6.1). A selection of  $\Lambda$  values was chosen to cover the reach in new physics for all formalisms of the model (LL, LR and RR). This constitutes signals for  $\Lambda = 7, 10, 14, 20$  and  $28$  TeV. For each of these working points parametrisations of constructive and destructive interference and LL, LR and RR models are all generated. This makes 6 parametrisations with 5  $\Lambda$  values produced for each one. Each MC sample is composed of three dilepton mass binned samples above 300 GeV in order to maintain statistics. Below 300 GeV negligible new

physics is predicted and so the SM DY prediction is used below this point. Because this MC sample is LO a PYTHIA 8 LO DY sample is also produced. This sample models the DY in the same way as the signal samples allowing you to subtract it from the signal samples to leave a pure new physics signal sample. This signal sample can then be added to the other background samples including the background MC DY sample (seen in section 6.1) to give a full signal prediction with a more consistent and higher statistics DY sample.

## ADD

The ADD samples used are produced using the SHERPA 1.4.1 [77] generator and NLO PDF CT10 [66]. Only two formalisms are produced as limits for other formalisms can be converted from the GRW one. The only formalism this is not possible for is HLZ ( $n = 2$ ). For these 2 formalisms 4 values of  $M_s$  are generated of  $M_s = 4.75, 4.0, 3.75$  and  $3.5$  TeV. Again 3 dilepton mass bins are used above 300 GeV with the SM DY replacing the distribution below this. Also, like the CI samples, a specific DY only SHERPA sample is produced which is then subtracted from the signal samples so the background MC DY can be used.

## 7.2 Signal Parametrisation

Each formalism of the CI and ADD model is parametrised according to the form of their individual cross-sections (Eq's 1.5 and 1.7) and as a function of their parameter of interest ( $\Lambda, M_s$ ). The parametrisations are a prediction of number of expected events  $N_{\text{exp}}$  where the parameter of interest ( $\Lambda, M_s$ ) at  $\infty$  equates to no signal and just the SM background prediction, these can be seen in equations 7.1 and 7.2.

$$N_{\text{exp}}(\Lambda) = c_0 + \frac{c_1}{\Lambda^2} + \frac{c_2}{\Lambda^4} \quad (7.1)$$

$$N_{\text{exp}}(M_s) = c_0 + \frac{c_1}{M_s^4} + \frac{c_2}{M_s^8} \quad (7.2)$$

Here  $c_0$  refers to the SM background prediction while  $c_1$  and  $c_2$  show the dependence of the scale of new physics on number of expected events. Each formalism gets parametrised



in every search bin. These search bins are described at the start of chapter 8 while the parametrisations can be seen in figure 7.1 for every CI mass bin. The full list of all of the parametrisations used can be found in appendix B.

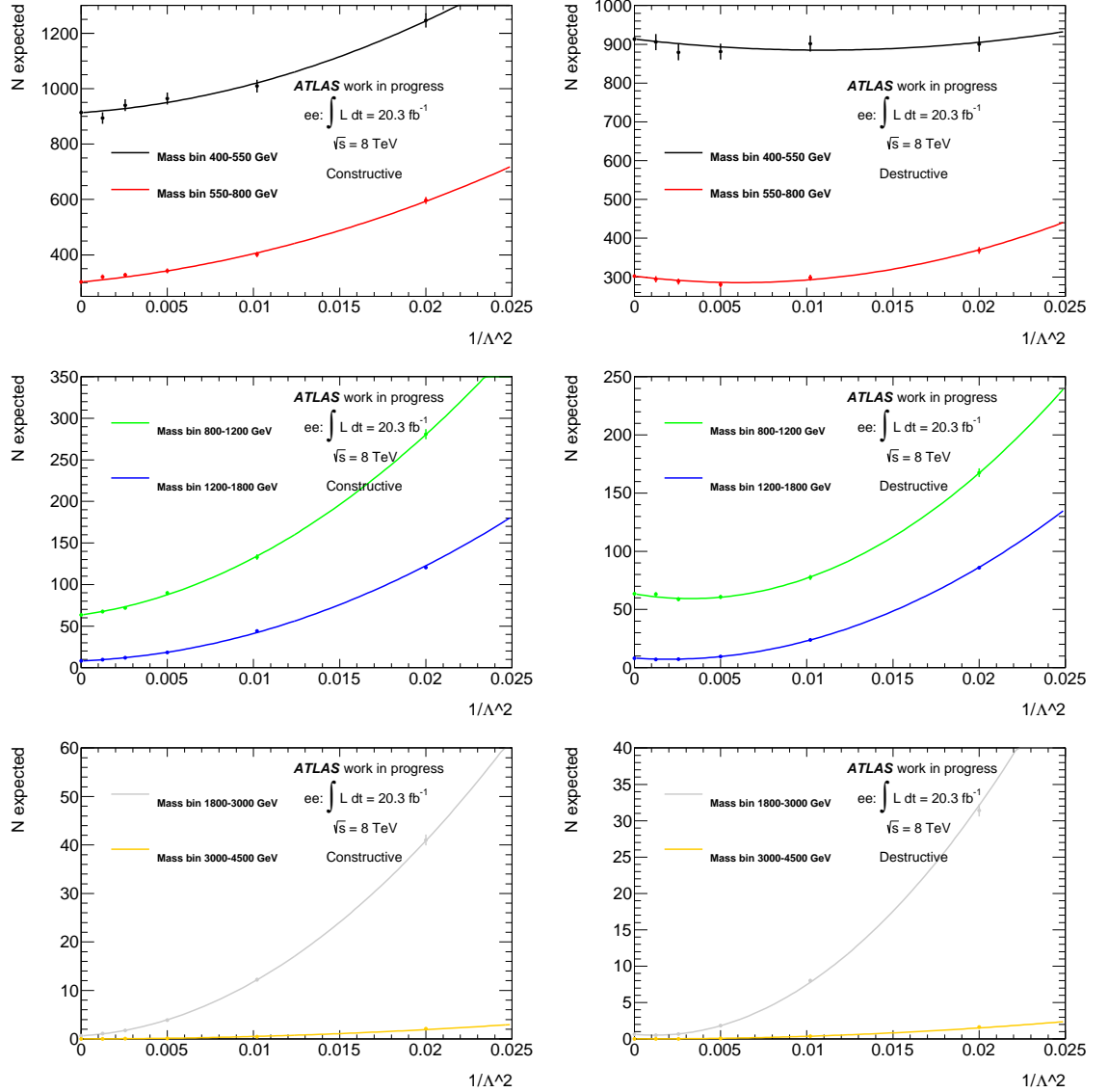


Figure 7.1: Parametrisations of the CI signal for number of expected events as a function of  $\Lambda$  according to equation 7.1 and for each CI mass bin.

## 7.3 Results

Following are full results of the event selection for observed data, predicted background and some example signal models. Figures 7.2 and 7.3 show the distributions of the two

main search variables dielectron invariant mass and  $\cos\theta^*$ . A comparison between data and background is given with the expected shapes of some signal models shown for comparison. Ratio's are also shown between data and background along with a band showing the size of the total systematic uncertainty as described in section 8.1. Figure 7.4 then shows forward backward asymmetry ( $A_{FB}$ ) defined in equation 1.4. Statistical errors on the data points are calculated using the function  $\Delta A_{FB} = \sqrt{(1 - A_{FB}^2)/N}$  where  $N$  is the number of events in both the forward and backwards regions. The ratio shown in figure 7.4 is the difference between data and background  $A_{FB}$  values,  $\Delta$ , divided by the total systematic uncertainty found in that bin,  $\sigma$ . It can be seen that data favours the angular dependence of the SM prediction or the CI LL formalism with no divergence similar to the CI LR formalism. In figure 7.5 control plots are seen showing electron  $p_T$ ,  $\eta$  and  $\phi$ . More results and control plots can be found in appendix A. Lastly tables 7.1, 7.2, 7.3 and 7.4 show the full extracted results acceding through the search bins. Each invariant mass bin is shown as well as the forward and backwards regions within each bin where forward refers to events with  $\cos\theta^*$  greater than 0 and backwards events with  $\cos\theta^*$  less than 0. The expected number of events is given for each of the background as well as a selection of CI signal formalisms and the data observed. Table 7.5 shows the results for the single ADD search search bin the same as the CI tables. The reason a single bin is used is discussed in chapter 8.

It can be seen from these results that no significant difference is seen between data observed and the background predicted. A slight discrepancy is seen between data and background in the 1200 - 1800 GeV invariant mass bin. The background predicts 10.8 events with a total systematic error of 1.6 events while only 7 events are observed in data. As seen later this doesn't signify a significant difference but has an effect on the limits set in chapter 8.

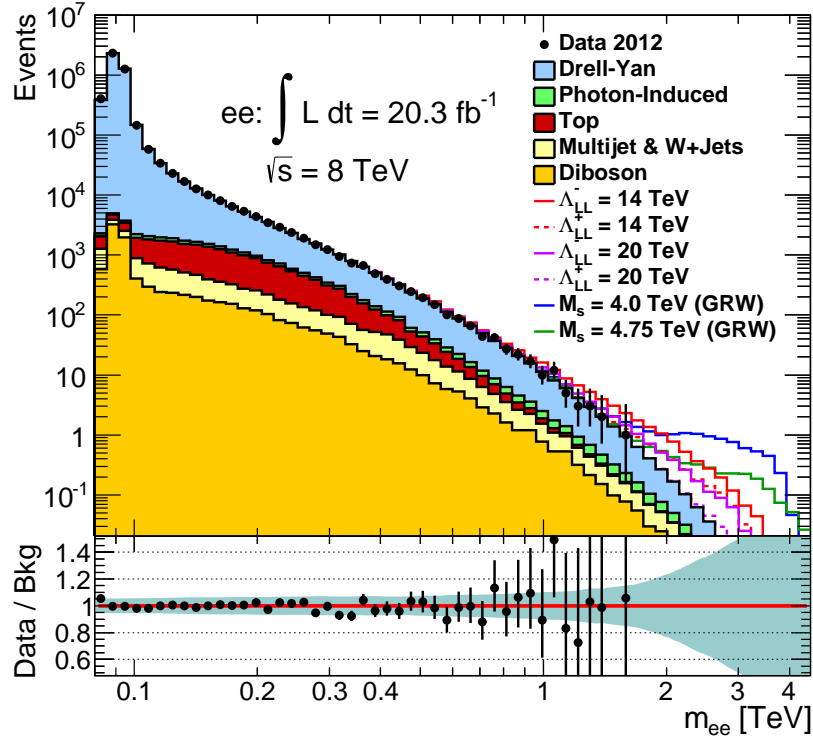


Figure 7.2: Dielectron invariant mass comparison between data and MC with possible signal overlays of CI and ADD. Ratio between data and background included with band showing size of total background systematic. The distribution has bin width constant in  $\log(m_{ee})$ .

Process	$m_{ee}$ [GeV]					
	All	120 - 200		All	200 - 400	
		Forward	Backward		Forward	Backward
Drell-Yan	72000 $\pm$ 5000	41500 $\pm$ 2600	31000 $\pm$ 2200	13100 $\pm$ 900	7900 $\pm$ 500	5200 $\pm$ 400
Top	6900 $\pm$ 400	3480 $\pm$ 210	3410 $\pm$ 210	2840 $\pm$ 170	1400 $\pm$ 90	1440 $\pm$ 90
Multijets & W+Jets	1650 $\pm$ 330	900 $\pm$ 180	780 $\pm$ 160	670 $\pm$ 130	330 $\pm$ 70	340 $\pm$ 70
Diboson	1330 $\pm$ 70	710 $\pm$ 40	619 $\pm$ 33	583 $\pm$ 31	331 $\pm$ 19	252 $\pm$ 15
Photon-Induced	1200 $\pm$ 1200	600 $\pm$ 600	600 $\pm$ 600	400 $\pm$ 400	230 $\pm$ 230	220 $\pm$ 220
Total SM	84000 $\pm$ 5000	47200 $\pm$ 2800	36400 $\pm$ 2500	17600 $\pm$ 1200	10200 $\pm$ 600	7400 $\pm$ 500
Data	83824	46910	36914	17525	10107	7418

Table 7.1: Comparison of background prediction to data. Binning covering the control region. Total systematic error is included on each number. See section 8.1 for details of systematics.

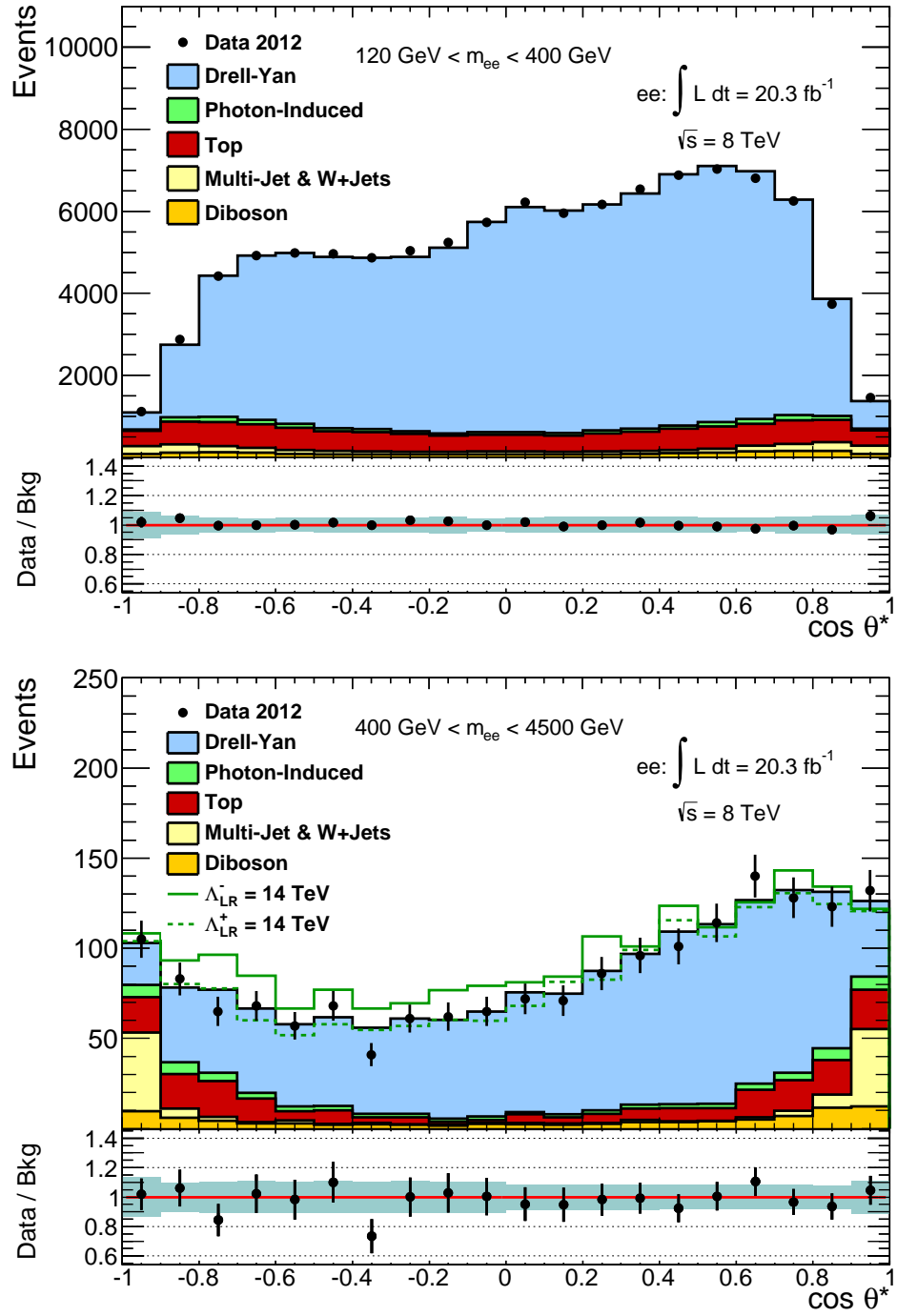


Figure 7.3:  $\cos\theta^*$  comparison between data and MC in control and signal regions with possible signal overlay of the CI LR formalism. Ratio between data and background included with band showing size of total background systematic.  $\cos\theta^*$  plots for each mass bin are found in appendix A.

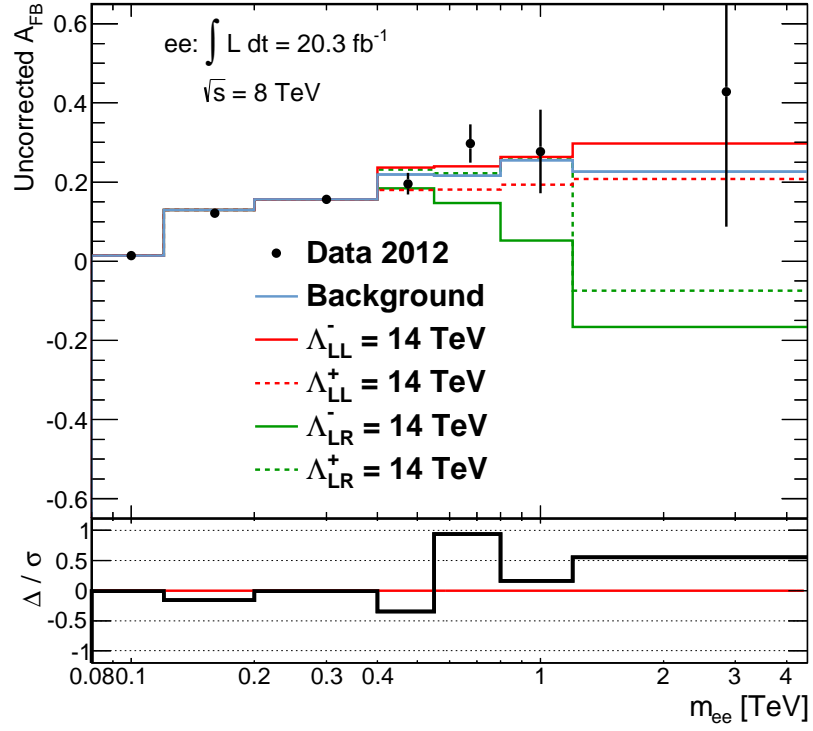
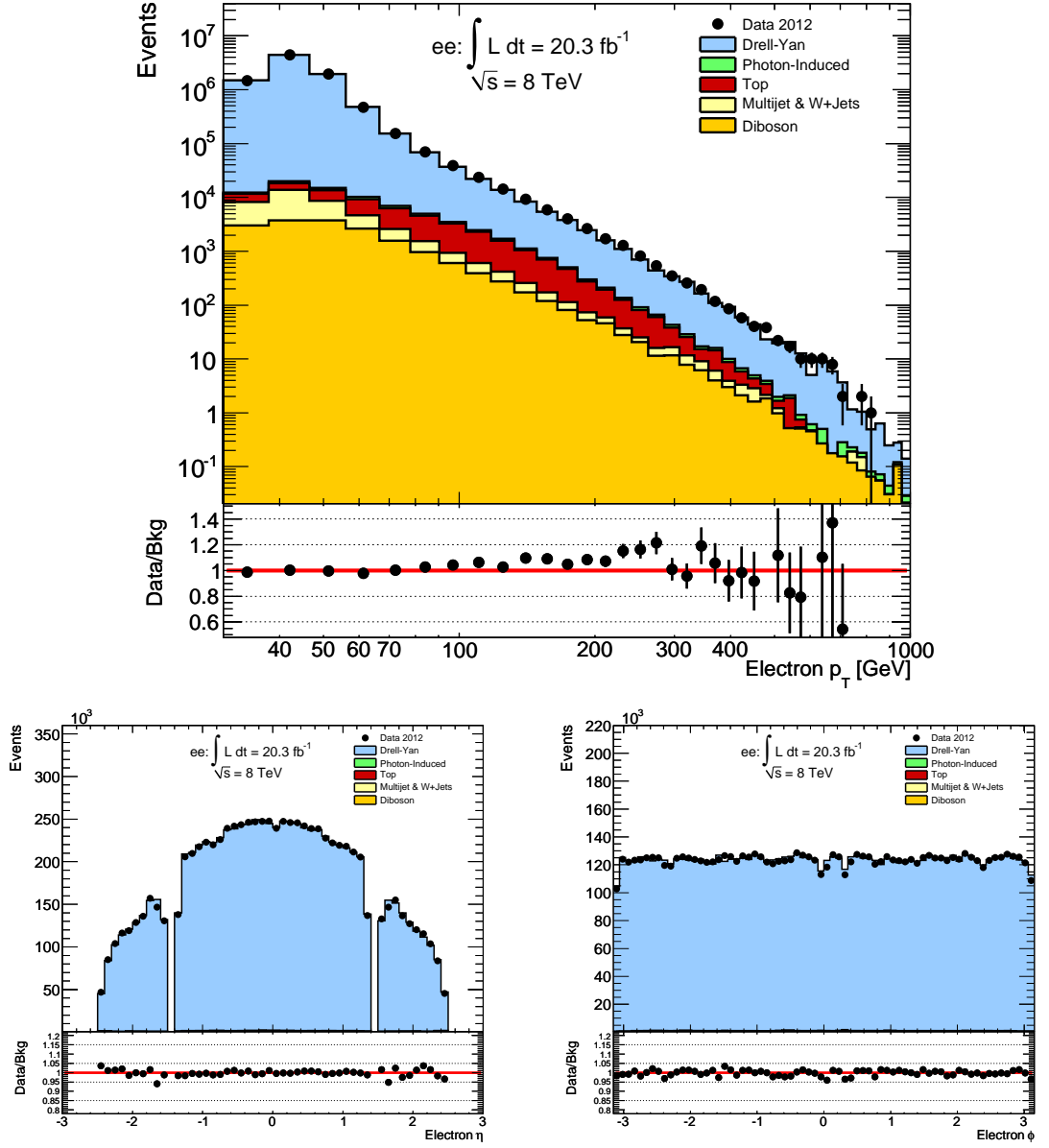


Figure 7.4:  $A_{FB}$  comparison between data and MC with possible signal overlay of CI. Ratio shows the difference between data and background prediction divided by total background systematic.

Process	$m_{ee}$ [GeV]					
	All	Forward	Backward	All	Forward	Backward
Drell-Yan	$910 \pm 70$	$580 \pm 40$	$333 \pm 32$	$302 \pm 25$	$193 \pm 13$	$109 \pm 12$
Top	$153 \pm 13$	$87 \pm 8$	$72 \pm 7$	$35.2 \pm 2.7$	$18.2 \pm 1.6$	$17.5 \pm 1.6$
Multijets & W+Jets	$88 \pm 18$	$43 \pm 9$	$45 \pm 9$	$27 \pm 6$	$13.0 \pm 3.0$	$13.0 \pm 3.1$
Diboson	$62.2 \pm 3.5$	$36.0 \pm 2.2$	$26.2 \pm 1.7$	$22.3 \pm 1.3$	$13.8 \pm 0.9$	$8.5 \pm 0.7$
Photon-Induced	$40 \pm 40$	$22 \pm 22$	$22 \pm 22$	$17 \pm 17$	$8 \pm 8$	$8 \pm 8$
Total SM	$1260 \pm 100$	$770 \pm 50$	$500 \pm 50$	$404 \pm 35$	$247 \pm 18$	$156 \pm 17$
Data	1262	754	508	388	251	137
SM+CI( $\Lambda_{LL}^{-14}$ )	$1310 \pm 110$	$810 \pm 60$	$510 \pm 50$	$440 \pm 40$	$276 \pm 22$	$167 \pm 18$
SM+CI( $\Lambda_{LL}^{-20}$ )	$1290 \pm 110$	$780 \pm 60$	$510 \pm 50$	$430 \pm 40$	$271 \pm 22$	$157 \pm 18$
SM+CI( $\Lambda_{LR}^{-14}$ )	$1340 \pm 110$	$790 \pm 60$	$550 \pm 50$	$460 \pm 40$	$266 \pm 22$	$195 \pm 19$
SM+CI( $\Lambda_{LR}^{-20}$ )	$1290 \pm 110$	$780 \pm 60$	$510 \pm 50$	$420 \pm 40$	$249 \pm 21$	$174 \pm 19$
SM+CI( $\Lambda_{RR}^{-14}$ )	$1310 \pm 110$	$810 \pm 60$	$510 \pm 50$	$440 \pm 40$	$276 \pm 22$	$167 \pm 18$
SM+CI( $\Lambda_{RR}^{-20}$ )	$1290 \pm 110$	$780 \pm 60$	$510 \pm 50$	$430 \pm 40$	$271 \pm 22$	$157 \pm 18$
SM+CI( $\Lambda_{LL}^{+14}$ )	$1230 \pm 110$	$730 \pm 60$	$510 \pm 50$	$380 \pm 40$	$227 \pm 21$	$155 \pm 18$
SM+CI( $\Lambda_{LL}^{+20}$ )	$1230 \pm 110$	$740 \pm 60$	$490 \pm 50$	$390 \pm 40$	$234 \pm 21$	$156 \pm 18$
SM+CI( $\Lambda_{LR}^{+14}$ )	$1200 \pm 110$	$740 \pm 60$	$470 \pm 50$	$400 \pm 40$	$247 \pm 21$	$154 \pm 18$
SM+CI( $\Lambda_{LR}^{+20}$ )	$1210 \pm 110$	$740 \pm 60$	$470 \pm 50$	$390 \pm 40$	$238 \pm 21$	$150 \pm 18$
SM+CI( $\Lambda_{RR}^{+14}$ )	$1230 \pm 110$	$730 \pm 60$	$510 \pm 50$	$380 \pm 40$	$227 \pm 21$	$155 \pm 18$
SM+CI( $\Lambda_{RR}^{+20}$ )	$1230 \pm 110$	$740 \pm 60$	$490 \pm 50$	$390 \pm 40$	$234 \pm 21$	$156 \pm 18$

Table 7.2: Comparison of background prediction to data with prediction of several CI signal models. Signal models are referred to showing constructive or destructive interference ( $-/+$  in superscript),  $\Lambda$  value (number in superscript) and formalism (letters in subscript). Binning used is the same as used for statistical analysis of CI model with the two lowest mass regions shown here. Total systematic error is included on each number. See section 8.1 for details of systematics.

Figure 7.5: Control plots of  $p_T$ ,  $\eta$  and  $\phi$  distributions of selected electrons.

Process	$m_{ee}$ [GeV]					
	800 - 1200			1200 - 1800		
	All	Forward	Backward	All	Forward	Backward
Drell-Yan	$63 \pm 6$	$41.4 \pm 3.4$	$22.1 \pm 2.9$	$8.2 \pm 1.2$	$5.3 \pm 0.6$	$2.9 \pm 0.6$
Top	$3.06 \pm 0.18$	$1.58 \pm 0.10$	$1.45 \pm 0.09$	$0.140 \pm 0.008$	$0.073 \pm 0.004$	$0.065 \pm 0.004$
Multijets & W+Jets	$5.8 \pm 1.5$	$2.6 \pm 0.9$	$2.5 \pm 0.8$	$0.87 \pm 0.32$	$0.35 \pm 0.16$	$0.32 \pm 0.24$
Diboson	$5.4 \pm 0.4$	$3.41 \pm 0.28$	$2.02 \pm 0.17$	$0.83 \pm 0.05$	$0.542 \pm 0.035$	$0.287 \pm 0.016$
Photon-Induced	$4 \pm 4$	$2.2 \pm 2.2$	$2.1 \pm 2.1$	$0.7 \pm 0.7$	$0.34 \pm 0.34$	$0.4 \pm 0.4$
Total SM	$82 \pm 9$	$51 \pm 5$	$30 \pm 4$	$10.8 \pm 1.6$	$6.6 \pm 0.7$	$4.0 \pm 0.8$
Data	84	53	31	7	5	2
SM+CI( $\Lambda_{LL}^{-14}$ )	$108 \pm 10$	$68 \pm 6$	$39 \pm 5$	$20.9 \pm 1.9$	$13.5 \pm 1.0$	$7.2 \pm 0.9$
SM+CI( $\Lambda_{LL}^{-20}$ )	$90 \pm 10$	$58 \pm 5$	$32 \pm 4$	$14.4 \pm 1.7$	$9.2 \pm 0.9$	$5.0 \pm 0.8$
SM+CI( $\Lambda_{LR}^{-14}$ )	$118 \pm 10$	$62 \pm 6$	$56 \pm 5$	$26.3 \pm 2.1$	$11.3 \pm 1.0$	$14.8 \pm 1.1$
SM+CI( $\Lambda_{LR}^{-20}$ )	$98 \pm 10$	$57 \pm 5$	$41 \pm 5$	$15.7 \pm 1.7$	$8.3 \pm 0.9$	$7.2 \pm 0.9$
SM+CI( $\Lambda_{RR}^{-14}$ )	$108 \pm 10$	$68 \pm 6$	$40 \pm 5$	$20.8 \pm 1.9$	$13.6 \pm 1.0$	$6.9 \pm 0.9$
SM+CI( $\Lambda_{RR}^{-20}$ )	$91 \pm 10$	$58 \pm 5$	$32 \pm 4$	$14.3 \pm 1.7$	$9.1 \pm 0.9$	$5.0 \pm 0.8$
SM+CI( $\Lambda_{LL}^{+14}$ )	$79 \pm 9$	$47 \pm 5$	$32 \pm 4$	$12.2 \pm 1.7$	$7.3 \pm 0.8$	$4.7 \pm 0.8$
SM+CI( $\Lambda_{LL}^{+20}$ )	$77 \pm 9$	$48 \pm 5$	$29 \pm 4$	$10.0 \pm 1.6$	$6.1 \pm 0.8$	$3.7 \pm 0.8$
SM+CI( $\Lambda_{LR}^{+14}$ )	$88 \pm 10$	$55 \pm 5$	$32 \pm 4$	$18.9 \pm 1.8$	$9.2 \pm 0.9$	$9.5 \pm 0.9$
SM+CI( $\Lambda_{LR}^{+20}$ )	$81 \pm 9$	$52 \pm 5$	$29 \pm 4$	$11.5 \pm 1.6$	$6.8 \pm 0.8$	$4.5 \pm 0.8$
SM+CI( $\Lambda_{RR}^{+14}$ )	$79 \pm 9$	$47 \pm 5$	$32 \pm 4$	$12.1 \pm 1.7$	$7.3 \pm 0.8$	$4.6 \pm 0.8$
SM+CI( $\Lambda_{RR}^{+20}$ )	$77 \pm 9$	$48 \pm 5$	$29 \pm 4$	$10.2 \pm 1.6$	$6.3 \pm 0.8$	$3.8 \pm 0.8$

Table 7.3: Comparison of background prediction to data with prediction of several CI signal models. Signal models are refereed to showing constructive or destructive interference (-/+ in superscript),  $\Lambda$  value (number in superscript) and formalism (letters in subscript). Binning used is the same as used for statistical analysis of CI model with the two mid mass regions shown here. Total systematic error is included on each number. See section 8.1 for details of systematics.

Process	$m_{ee}$ [GeV]					
	1800 - 3000			3000 - 4500		
	All	Forward	Backward	All	Forward	Backward
Drell-Yan	$0.64 \pm 0.17$	$0.41 \pm 0.09$	$0.23 \pm 0.08$	$0.006 \pm 0.004$	$0.0039 \pm 0.0021$	$0.0022 \pm 0.0018$
Top	$< 0.004$	$< 0.002$	$< 0.002$	$< 0.001$	$< 0.001$	$< 0.001$
Multijets & W+Jets	$0.11 \pm 0.04$	$0.040 \pm 0.020$	$0.033 \pm 0.027$	$0.0058 \pm 0.0012$	$< 0.002$	$< 0.001$
Diboson	$0.075 \pm 0.006$	$0.053 \pm 0.004$	$0.0224 \pm 0.0026$	$< 0.001$	$< 0.001$	$< 0.001$
Photon-Induced	$0.08 \pm 0.08$	$0.04 \pm 0.04$	$0.04 \pm 0.04$	$0.0016 \pm 0.0016$	$< 0.002$	$< 0.002$
Total SM	$0.91 \pm 0.21$	$0.55 \pm 0.10$	$0.33 \pm 0.10$	$0.014 \pm 0.005$	$0.0065 \pm 0.0026$	$0.0042 \pm 0.0022$
Data	0	0	0	0	0	0
SM+CI( $\Lambda_{LL}^{-14}$ )	$4.2 \pm 0.4$	$2.75 \pm 0.23$	$1.38 \pm 0.15$	$0.141 \pm 0.028$	$0.080 \pm 0.020$	$0.058 \pm 0.016$
SM+CI( $\Lambda_{LL}^{-20}$ )	$2.01 \pm 0.25$	$1.26 \pm 0.14$	$0.72 \pm 0.12$	$0.045 \pm 0.012$	$0.021 \pm 0.007$	$0.022 \pm 0.007$
SM+CI( $\Lambda_{LR}^{-14}$ )	$6.0 \pm 0.5$	$2.31 \pm 0.21$	$3.69 \pm 0.30$	$0.28 \pm 0.05$	$0.127 \pm 0.030$	$0.146 \pm 0.032$
SM+CI( $\Lambda_{LR}^{-20}$ )	$2.58 \pm 0.28$	$1.01 \pm 0.13$	$1.54 \pm 0.16$	$0.078 \pm 0.018$	$0.036 \pm 0.011$	$0.039 \pm 0.012$
SM+CI( $\Lambda_{RR}^{-14}$ )	$3.78 \pm 0.34$	$2.51 \pm 0.22$	$1.23 \pm 0.15$	$0.23 \pm 0.04$	$0.155 \pm 0.031$	$0.069 \pm 0.018$
SM+CI( $\Lambda_{RR}^{-20}$ )	$1.86 \pm 0.24$	$1.11 \pm 0.13$	$0.71 \pm 0.12$	$0.072 \pm 0.015$	$0.047 \pm 0.011$	$0.022 \pm 0.008$
SM+CI( $\Lambda_{LL}^{+14}$ )	$2.08 \pm 0.25$	$1.30 \pm 0.14$	$0.75 \pm 0.12$	$0.075 \pm 0.015$	$0.050 \pm 0.012$	$0.023 \pm 0.007$
SM+CI( $\Lambda_{LL}^{+20}$ )	$0.95 \pm 0.22$	$0.55 \pm 0.11$	$0.36 \pm 0.11$	$0.029 \pm 0.008$	$0.019 \pm 0.006$	$0.0073 \pm 0.0034$
SM+CI( $\Lambda_{LR}^{+14}$ )	$4.2 \pm 0.4$	$1.60 \pm 0.16$	$2.51 \pm 0.22$	$0.191 \pm 0.034$	$0.081 \pm 0.020$	$0.107 \pm 0.023$
SM+CI( $\Lambda_{LR}^{+20}$ )	$1.65 \pm 0.24$	$0.82 \pm 0.12$	$0.79 \pm 0.12$	$0.058 \pm 0.013$	$0.017 \pm 0.006$	$0.039 \pm 0.010$
SM+CI( $\Lambda_{RR}^{+14}$ )	$2.26 \pm 0.26$	$1.44 \pm 0.15$	$0.78 \pm 0.12$	$0.098 \pm 0.018$	$0.057 \pm 0.012$	$0.038 \pm 0.010$
SM+CI( $\Lambda_{RR}^{+20}$ )	$1.06 \pm 0.22$	$0.65 \pm 0.11$	$0.37 \pm 0.11$	$0.036 \pm 0.009$	$0.028 \pm 0.008$	$0.0044 \pm 0.0029$

Table 7.4: Comparison of background prediction to data with prediction of several CI signal models. Signal models are refereed to showing constructive or destructive interference (-/+ in superscript),  $\Lambda$  value (number in superscript) and formalism (letters in subscript). Binning used is the same as used for statistical analysis of CI model with the two high mass regions shown here. Total systematic error is included on each number. See section 8.1 for details of systematics.

Process	$1900 \leq m_{ee} \leq 4500 \text{ GeV}$
Drell-Yan	$0.435 \pm 0.002$
Top	$0.003 \pm 0.000$
Multi-Jet	$0.062 \pm 0.012$
Diboson	$0.053 \pm 0.004$
Photon-Induced	$0.058 \pm 0.001$
Total SM	$0.611 \pm 0.129$
Data	0
SM+ADD ( $M_S = 3.50 \text{ TeV}$ )	$21.637 \pm 2.144$
SM+ADD ( $M_S = 3.75 \text{ TeV}$ )	$13.171 \pm 1.295$
SM+ADD ( $M_S = 4.00 \text{ TeV}$ )	$8.436 \pm 0.821$
SM+ADD ( $M_S = 4.75 \text{ TeV}$ )	$2.952 \pm 0.282$

Table 7.5: Comparison of background prediction to data with prediction of several ADD signal models. One bin used the same in the statistical analysis of ADD. Total systematic error is included on each number. See section 8.1 for details of systematics.



---

## Chapter 8

### Statistical Analysis

The statistical analysis of results is done via a Bayesian approach where first a search for signs of new physics is done with a calculation of the significance of any excesses. Then in the absence of a signals exclusion limits on the scale of new physics (either  $\Lambda$  or  $M_S$ ) are then set. A slightly different search approach is made between CI and ADD. In CI the shape of new physics is studied and therefore a series of invariant mass search bins are used with bin edges of 400, 550, 800, 1200, 1800, 3000 and 4500 GeV. With the addition of information from the  $\cos\theta^*$  variable in this analysis bins are also then split up in  $\cos\theta^*$  as well as invariant mass. As seen in section 8.2.2 most of the new information is obtained via using two bins in  $\cos\theta^*$  making a total of 12 search bins distributed in invariant mass and  $\cos\theta^*$ . ADD on the other hand doesn't gain from the many search bin approach due to a sharper turn-on and undefined nature of the signal after the cut off point. Therefore only one search bin is used to search for ADD with a minimum invariant mass cut of 1900 GeV and upper cut of 4500 GeV. The lower range of this search bin is optimised by choosing the value with the highest expected limit. The ADD model gains no additional discriminating power from the  $\cos\theta^*$  variable. For each search bin a parametrisation of new physics is produced (discussed in section 7.2) as well as the background predicted and data observed. Also included is the background and signal parametrisation varied by each of the appropriate sources of systematic error (discussed in section 8.1) for signal and background. This all composes the input of the event selection in the statistical analysis.

The statistical analysis is carried out using the ROOT [57] package BAT or Bayesian Analysis Tool-kit [78]. This package allows for the integration over nuisance parameters

(discussed below) using the Markov Chain Monte Carlo method. The statistical analysis starts off with the definition of the number of expected events  $\mu$  found in the signal region as seen in equation 8.1.

$$\mu = n_s(\Theta, \bar{\Omega}) + n_b(\bar{\Omega}) \quad (8.1)$$

Here  $n_s$  is the number of signal events predicted by the model with a particular model parameter  $\Theta$  and  $n_b$  is the total number of predicted background events.  $\bar{\Omega}$  is then a set of Gaussian nuisance parameters or systematic uncertainties on the number of expected events for signal and background. A product of Poisson probabilities for each search bin  $k$  gives the Bayesian likelihood, seen in equation 8.2, of observing  $n$  events given the signal parameter  $\Theta$  and nuisance parameters  $\bar{\Omega}$ .

$$\mathcal{L}(n | \Theta, \bar{\Omega}) = \prod_{k=1}^N \frac{\mu_k^{n_k} e^{-\mu_k}}{n_k!} \quad (8.2)$$

where  $\mu_k^{n_k}$  and  $n_k$  are the total number of expected events and observed number of events in search bin  $k$  respectively.

$$\mathcal{P}(\Theta | n) = \frac{1}{\mathcal{Z}} \mathcal{L}_{\mathcal{M}}(n | \Theta) P(\Theta) \quad (8.3)$$

Equation 8.3 shows the posterior probability using Bayes' theorem for the observation of  $\Theta$  given  $n$ . Here  $\mathcal{Z}$  is the normalisation factor and  $\mathcal{L}_{\mathcal{M}}$  is the marginalised likelihood after all nuisance parameters have been integrated out. It is assumed all nuisance parameters are correlated across all search bins. A full description of nuisance parameters can be found in section 8.1. Finally  $P(\Theta)$  is the prior probability of  $\Theta$ . A 95% confidence level (CL) limit can then be found by finding  $\Lambda_{lim}$  that satisfies  $\int_0^{\theta_{lim}} P(\theta | \bar{n}) d\theta = 0.95$ . For CI  $P(\Theta)$  is chosen to be uniform and positive with respect to  $1/\Lambda^2$  or  $1/\Lambda^4$ . This form of priors is chosen due to the form of differential cross-section (equation 1.5) and its dependence on  $\Lambda$ . It is not obvious which prior is more correct as these forms refer to the interference and pure CI terms respectively which change in dominance throughout the search bins and model parameters, therefore the search is done using both parameters for completeness. A similar effect is seen in the form of the ADD differential cross-section (equation 1.7) and so there a prior of  $1/M_s^4$  or  $1/M_s^8$  are used for the same reason.

In order to check all signal formalisms 1000 background-like Pseudo-Experiments (PE) are run using BAT for each formalism. Each PE is then passed through the Bayesian statistical method above so they can be compared to data and signal predictions. Figure 8.1 shows posterior probability density functions (pdf's), for two CI formalisms, of these 1000 PE's.

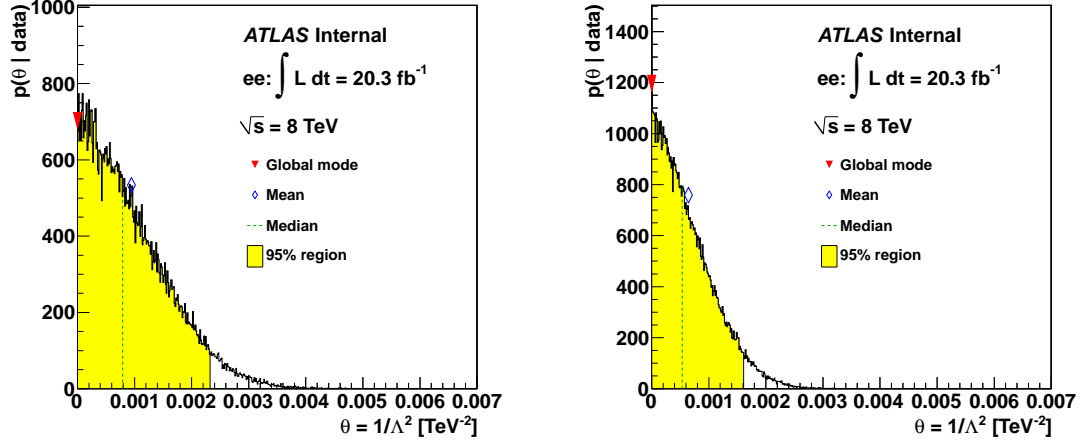


Figure 8.1: Posterior pdf distributions for the CI model formalisms LL and LR with constructive interference and a uniform positive prior in  $1/\Lambda^2$ .

## 8.1 Systematics

The list of nuisance parameters used for this statistical analysis make up a list of all systematic errors thought of as relevant for this analysis. Table 8.1 lists all the systematic errors used for this analysis along with their size while figures 7.2, 7.4 and 7.3 in the previous chapter show total background systematic errors in their ratio's. Due to this analysis using both the forward and backwards regions in the search all systematics needed to be assessed for both these regions separately. Following is a brief description of each of the systematics including how it was derived.

**Normalization** - This systematic accommodates the error associated with scaling MC samples within the Z peak to avoid luminosity errors however it also protects against any other sources of mass independent error. This systematic was investigated by looking at the effect of background cross-section on the scale factor.

**PDF Variation** - PDF variation was investigated as another source of systematic error using the set of 20 eigenvector error sets provided with the MSTW2008NNLO PDF [68]. These eigenvectors were organised into 4 groups, A, B, C and D, of eigenvectors with effects in similar regions of the invariant mass spectrum. These 4 groups were then used as separate nuisance parameters and applied to events based on dielectron invariant mass and  $\cos\theta^*$ .

**PDF Choice** - PDF choice refers to a comparison between the effects of different PDF's on the expected events from MC. Several other NNLO PDF are looked at including CT10 but the only PDF with predictions outside of the PDF variation systematic (seen above) is ABM11 [79] and so an additional systematic is introduced of the order of this difference.

**$\alpha_S$**  - A systematic is introduced to account for error in the value  $\alpha_S$ . It is varied between the values 0.11365 and 0.12044 according to the limits in MSTW. Recalculated cross-sections give a variation in the expected background and taken as the systematic.

**EW Corrections** - The EW correction is derived via the use of a different generator (MC-SANC [80]) when calculating the EW K-factor and differences between the method give the systematic.

**Photon-Induced** - The MC estimate for the PI fraction is predicted to be an upper estimate and so the effect of not including this background is studied and this effect on the event yield is taken as the systematic.

**Efficiency** - Systematic provided by the ATLAS electron photon performance group to accommodate the trigger and reconstruction efficiency corrections (see section 6.1.1).

**Scale/Resolution** - Systematic provided by the ATLAS electron photon performance group to accommodate the energy scale and energy resolution corrections (see section 6.1.1).

**Multijet/W+jets** - Systematic associated with the data driven multijet & W+jets estimate and seen in section 6.2.4.

**Beam Energy** - The beam energy uncertainty of the LHC 4 TeV beams is given as 0.65% giving this uncertainty which is again analysed to see its effect on event yield.

**Charge MisID** - Systematic associated with opposite sign requirement in the analysis. This error is estimated by injecting a higher fraction of charge miss-identification in to the DY MC sample and looking at the effect on background prediction. This is found to have an at most 3% effect at high mass.

**Statistical** - Systematic error of the statistical error of each of the MC samples used to es-

timate background and signal.

## 8.2 Angular Analysis Optimisation

This section looks at some of the issues revolving around the introduction of the angular search within  $\cos\theta^*$  as well as invariant mass. First a look at the effect of the loss in selection efficiency coming from the opposite sign requirement on the sensitivity of the search. Next is then a discussion on the optimisation of the binning used to search in  $\cos\theta^*$ .

### 8.2.1 Effect of the Opposite Sign Requirement on Analysis Reach

The opposite sign requirement is needed to ensure that calculations of the variable  $\cos\theta^*$  correctly use the particle instead of anti-particle. However the selection comes with a 7% drop in acceptance of signal in the signal search region (see table 5.1). The important question becomes what effect this has on the sensitivity of the analysis. This is important because angular dependence was introduced for a single CI formalism LR and not predicted to strongly impact the results for other formalisms. A study was done on the expected limits set by the Bayesian statistical analysis (see chapter 8) both with the opposite sign requirement introduced and without it for both a search in invariant mass only and search bins distributed in both invariant mass and  $\cos\theta^*$  (called the 1D and 2D search respectively below). Table 8.2 show limits for all of these possibilities for both the LL and LR formalisms. It is important to bear in mind this study was done before the analysis was finalised and so the limits do not represent the final results of the analysis but are consistent enough to represent the effects we are looking at. It can be seen that the introduction of the opposite sign requirement leads to a reduction in the reach of the limits while the introduction of the the 2D search bin approach greatly increases the the limits for the LR formalism while regaining the lost sensitivity in the case of the LL formalism. Although no difference is seen between the angular dependence of background and the LL formalism (see figures 7.4) the 2D search approach gains some extra shape information from the extra search bins used which offsets the loss of sensitivity from the opposite sign requirement. The same was found to be true for the ADD model as the LL formalism.

### 8.2.2 Optimisation of Search Bins in $\cos\theta^*$

The belief at the start of the analysis was that binning within  $\cos\theta^*$  would be optimised with two to  $n$  evenly distributed bins, varying bins in  $\cos\theta^*$  or even varying number of bins throughout invariant mass. This study was carried out at two different points; early on in the analysis when search bins were first discussed, then towards the end when the full analysis was almost finalized. The first study looked at expected limits for individual invariant mass bins while varying the number of  $\cos\theta^*$  bins. These “limits” do not give an accurate estimate of final limits but are used as a guide to see the sensitivity of each binning. The results from this study can be seen in table 8.3 where 600 PEs are run for each individual bin combination and expected limits are extracted from these. Random fluctuations in the limits are seen but are almost consistent through many of the binning structures. The highest limits found within each invariant mass bin can be seen as bold and a structure with more bins at low mass while less bins at high mass can be seen. However this structure does not gain a very big advantage over any other binning structures that could be chosen due to the small size of the differences. The study was postponed until systematics were finalised.

The second study seen in table 8.4 found very quickly that while changing from a 1D to a 2D search strategy using two evenly sized bins in  $\cos\theta^*$ , gave a moderate increase in limits, any further increase in the number of  $\cos\theta^*$  search bins gave no increase or a slight decrease in limits. This found that most of the extra information gained from searching in  $\cos\theta^*$  was seen in a split between forward ( $\cos\theta^* > 1$ ) and backwards ( $\cos\theta^* < 1$ ) regions. The cause of this effect comes from the introduction of systematics that grow at high mass as well as the increase in MC statistical error when binning the signal in finer bins. The two bin search structure was therefore chosen as optimal for searching in the  $\cos\theta^*$  variable meaning that with 6 invariant mass search bins 12 total search bins are used.

## 8.3 Signal Search & $p$ -Values

Consistency between data and background prediction is estimated by taking the likelihood of signal given  $n$  observed events (observed) and comparing this to the likelihood of signal given the outcome of a set of 1000 PE (expected given no signal) calculated above. A likeli-

hood ratio is then calculated between the signal prediction and background only hypothesis where the signal predictions likelihood is maximised to the highest likelihood in  $\Theta$ . This is done for both the observed likelihood and the set of 1000 PE likelihoods for the expected result given no signal. These are converted to the distribution of negative Log Likelihood Ratio's (LLR) given in figure 8.2 comparing observed values to the expected values in the distribution of PE's. More of these distributions are found in appendix C.  $p$ -value's are also derived for each formalism quantifying the probability of observing a fluctuation in PE's at least as signal-like as is observed in data. A table of  $p$ -values for each formalism for CI can be found in table 8.5 and for ADD in table 8.6.

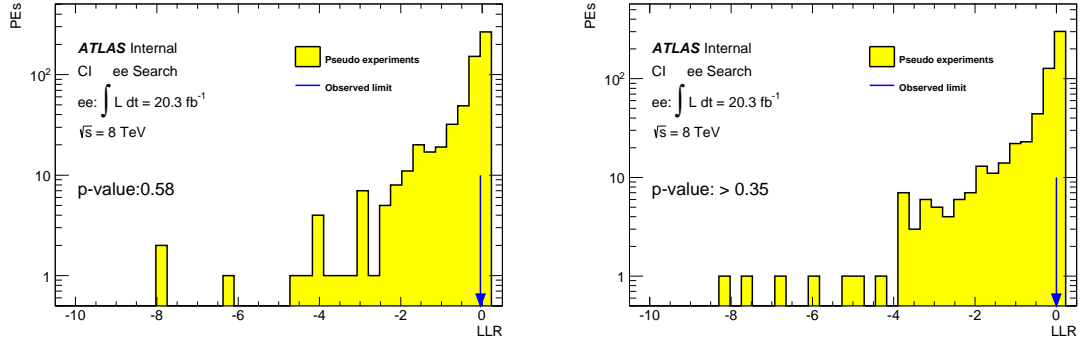


Figure 8.2: Distribution of negative Log Likelihood Ratio's for the CI formalisms LL (left) and LR (right) with constructive interference given a uniform positive prior in  $1/\Lambda^2$ .

## 8.4 Setting Limits

With no sign of new physics found limits are set on the lower limit of the scale of new physics for each CI and ADD formalism. Limits in  $\Theta$  are extracted from each of the 1000 PE's for each formalism and the mean of this distribution is taken as the expected limit and converted into a limit on  $\Lambda$  for CI and  $M_s$  for ADD. Figure 8.3 shows the distribution of these PE's in  $\Theta$  along with the mean value of the distribution taken as the expected limit. More of these distributions are found in appendix C. Tables 8.7 and 8.8 then show the expected limits converted into  $\Lambda$  and  $M_s$  respectively where the same procedure had been done in the ADD channel. The final observed limits are also included in these figures and tables compared to the expected limits and extracted from the observed data. The limits in

the ADD search are also converted from the GRW formalism to all of the other formalism discussed in section 1.2.2 by a rearrangement of equation 1.8. The exception is the HLZ  $n = 2$  formalism which has its own MC sample and limits are set in the same way as for GRW. The limits on all other formalisms discussed are then seen in 8.9.

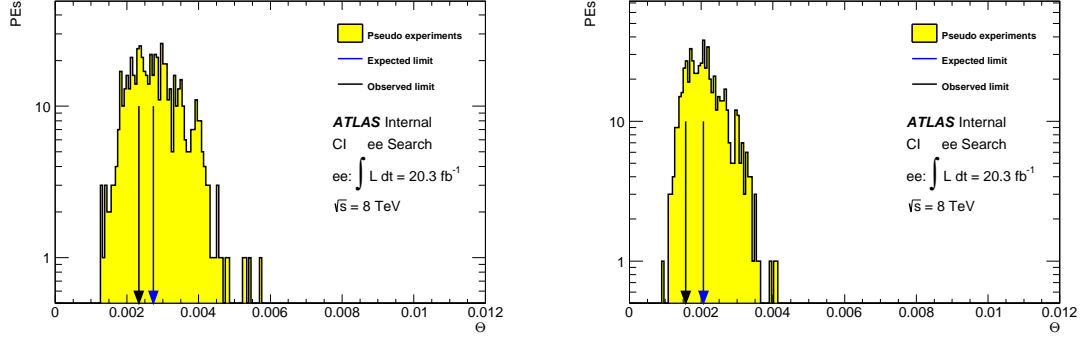


Figure 8.3: Distribution of PE's with associated limits for CI formalisms LL (left) and LR (right) with constructive interference given a uniform positive prior in  $1/\Lambda^2$ . The mean value is shown as the expected limit for comparison to the observed limit shown.  $\Theta = 1/\Lambda^2$

## 8.5 Combination with the Muon Search

A similar analysis was carried out at the same time as this one looking at the dimuon decay channel instead. This analysis followed the same procedure and after failing to find any signals limits were set on the scale of new physics. Assuming lepton universality integrated luminosity can effectively be doubled by combining the results from both channels. Therefore the posterior pdf's from each analysis were combined in BAT and new limits set on the scale of new physics. Care was taken to correctly treat sources of systematic uncertainty that are correlated between analyses. Combined limits of this form can be found in tables 8.10 and 8.11 for the CI and ADD models respectively while table 8.12 shows the combined limits for the other ADD formalisms. These limits mark the highest limits set for this analysis owing to the higher effective luminosity.



Source	Signal Systematic [%]	
	Forward	Backward
Normalization	4.0 (4.0) [4.0]	4.0 (4.0) [4.0]
PDF Variation	< 0.1 (0.2) [0.5]	< 0.1 (0.2) [0.5]
PDF Choice	NA	NA
$\alpha_s$	NA	NA
EW Corrections	< 0.1 (< 0.1) [0.1]	< 0.1 (< 0.1) [0.1]
Photon-Induced	NA	NA
Efficiency	1.0 (2.0) [3.0]	1.0 (2.0) [3.0]
Scale/Resolution	1.2 (2.4) [5.0]	1.2 (2.4) [5.0]
Multijet/W+jets	NA	NA
Beam Energy	1.0 (3.0) [5.0]	1.0 (3.0) [5.0]
Charge MisID	1.2 (2.0) [2.9]	1.2 (2.0) [2.9]
Statistical	3.0 (3.0) [3.0]	3.0 (3.0) [3.0]
Total	5.5 (6.9) [9.6]	5.5 (6.9) [9.6]

Source	Background Systematic [%]	
	Forward	Backward
Normalization	4.0 (4.0) [4.0]	4.0 (4.0) [4.0]
PDF Variation	6.0 (12.5) [35.0]	10.0 (28.0) [62.5]
PDF Choice	1.0 (7.0) [22.0]	1.0 (7.0) [22.0]
$\alpha_s$	1.0 (3.0) [5.0]	1.0 (3.0) [5.0]
EW Corrections	1.0 (2.0) [4.0]	1.0 (2.0) [4.0]
Photon-Induced	6.0 (10.0) [17.0]	9.5 (16.5) [29.0]
Efficiency	1.0 (2.0) [3.0]	1.0 (2.0) [3.0]
Scale/Resolution	1.2 (2.4) [5.0]	1.2 (2.4) [5.0]
Multijet/W+jets	3.0 (5.0) [21.0]	3.0 (5.0) [21.0]
Beam Energy	1.0 (3.0) [5.0]	1.0 (3.0) [5.0]
Charge MisID	1.2 (2.0) [2.9]	1.2 (2.0) [2.9]
Statistical	0.5 (0.5) [0.5]	0.5 (0.5) [0.5]
Total	10.3 (19.6) [50.6]	14.9 (34.4) [76.1]

Table 8.1: All sources of systematic error and their approximate size as a percentage (%) for dielectron mass of 1 TeV (2 TeV) [3 TeV].

Search strategy	LL	LR
1D approach no opposite sign requirement	19.27	21.64
1D approach with opposite sign requirement	18.86	21.17
2D approach with opposite sign requirement	19.40	22.31

Table 8.2: Expected Limits calculated with 600 PE's for the LL and LR constructive CI formalisms looking at the effect of the opposite sign requirement on limits and introduction of 2D limits.

<b>Constructive Interference</b>	Mass bins [GeV]					
$\cos\theta^*$ binning	400-550	550-800	800-1200	1200-1800	1800-3000	3000-4500
1 bin	13.7154	15.0867	17.2645	17.4408	16.8898	8.81322
2 even bins	14.0608	15.9546	18.0246	17.9244	<b>17.4196</b>	<b>8.82076</b>
4 even bins	14.0553	15.9607	18.1429	18.1086	17.2942	8.74857
3 even bins	<b>14.1691</b>	15.7593	18.0305	<b>18.1593</b>	16.9797	8.8057
4 bins A	14.0999	<b>16.053</b>	18.1057	18.1086	17.1486	8.82008
4 bins B	<b>14.1655</b>	16.0005	<b>18.3324</b>	18.1146	17.3696	8.81391
5 even bins	13.7568	15.8124	18.2437	18.1414	17.0067	8.7914
<b>Destructive Interference</b>	Mass bins [GeV]					
$\cos\theta^*$ binning	400-550	550-800	800-1200	1200-1800	1800-3000	3000-4500
1 bin	8.31287	8.98298	12.5147	14.7194	15.3456	<b>8.52415</b>
2 even bins	8.87217	9.22688	12.7154	15.0151	<b>15.8282</b>	8.5155
4 even bins	8.77311	9.38027	12.7906	<b>15.0944</b>	15.6893	8.49673
3 even bins	8.94302	9.30384	12.7526	15.0372	15.4184	8.51457
4 bins A	8.98625	9.28697	12.7833	<b>15.0953</b>	15.5823	8.4854
4 bins B	8.93035	9.50594	<b>12.8105</b>	15.0585	15.773	8.42107
5 even bins	<b>9.22944</b>	<b>9.59655</b>	12.7666	15.0764	15.7632	8.44356

Table 8.3: Expected Limits calculated with 600 PE's for individual mass bins while varying  $\cos\theta^*$  binning to select variable search bins. The highest limits found for each invariant mass bin are shown in **bold**. No systematics were included in this study. Even bins refer to bins distributed evening in  $\cos\theta^*$  while A and B refer to larger bins in the centre of the  $\cos\theta^*$  distribution and larger bins at the extremes in  $\cos\theta^*$  respectively while still being symmetric around  $\cos\theta^* = 0$ .

$\cos\theta^*$ bins	Constructive	Destructive
1 bin	21.1691	17.0884
2 bin	22.3078	17.6309
4 bin	22.1839	17.5169

Table 8.4: Expected Limits on the LR formalism calculated with 600 PE's showing the effect of changing from 1 to 2 to 4 search bins in  $\cos\theta^*$ .

$p$ -value [%]	$1/\Lambda^2$		$1/\Lambda^4$	
	Constructive	Destructive	Constructive	Destructive
LL: ee	58	60	> 76	> 58
LR: ee	> 35	36	> 85	> 62
RR: ee	> 35	68	> 75	> 62

Table 8.5:  $p$ -values for all CI formalisms and prior's.

$p$ -value [%]	$1/M_S^4$	$1/M_S^8$
GRW: ee	51	> 58

Table 8.6:  $p$ -values for ADD with each prior.

Limits [TeV]	$1/\Lambda^2$		$1/\Lambda^4$	
	Constructive	Destructive	Constructive	Destructive
Expected LL: $ee$	19.11	14.02	17.44	13.02
Observed LL: $ee$	20.71	16.35	18.58	14.72
Expected LR: $ee$	22.01	17.37	20.09	16.26
Observed LR: $ee$	25.16	19.19	22.19	17.68
Expected RR: $ee$	18.97	14.23	17.23	13.14
Observed RR: $ee$	20.22	16.57	18.34	14.89

Table 8.7: Expected and observed 95% C.L. lower limits for all CI formalisms and prior's.

GRW ADD Limits [TeV]	$1/M_S^4$	$1/M_S^8$
Expected: $ee$	4.79	4.50
Observed: $ee$	4.79	4.50

Table 8.8: Expected and observed 95% C.L. lower limits for ADD with each prior.

Expected and Observed Limit on $M_S$ [TeV]									
Channel	Prior	GRW	Hewett	HLZ					
				n=2	n=3	n=4	n=5	n=6	n=7
Expected: $ee$	$1/M_S^4$	4.79	4.28	4.85	5.70	4.79	4.33	4.03	3.81
Observed: $ee$		4.79	4.28	4.86	5.70	4.79	4.33	4.03	3.81
Expected: $ee$	$1/M_S^8$	4.50	4.25	4.42	4.90	4.50	4.27	4.12	4.01
Observed: $ee$		4.50	4.25	4.42	4.90	4.50	4.27	4.12	4.01

Table 8.9: Expected and observed 95% C.L. lower limits on  $M_S$ , for ADD signal in the GRW, Hewett and HLZ formalisms.

Limits [TeV]	$1/\Lambda^2$		$1/\Lambda^4$	
	Constructive	Destructive	Constructive	Destructive
Expected LL: $\ell\ell$	21.44	19.11	14.73	13.81
Observed LL: $\ell\ell$	21.55	19.61	17.15	15.35
Expected LR: $\ell\ell$	24.78	23.12	18.46	17.57
Observed LR: $\ell\ell$	26.25	23.77	18.95	17.79
Expected RR: $\ell\ell$	20.98	19.11	14.99	14.21
Observed RR: $\ell\ell$	21.11	19.31	17.50	15.58

Table 8.10: Combined expected and observed 95% C.L. lower limits for the 2D LL, LR, and RR Contact Interaction search using a uniform positive prior.

GRW ADD Limits [TeV]	$1/M_S^4$	$1/M_S^8$
Expected: $\ell\ell$	4.83	4.60
Observed: $\ell\ell$	5.12	4.79

Table 8.11: Combined expected and observed 95% C.L. lower limits for the ADD search using a uniform positive prior.

Expected and Observed Limit on $M_S$ [TeV]									
Channel	Prior	GRW	Hewett	HLZ					
				n= 2	n=3	n=4	n=5	n=6	n=7
Expected: $ll$	$1/M_S^4$	4.83	4.31	5.09	5.74	4.83	4.36	4.06	3.84
Observed: $ll$		5.12	4.57	5.47	6.09	5.12	4.62	4.30	4.07
Expected: $ll$	$1/M_S^8$	4.60	4.35	4.67	5.01	4.50	4.37	4.22	4.10
Observed: $ll$		4.79	4.53	4.94	5.23	4.79	4.56	4.40	4.27

Table 8.12: Expected and observed combined 95% C.L. lower limits on  $M_S$ , for ADD signal in the GRW, Hewett and HLZ formalisms.

---

## Chapter 9

# Non-Resonant 7 TeV Analysis

This chapter looks at the non-resonant analysis done within ATLAS on 2011 data and was a measurement made prior to the other analysis presented in this thesis. The author made a major contribution to this analysis working on the dielectron search channel and following it to publication [1]. The 7 TeV analysis major differences come from not including the angular search in  $\cos\theta^*$  and looking at only the LL CI formalism and GRW ADD formalism. Background simulation differs slightly with different generators used and the explicit change from the QCD and W+jets background to the more inclusive multijets & and W+jets obtained fully via a data driven method. The event selection also differs between the two analyses with the optimisation of the isolation selection and updated shower shape selection in the 8 TeV analysis. The big change is the addition of the angular analysis with respect to  $\cos\theta^*$  introducing the opposite sign requirement and changing the search bins used in the Bayesian analysis. A slightly smaller list of systematic errors were included in this analysis compared to the 8 TeV one. Below is an overview of each part of this analysis with comparisons between this and the main analysis spoken of in this thesis.

### 9.1 Data and Background Processes

#### Data

All data used in this analysis is taken from the LHC 2011  $\sqrt{s} = 7$  TeV proton-proton collision data of which ATLAS recorded  $4.9fb^{-1}$  of electron candidate data. Data was collected

with stable LHC beams and a fully operational inner detector and calorimeter each being important in the identification of good electron candidates.

## Background

The background process are the same between analyses with slight differences in the MC generators used. The bigger difference however are the comparisons between the W+jets and QCD backgrounds used in this analysis with the multijet & W+jets background used in the 8 TeV analysis. This difference is mainly naming differences but here the background is produced through a combination of a MC sample and a data driven method while the 8 TeV analysis uses only a data driven method.

Standard Model Drell-Yan was simulated by the leading-order (LO) PYTHIA 6 [81] Monte Carlo (MC) event generator. This method was used to generate a  $Z \rightarrow ee$  sample for the low dielectron invariant mass region ( $m_{ee} < 120$  GeV) and a  $DY \rightarrow ee$  mass binned sample for the high invariant mass ( $m_{ee} > 120$  GeV) to keep high statistics. Similarly to the 8 TeV analysis K-factors are used here to weight from the LO prediction up a NNLO prediction. Four other samples are included to produce the background estimate, these are:  $t\bar{t}$ , produced with MC@NLO [73]; diboson, WW, WZ and ZZ decays produced with HERWIG [70]; W+jets, produced with ALPGEN [82], JIMMY [74] and HERWIG [70]; and QCD, produced using a data driven method.

## Signal

Five benchmarks for the value of  $\Lambda$  where chosen for the CI signal samples for both constructive and destructive interference. Like the DY these were also produced with LO PYTHIA 6 [81] containing both the pure DY contribution as well as the interference and pure CI components. Samples where produced above dilepton invariant mass of 120 GeV to increase statistics above the Z boson peak where new physics would appear.

ADD samples were generated using SHERPA [77] at leading order with 4 values of  $M_s$  produced. Samples were again produced above dilepton invariant mass of 120 GeV.

Corrections are applied to all MC samples. A correction handling event pile-up is applied on an event by event basis as well as QCD and Electroweak K-factor corrections

applied as a function of invariant mass to the signal samples and SM DY samples. The K-factors applied to DY scales the original LO predictions using the MRST2007LO\*\* [69] PDF to the MSTW2008NNLO [68] PDF. These corrections did not change in method between the 7 and 8 TeV analyses and are discussed in more detail in section 6.1.1.

## 9.2 Electron Identification and Selection

The selection of electron candidates for the CI and ADD analysis can be split into three main parts, selection of a good event, selection of a set of good electrons and selection of a good dielectron pair.

### Event Selection

- Each event is required to contain at least one reconstructed primary vertex with more than 2 charged tracks traceable to it.
- Event is required have passed the chosen unprescaled electron trigger (EF\_g20\_loose).

### Electron Selection

- Each electron is required to have a transverse momentum ( $p_T$ ) greater than 25 GeV.
- Electron  $|\eta| < 2.47$  and not lie within the detector crack region  $1.37 \leq |\eta| \leq 1.52$  due to a decreased energy resolution.
- Electrons are required to pass identification criteria on the transverse shower shape, the longitudinal leakage into the hadronic calorimeter, and the association to an inner detector track, defined together as a “medium” electron identification.
- If expected electron is required to have signal in the inner most level of the tracking detector (B-layer). Used to suppress background from photon conversions.

### Dielectron Selection

- Selection of two highest  $p_T$  electrons left in event.

- Isolation (A cone around the candidate in the calorimeter is required to have  $< 7$  GeV deposited in it) of the highest  $p_T$  electron in the event is required to suppress QCD jet background.
- Dielectron invariant mass ( $m_{ee}$ ) is required to be greater than or equal 70 GeV.

There are several differences between the 7 and 8 TeV event selections. The trigger used is different in each case as the lowest threshold unprescaled trigger that is available is used for each data set. Transverse momentum requirements have then changed in accordance with the thresholds of the triggers as well as the increase in the invariant mass requirement for the same reason. The identification of a “medium” electron was updated between the two analyses with the 8 TeV version also including the expected signal in the tracking detector B-layer as a requirement. The isolation requirement underwent an optimisation between the two analyses detailed in section 5.2. The final difference is the lack of opposite sign requirement in this analysis.

These remaining candidates are then the results. The signal region is defined as  $m_{ee} > 200$  GeV while the  $70 \leq m_{ee} \leq 200$  GeV region is used as a control region.

$m_{ee}$ [GeV]	70-110	110-200	200-400
DY	$1231053.7 \pm 1109.5$	$26756.7 \pm 163.6$	$2964.0 \pm 54.4$
$t\bar{t}$	$879.6 \pm 29.7$	$1008.8 \pm 31.8$	$315.8 \pm 17.8$
Dibosons	$1827.1 \pm 42.7$	$415.4 \pm 20.4$	$146.6 \pm 12.1$
QCD + W+jets	$2885.7 \pm 53.7$	$1892.0 \pm 43.5$	$510.5 \pm 22.6$
Total	$1236646.0 \pm 1112.0$	$30072.9 \pm 173.4$	$3936.9 \pm 62.7$
Data	1236646	29816	4026

400-800	800-1200	1200-3000
$266.0 \pm 16.3$	$12.2 \pm 3.5$	$1.5 \pm 1.2$
$20.5 \pm 4.5$	$0.3 \pm 0.6$	$0.0 \pm 0.2$
$16.5 \pm 4.1$	$0.9 \pm 0.9$	$0.1 \pm 0.3$
$49.5 \pm 7.0$	$2.0 \pm 1.4$	$0.3 \pm 0.5$
$352.4 \pm 18.8$	$15.4 \pm 3.9$	$1.9 \pm 1.4$
358	17	3

Table 9.1: Data yield compared to background MC scaled to luminosity of data. Errors shown are statistical only.



### 9.2.1 Data and Background Comparison

Table 9.1 shows the number of data events remaining after selection of dielectron candidates compared to the total background prediction with all individual background components also shown. The simulated MC samples also undergo a scaling factor to scale within the Z boson peak. This scale factor works the same as in the 8 TeV analysis only within the slightly more limited range  $70 \leq m_{ee} \leq 110$  GeV. As can be seen the background prediction matches very closely to data within the statistical errors shown.

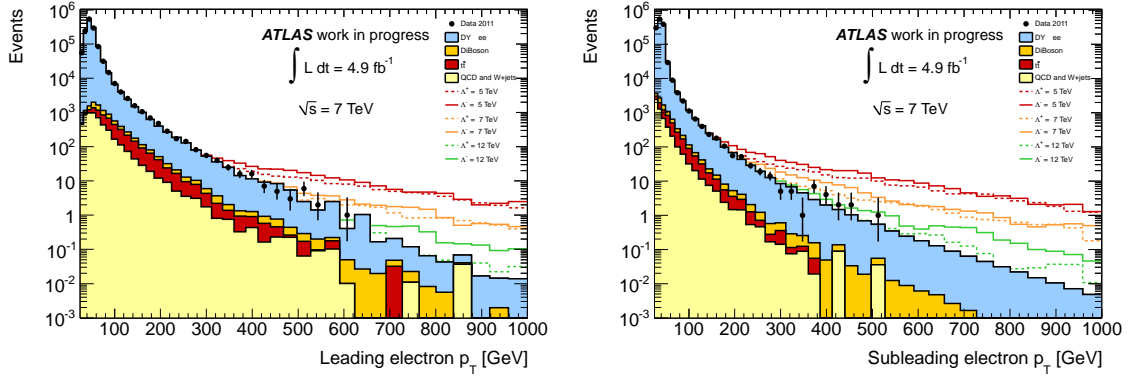


Figure 9.1:  $p_T$  distribution of the leading (left) and subleading (right) electrons showing data, MC background and example CI signal samples compared to data.

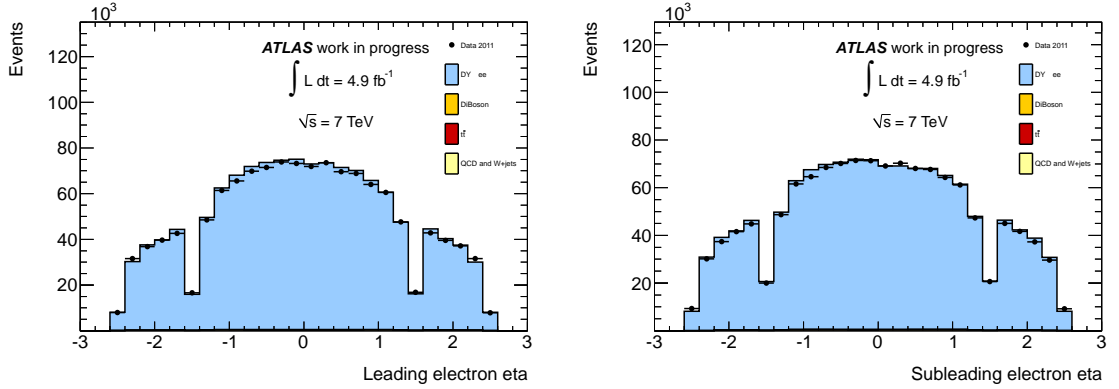


Figure 9.2:  $\eta$  distribution of the leading (left) and subleading (right) electrons showing data, MC background compared to data.

Control plots were produced to display that the distributions were behaving as predicted such as the  $p_T$  (Fig. 9.1) and the  $\eta$  (Fig. 9.2) distributions.

$m_{ee}$ [GeV]	110-200	200-400	400-800	800-1200	1200-3000
$\Lambda^- = 3$ TeV	$18790.8 \pm 137.1$	$5022.4 \pm 70.9$	$2766.3 \pm 52.6$	$1089.2 \pm 33.0$	$673.3 \pm 25.9$
$\Lambda^- = 4$ TeV	$18212.5 \pm 135.0$	$3707.1 \pm 60.9$	$1102.5 \pm 33.2$	$356.9 \pm 18.9$	$214.3 \pm 14.6$
$\Lambda^- = 5$ TeV	$17821.5 \pm 133.5$	$3310.5 \pm 57.5$	$653.1 \pm 25.6$	$160.6 \pm 12.7$	$97.7 \pm 9.9$
$\Lambda^- = 7$ TeV	$17711.1 \pm 133.1$	$3018.8 \pm 54.9$	$385.0 \pm 19.6$	$56.1 \pm 7.5$	$26.5 \pm 5.1$
$\Lambda^- = 12$ TeV	$17693.4 \pm 133.0$	$2992.7 \pm 54.7$	$296.5 \pm 17.2$	$20.4 \pm 4.5$	$5.6 \pm 2.4$
$\Lambda^+ = 3$ TeV	$18106.6 \pm 134.6$	$4063.8 \pm 63.7$	$2103.3 \pm 45.9$	$918.1 \pm 30.3$	$621.4 \pm 24.9$
$\Lambda^+ = 4$ TeV	$17958.1 \pm 134.0$	$3178.6 \pm 56.4$	$765.6 \pm 27.7$	$288.0 \pm 17.0$	$194.9 \pm 14.0$
$\Lambda^+ = 5$ TeV	$18026.6 \pm 134.3$	$2895.6 \pm 53.8$	$432.1 \pm 20.8$	$111.4 \pm 10.6$	$78.8 \pm 8.9$
$\Lambda^+ = 7$ TeV	$17926.4 \pm 133.9$	$2857.5 \pm 53.5$	$278.2 \pm 16.7$	$34.3 \pm 5.9$	$19.1 \pm 4.4$

Table 9.2: CI signal yields for  $4.9 \text{ fb}^{-1}$ .

$m_{ee}$ [GeV]	$\geq 1300$
$M_S = 1500$ GeV (GRW)	$94.8 \pm 9.7$
$M_S = 2000$ GeV (GRW)	$42.7 \pm 6.5$
$M_S = 2500$ GeV (GRW)	$11.3 \pm 3.4$
$M_S = 3000$ GeV (GRW)	$3.2 \pm 1.8$

Table 9.3: ADD analysis region yields for  $4.9 \text{ fb}^{-1}$ .

### 9.2.2 New Physics Signal Expectation

Tables 9.2 and 9.3 show the yield from the CI and ADD MC signals used after scaling to data luminosity. The ADD yield is only shown in a single bin above 1300 GeV as the ADD statistical analysis uses only a one bin approach to set a limit of a general increase over SM background. Table 9.4 shows the same one bin approach to the data MC comparison table.

$m_{ee}$ [GeV]	$\geq 1300$
DY	$1.1 \pm 1.1$
$t\bar{t}$	$0.0 \pm 0.1$
Dibosons	$0.1 \pm 0.3$
QCD + W+jets	$0.2 \pm 0.4$
Total	$1.4 \pm 1.2$
Data	2.0

Table 9.4: Data and MC yields for ADD analysis region.

Figures 9.3 (9.5) show the dielectron invariant mass distribution comparing data to

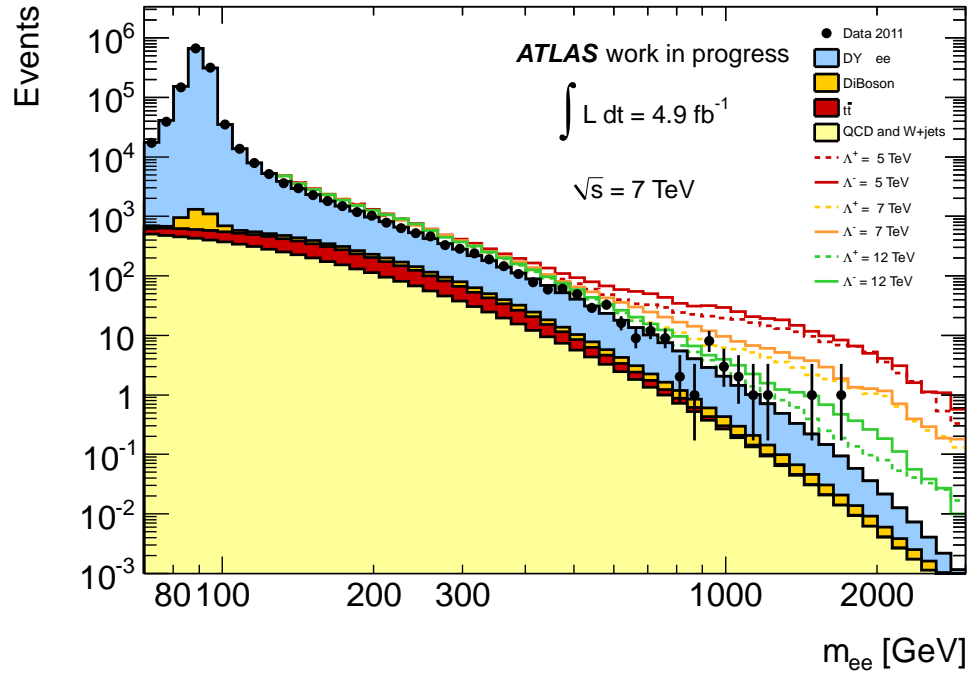


Figure 9.3: Dielectron invariant mass distribution for data and Monte Carlo simulation. Lines show expected distributions for the presence of Contact Interactions.

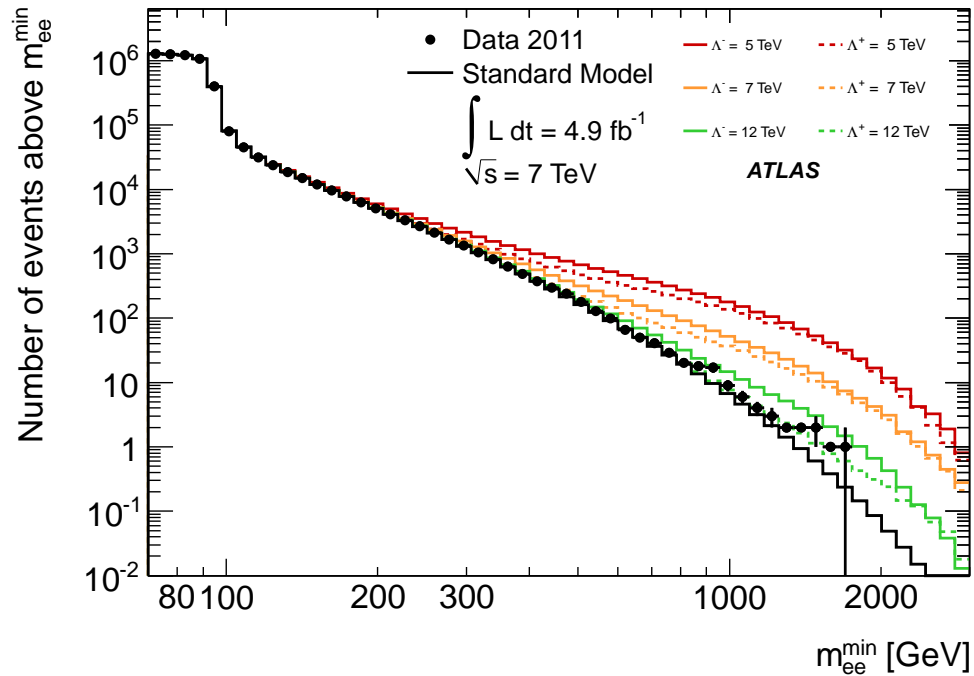


Figure 9.4: Dielectron integrated invariant mass distribution for data and total background Monte Carlo simulation. Lines show expected distributions for the presence of Contact Interactions.

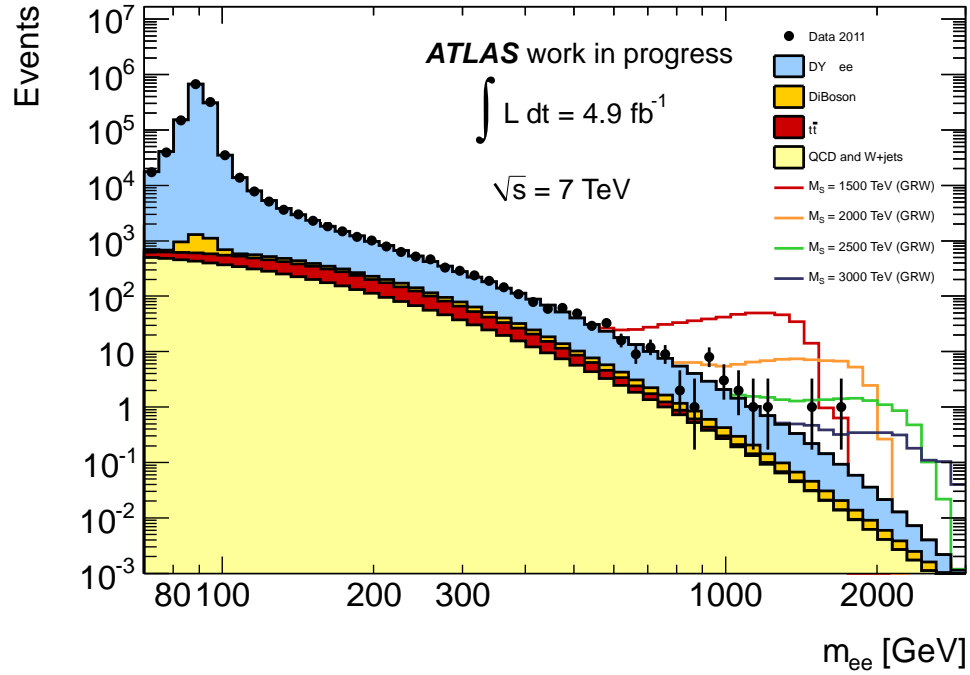


Figure 9.5: Dielectron invariant mass distribution for data and Monte Carlo simulation. Lines show expected distributions for the presence of ADD.

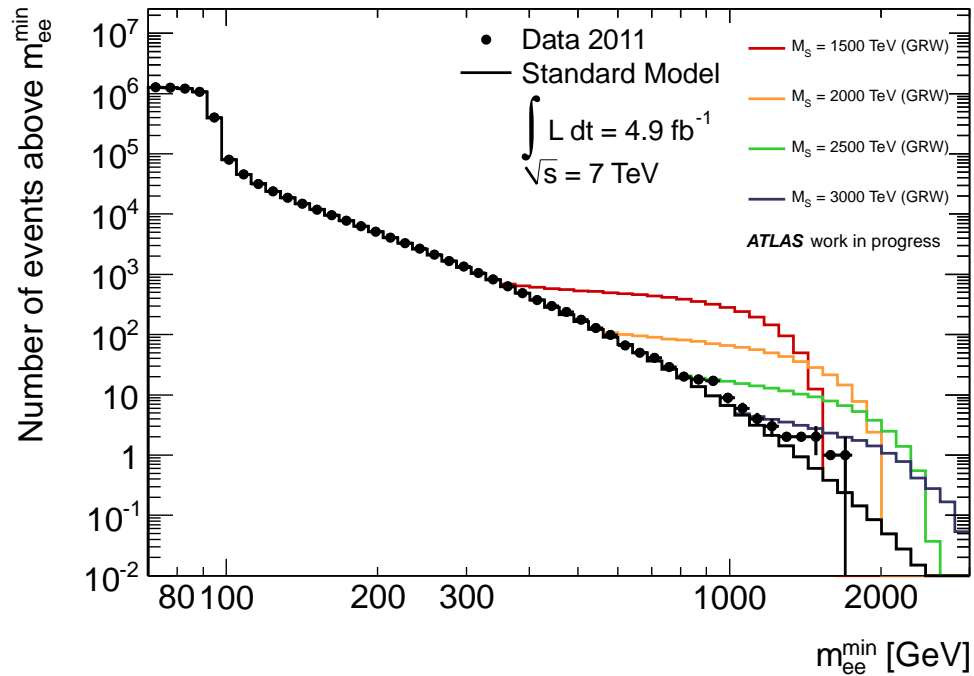


Figure 9.6: Dielectron integrated invariant mass distribution for data and total backpicking Monte Carlo simulation. Lines show expected distributions for the presence of ADD.

background MC while showing the effect CI (ADD) would have on this spectrum. Figures 9.4 (9.6) then show the same spectrum but with an integrated invariant mass distribution instead which indicates better general increases in the dielectron spectrum. These integrated invariant mass distributions show that although no excess is seen a slight difference exist between data and background prediction. This difference leads to a decrease in the observed limits compared to the expected limits as seen in section 9.3.

### 9.3 Statistical Analysis

No evidence of new physics was seen in this analysis and the same procedure was carried out here as discussed in chapter 8 to obtain limits on the minimum scale of new physics. This search differs as only dielectron invariant mass is used as a search variable and search bins are found at a lower invariant mass due to the lower energy and statistics of this analysis. The CI search is carried out in 5 search bins with bin edges of 110, 200, 400, 800, 1200, 3000 GeV while the ADD search was carried out in a single bin above 1300 GeV which is optimised by selecting the bin providing the highest expected limit. As in the 8 TeV analysis the expected number of events from signal was parametrised as a function of  $1/\Lambda^2$  and  $1/\Lambda^4$  for CI and  $1/M_s^4$  and  $1/M_s^8$  for ADD. Table 9.5 shows the list of systematics considered at nuisance variables for this statistical analysis. The PDFs/ $\alpha_s$  and Weak k-factor systematics are analogous to the PDF variation systematic from the 8 TeV analysis while all others mentioned are the same.

Source	Signal	Background
Normalization	5.0% (5.0%)	NA
PDFs/ $\alpha_s$	NA	7.0% (20.0%)
Weak k-factor	NA	2.3% (4.5%)
Efficiency	1.0% (2.0%)	1.0% (2.0%)
Scale/Resolution	1.2% (2.4%)	1.2% (2.4%)
QCD/W+jets background	NA	12.0% (26.0%)
Total	5.0% (6.0%)	14.0% (33.0%)

Table 9.5: All sources of systematic error and their approximate size for dielectron mass of 1 TeV (2 TeV).

As no evidence of new physics was found then a Bayesian statistical analysis was used to set a limit on  $\Lambda$  and  $M_s$ . These limits can be seen in table 9.6. Expected limits were

obtained by running 1000 PE's and the mean limit taken with respect to  $\Lambda$  and  $M_s$  for CI and ADD. Combined limits were also calculated with the dimuon search channel giving the highest limits on the scale of new physics for both CI and ADD at the time the paper was released. The Limits obtained in the 7 TeV analysis constituted the highest limits on either model when obtained the 8 TeV results then replace them within more formalisms. Improvements can also be seen in the upgrades to the analysis procedure between the two making the 8 TeV analysis a more mature analysis.

Channel	ee	ee+ $\mu\mu$
Expected CI constructive	13.73 TeV	15.10 TeV
Expected CI destructive	10.41 TeV	11.42 TeV
Observed CI constructive	11.60 TeV	12.70 TeV
Observed CI destructive	8.76 TeV	9.63 TeV
Expected ADD	2.84 TeV	2.94 TeV
Observed ADD	2.71 TeV	2.94 TeV

Table 9.6: 95% confidence level limits found in the CI and ADD analyses.

---

# Chapter 10

## Conclusion

To conclude this analysis sees no evidence of new non-resonant physics at high mass in the dielectron decay channel and along with the dimuon decay channel. Limits are set using a Bayesian statistical approach on the scale of new physics in the dilepton decay channel for two models of non-resonant new physics, CI and ADD. The limits set mark the highest limits found for  $qq\ell\ell$  contact interactions with limits set on three formalisms of LL, LR and RR Contact Interactions. While the ADD limits mark a large increase in the previous dilepton searches at the LHC.

Comparing to the previous CI ATLAS analysis [1], detailed in chapter 9, where limits of  $\Lambda > 12.7$  TeV and  $\Lambda > 9.63$  TeV for the dilepton LL CI model for constructive and destructive interference were set, limits established using the 8 TeV data of  $\Lambda > 21.55$  TeV and  $\Lambda > 19.61$  TeV for the dilepton LL CI model for constructive and destructive interference mark a significant increase in these results. Higher limits were also set for new LR formalism where limits of  $\Lambda > 26.25$  TeV and  $\Lambda > 23.77$  TeV for constructive and destructive interference were obtained which was made possible by the additional information coming from the new angular analysis used. As expected similar limits were set for the RR formalism as for the LL formalism due to the symmetry of these interactions. Observed limits within the electron channel were found to vary up slightly from the expected value due to a slight deficit of observed events in the 1200-1800 GeV search bin for forward and backwards. This deficit was found to not be significant and figure 8.3 shows the observed limits to be in agreement with the distribution of expected limits from pseudo experiments.

CMS have not yet released limits on contact interactions for the 8 TeV data set to com-

pare to.

ADD limits also saw a significant increase from the previous analysis [1] with combined dilepton limits for the GRW formalism at  $M_s > 4.79$  TeV compared to the previous limits of  $M_s > 2.94$  TeV set on 2011 data. Limits were also converted in to many different formalisms seen in table 8.9.

For completeness all limits are also calculated for two separate priors in Bayesian statistical analysis motivated by the form of the differential cross-section of new physics for both CI and ADD.

## 10.1 Looking Forward

Beyond this analysis ATLAS looks towards RunII due to start in 2015. With no new physics discovered beyond the Standard Model so far the next few years will be important for searches such as this. An increase in centre of mass energy to 13 and then to 14 TeV gains further increases in the reach of limits but after just over a year of running at the proposed centre of mass energy a final limit for the LHC will be reached. The final limit is because centre of mass energy is far more important in the sensitivity of the non resonant search than statistics obtained from a higher luminosity of data. If new physics such as proposed here is not found within a few years of running then it will be ruled out in this form from the reach of the LHC. Non-resonant physics as well a resonant decays, particularly in the clean dilepton channel, will be some of the first physics to be ruled out or found at a new collision energy but this doesn't mean there are not other beyond the SM process that could yet exist in nature. The SM has been shown to make very accurate predictions for a host of phenomena yet we know it is not a complete theory. If it holds up within the energy range of the LHC is yet to be seen.



---

# Appendices

---

# Appendix A

## Extra Results & Control Plots

This appendix contains additional plots of the data background comparison. Figure A.1 shows the same  $A_{FB}$  distribution as in the main text but with a different example signal overlaid. Figures A.2 and A.3 show the  $p_T$  and  $\eta$  distributions for the highest and second highest  $p_T$  electrons with comparison between background and data. While figures A.4, A.5, A.6, A.7 and A.8 show the comparison within the  $\cos\theta^*$  variable for each of the search bins.

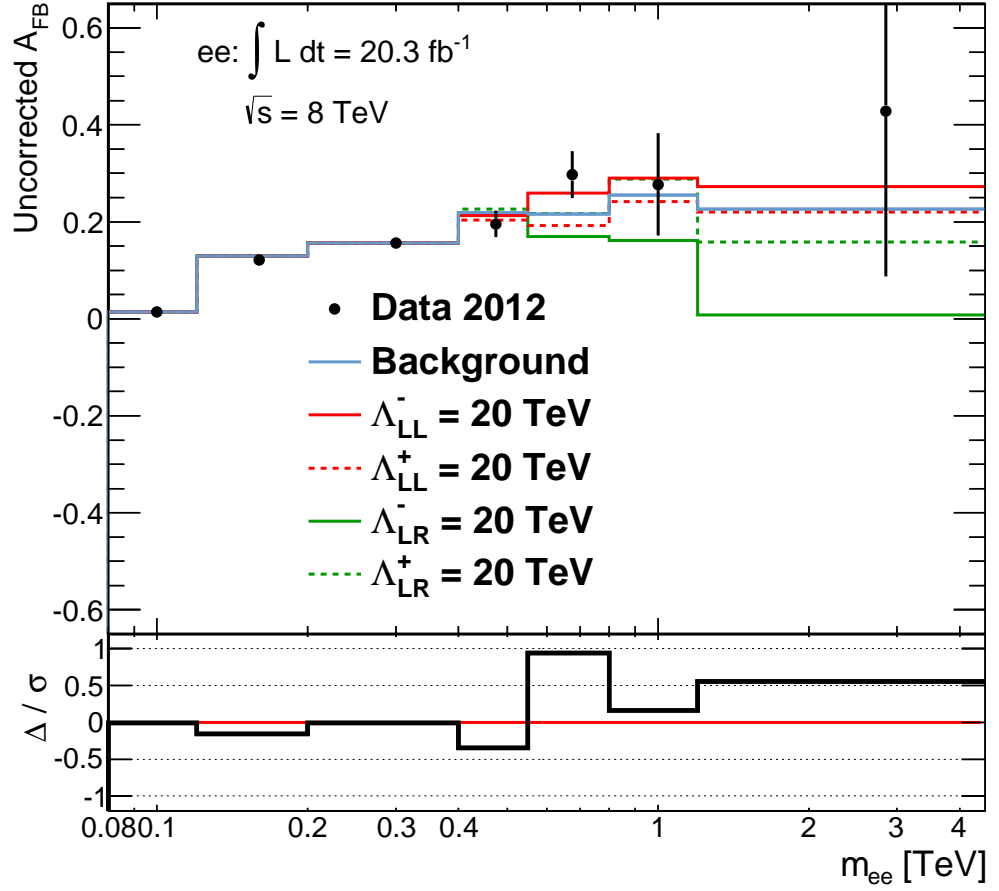


Figure A.1:  $A_{FB}$  comparison between data and MC with alternate signal overlay of CI. Ratio shows the difference between data and background prediction divided by total background systematic.

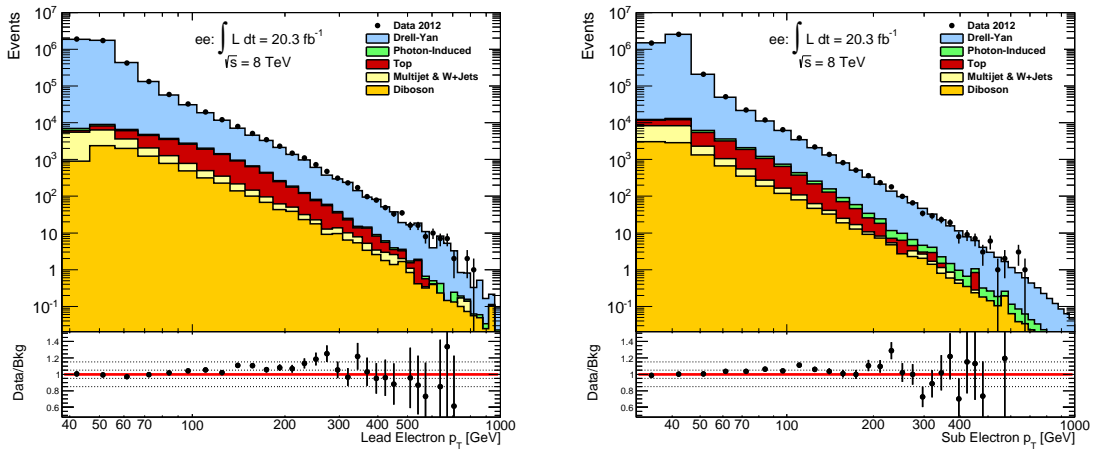


Figure A.2: Distribution of  $p_T$  of the selected highest (left) and second highest (right)  $p_T$  electrons comparing data to background prediction.

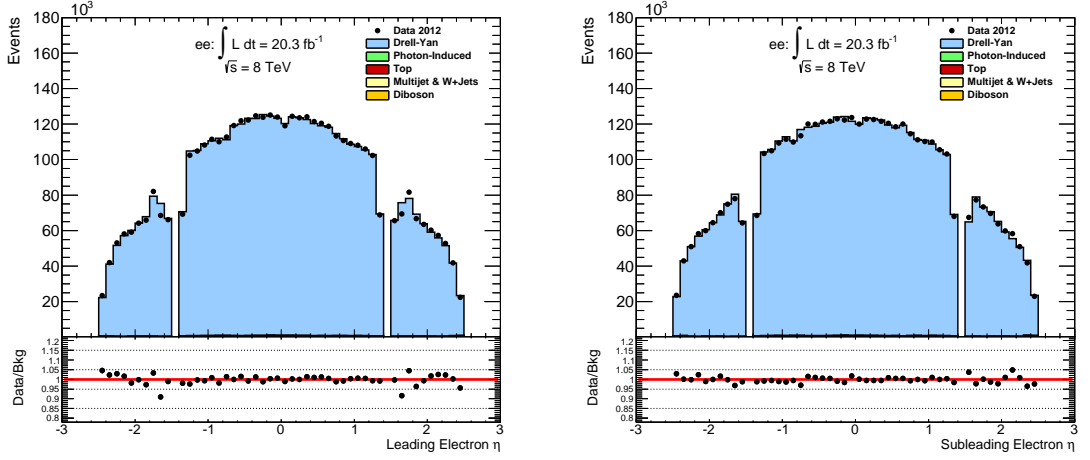


Figure A.3: Distribution of  $\eta$  of the selected highest (left) and second highest (right)  $p_T$  electrons comparing data to background prediction.

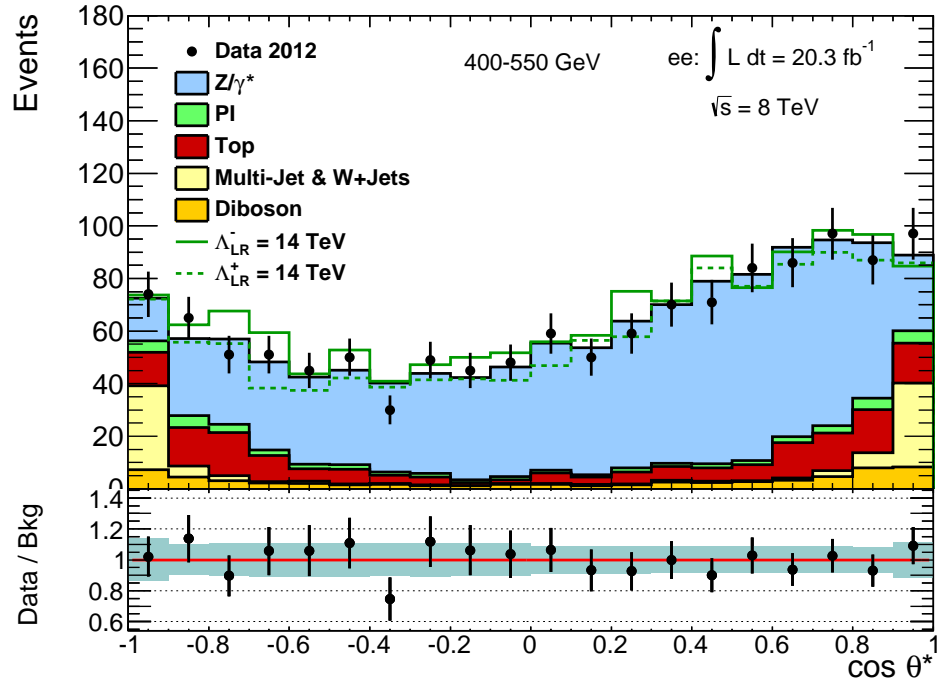


Figure A.4: Plot of  $\cos\theta^*$  comparing background to data in the invariant mass search bin 400-550 GeV with signal overlay.

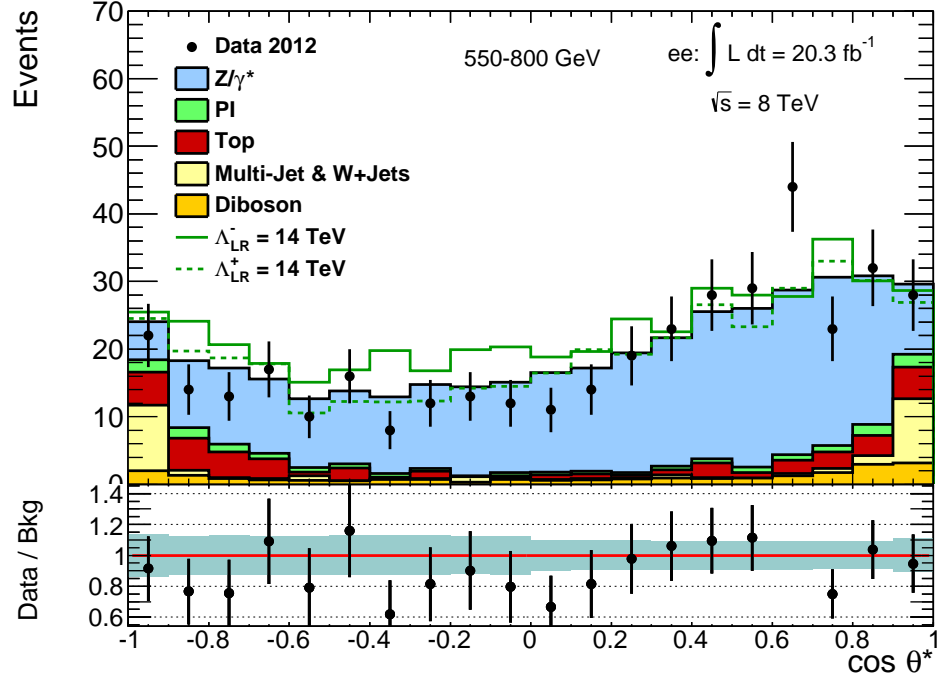


Figure A.5: Plot of  $\cos \theta^*$  comparing background to data in the invariant mass search bin 550-800 GeV with signal overlay.

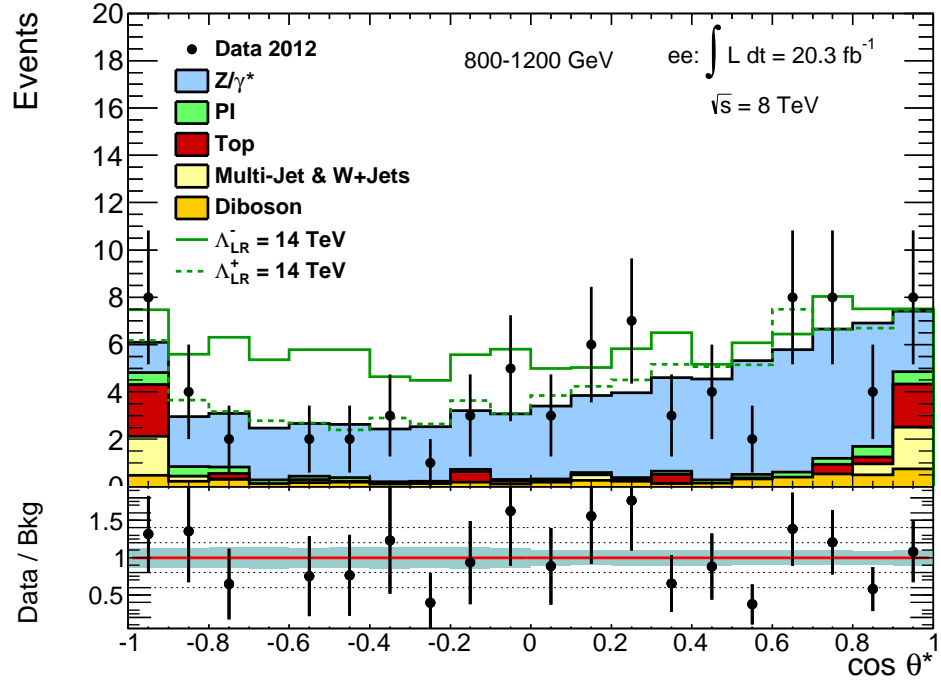


Figure A.6: Plot of  $\cos \theta^*$  comparing background to data in the invariant mass search bin 800-1200 GeV with signal overlay.

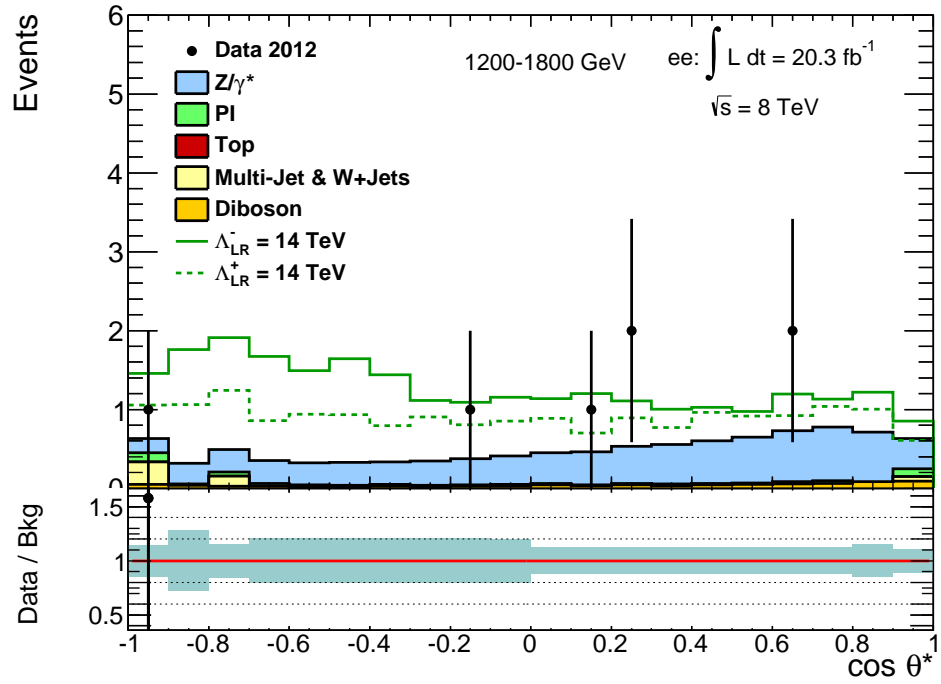


Figure A.7: Plot of  $\cos \theta^*$  comparing background to data in the invariant mass search bin 1200-1800 GeV with signal overlay.

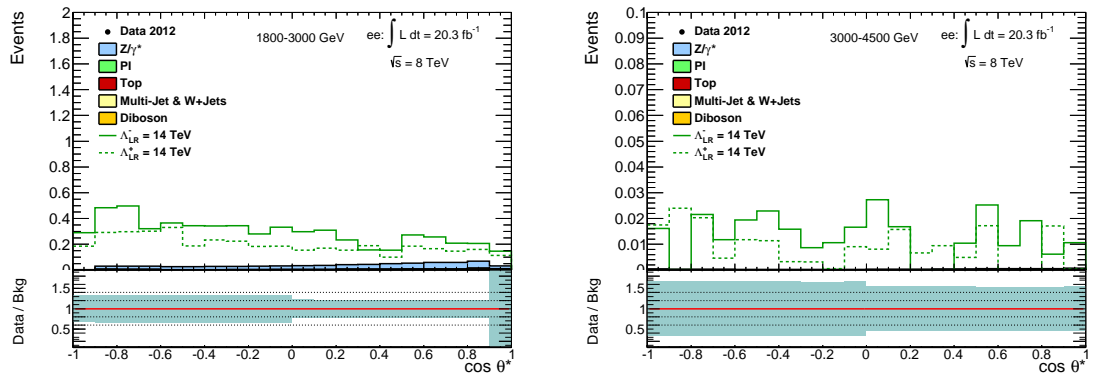


Figure A.8: Plot of  $\cos \theta^*$  comparing background to data in the invariant mass search bins 1800-3000 GeV and 3000-4500 GeV with signal overlay.

---

# Appendix B

## Signal Parametrisations

The appendix contains the parametrisations of signal within each search bin and for each formalism of CI. Parametrisations of each systematic are also included in each plot. Figures B.1, B.2, B.3 and B.4 parametrise the LL signal formalism while figures B.5, B.6, B.7 and B.8 do the same for the RR formalism and figures B.9, B.10, B.11 and B.12 for the LR formalism.

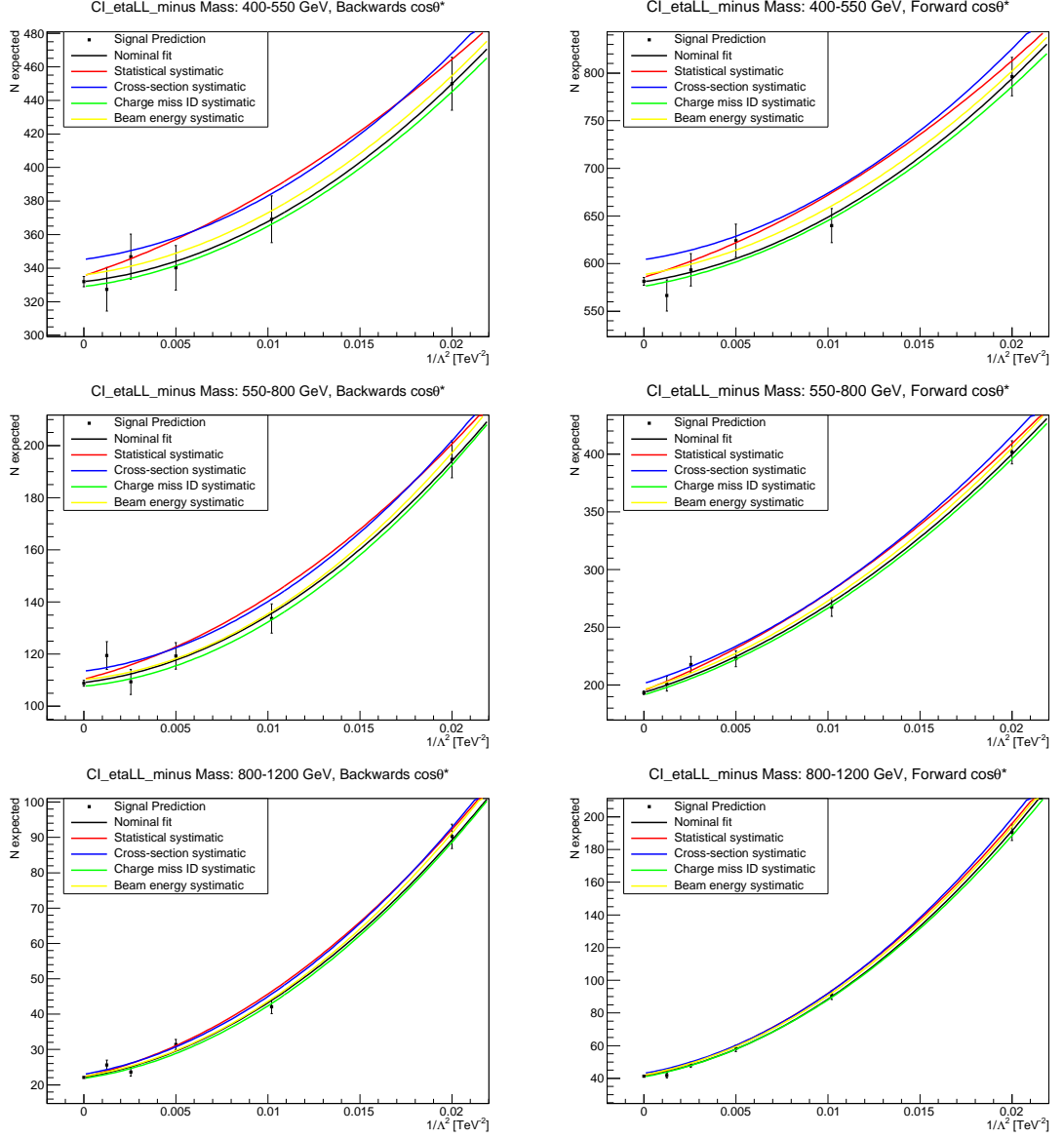


Figure B.1: Signal paramaterisations for the LL formalism with constructive interferences for low mass bins



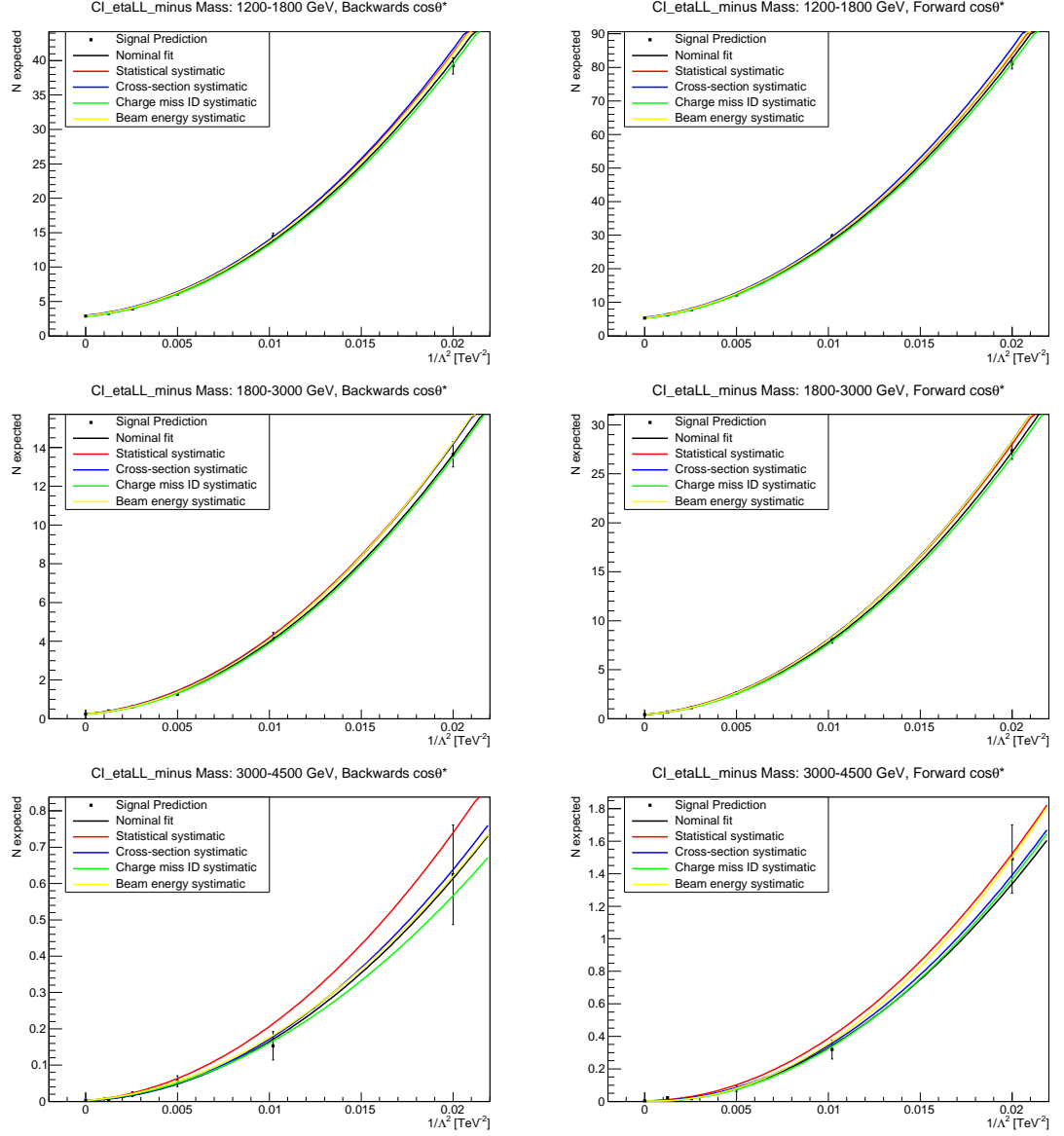


Figure B.2: Signal paramaterisations for the LL formalism with constructive interferences for high mass bins

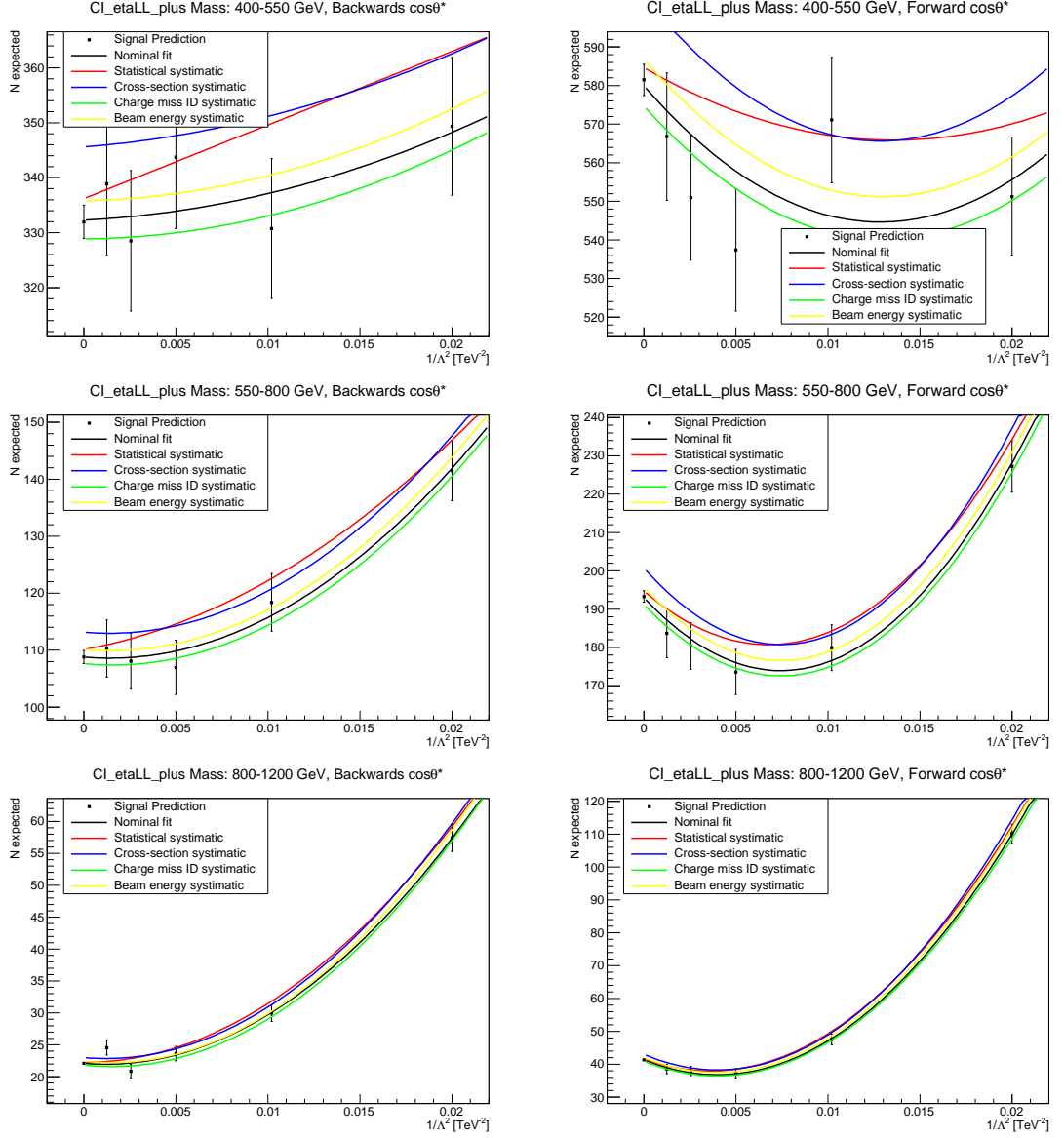


Figure B.3: Signal paramaterisations for the LL formalism with destructive interferences for low mass bins

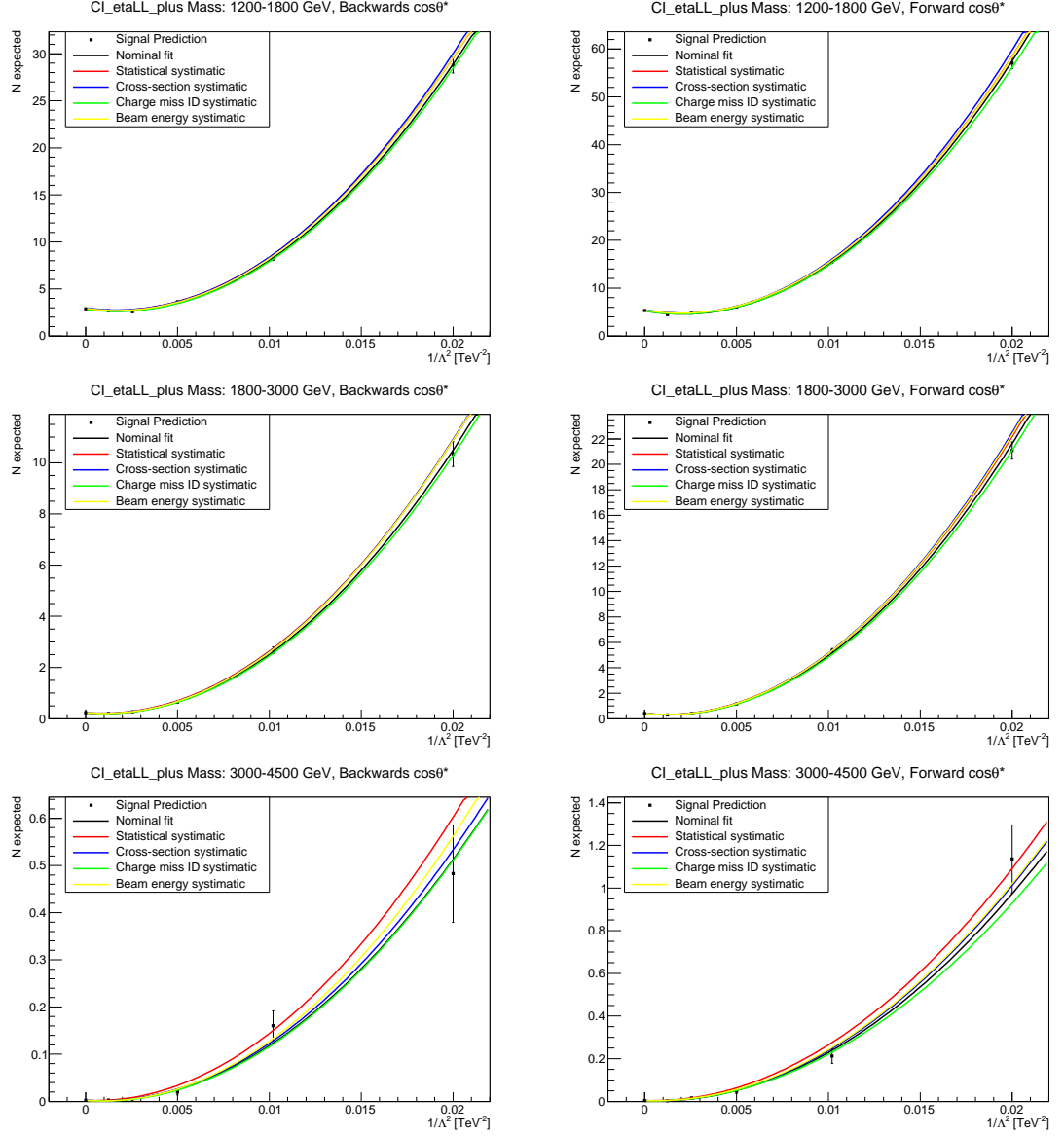


Figure B.4: Signal paramaterisations for the LL formalism with destructive interferences for high mass bins

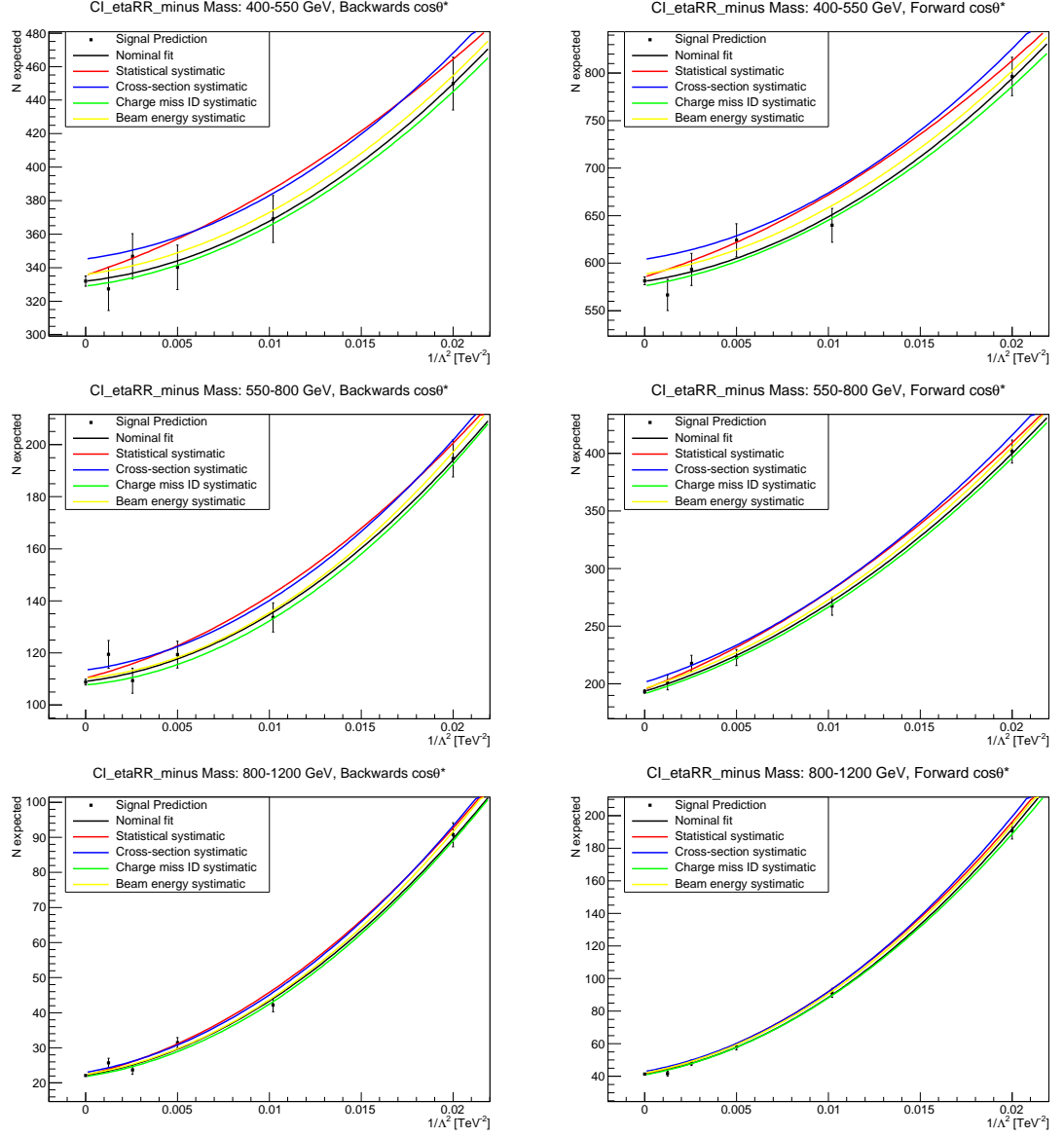


Figure B.5: Signal paramaterisations for the RR formalism with constructive interferences for low mass bins

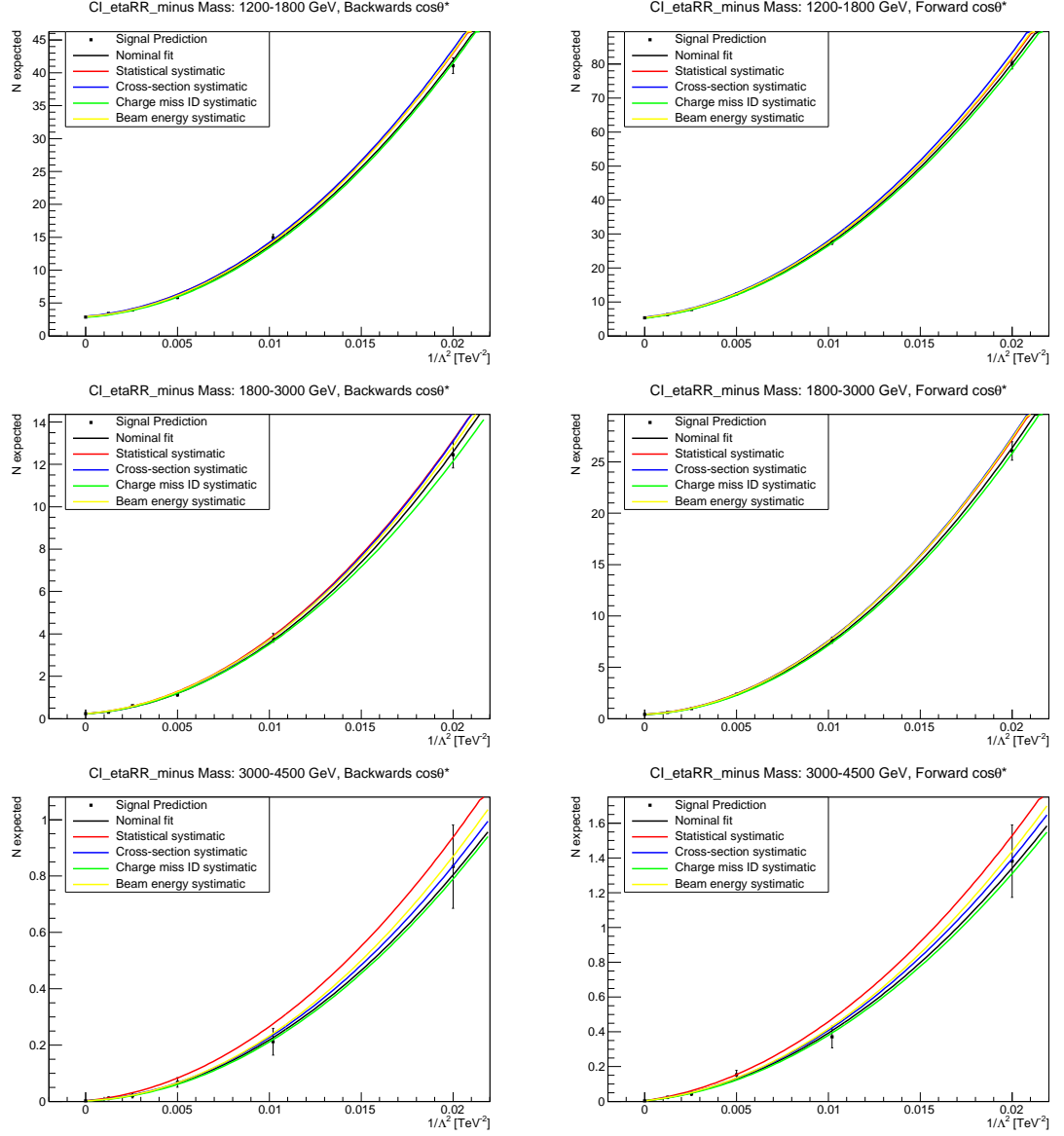


Figure B.6: Signal paramaterisations for the RR formalism with constructive interferences for high mass bins

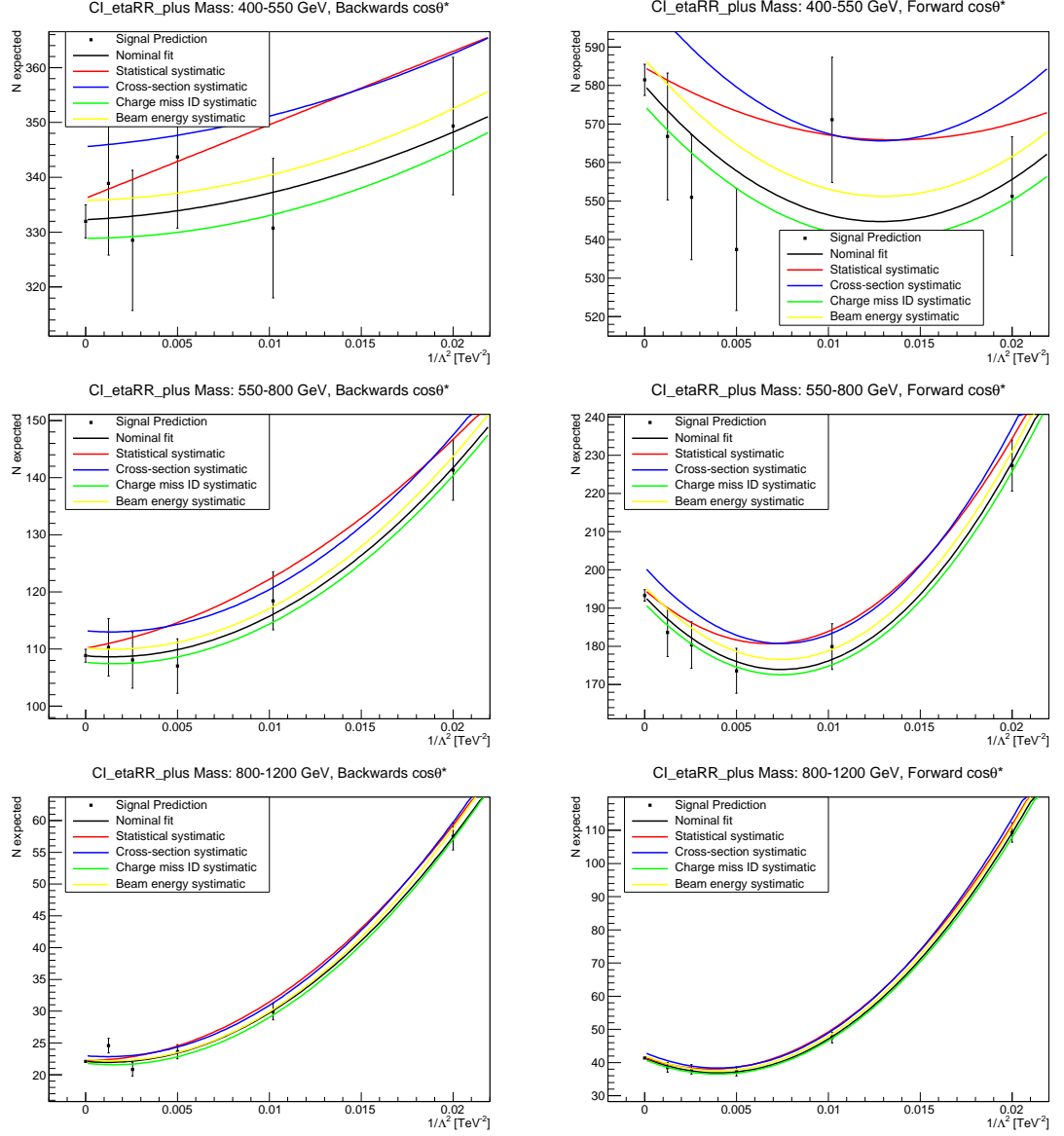


Figure B.7: Signal paramaterisations for the RR formalism with destructive interferences for low mass bins

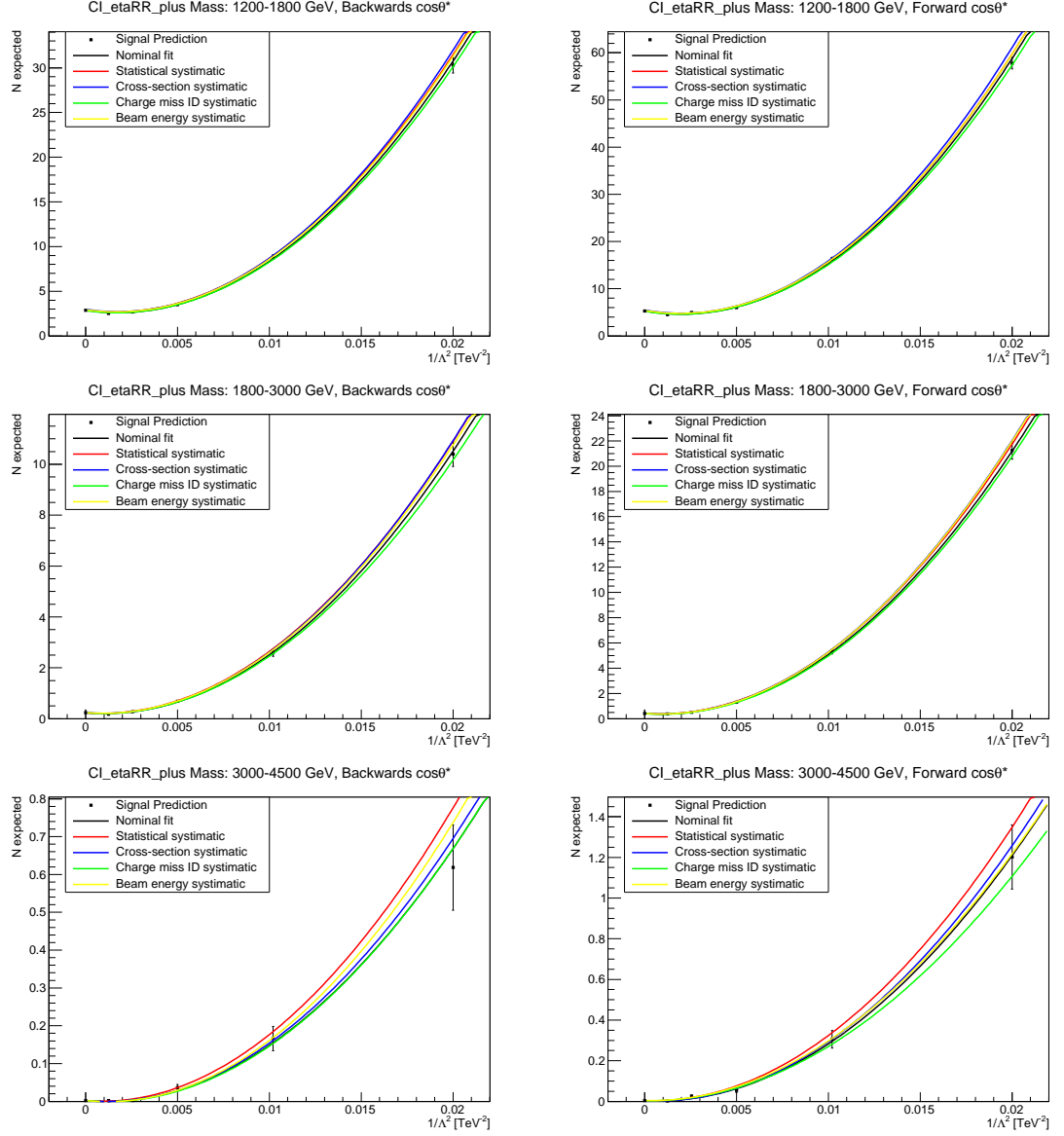


Figure B.8: Signal paramaterisations for the RR formalism with destructive interferences for high mass bins

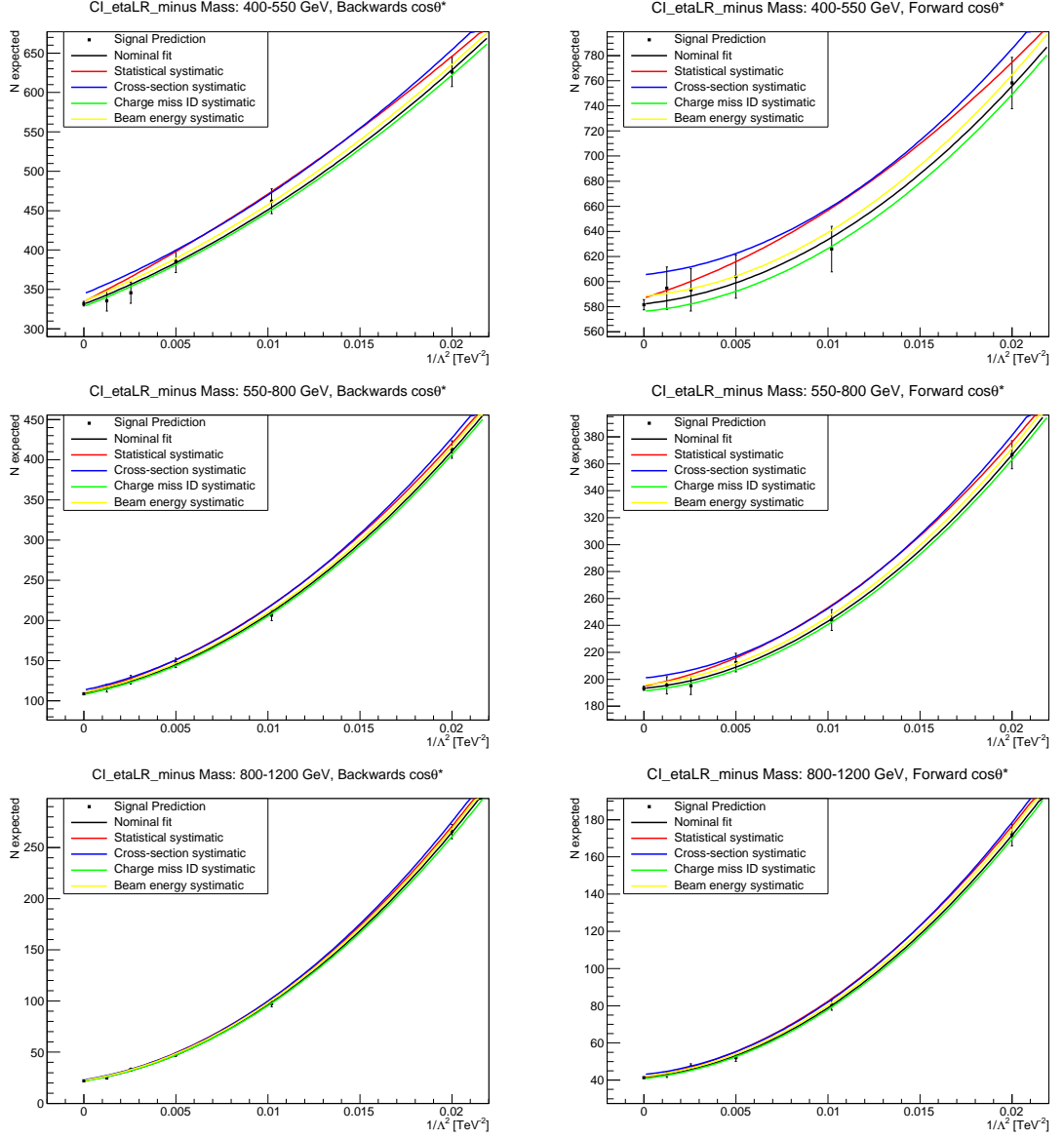


Figure B.9: Signal paramaterisations for the LR formalism with constructive interferences for low mass bins



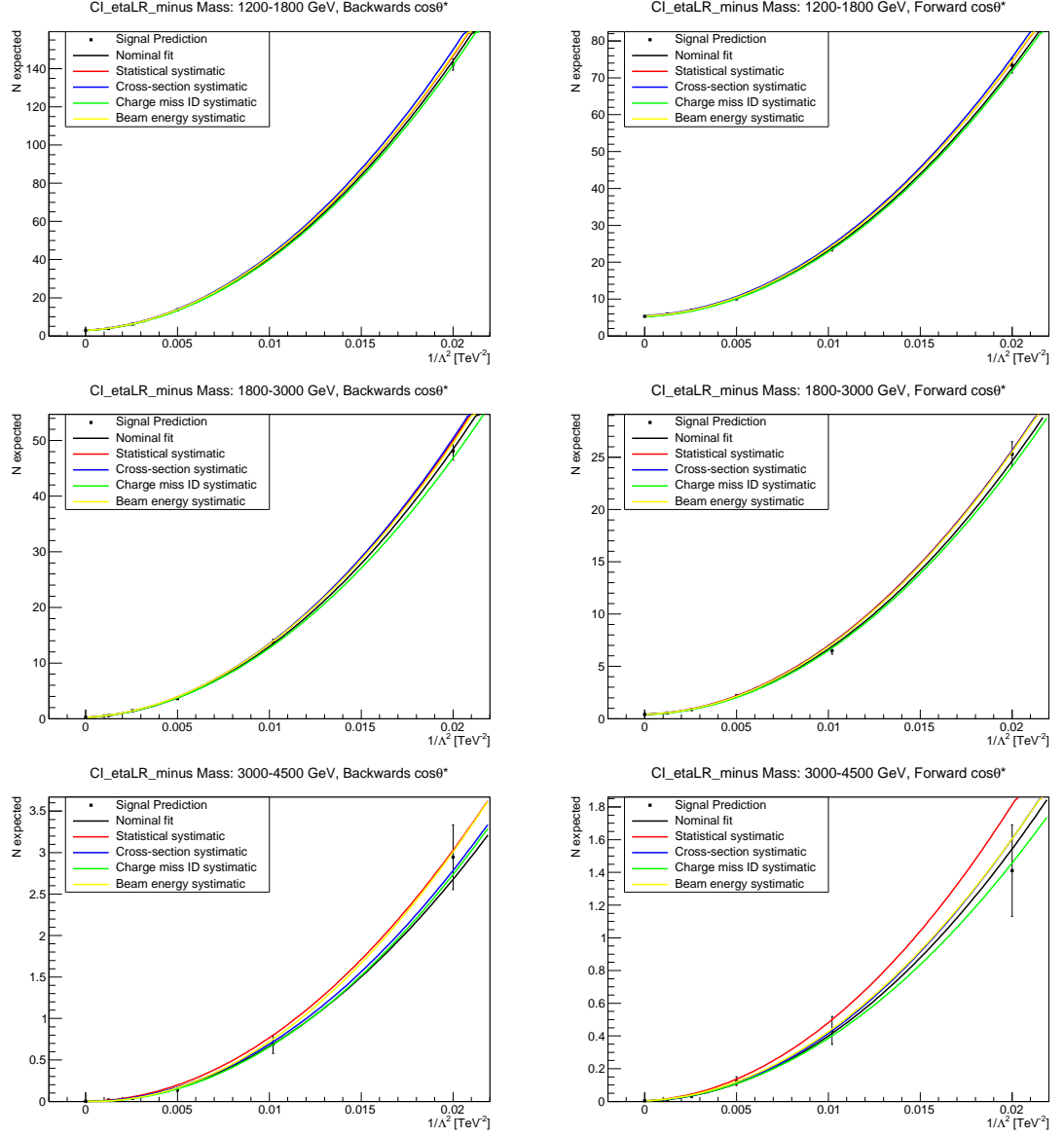


Figure B.10: Signal paramaterisations for the LR formalism with constructive interferences for high mass bins

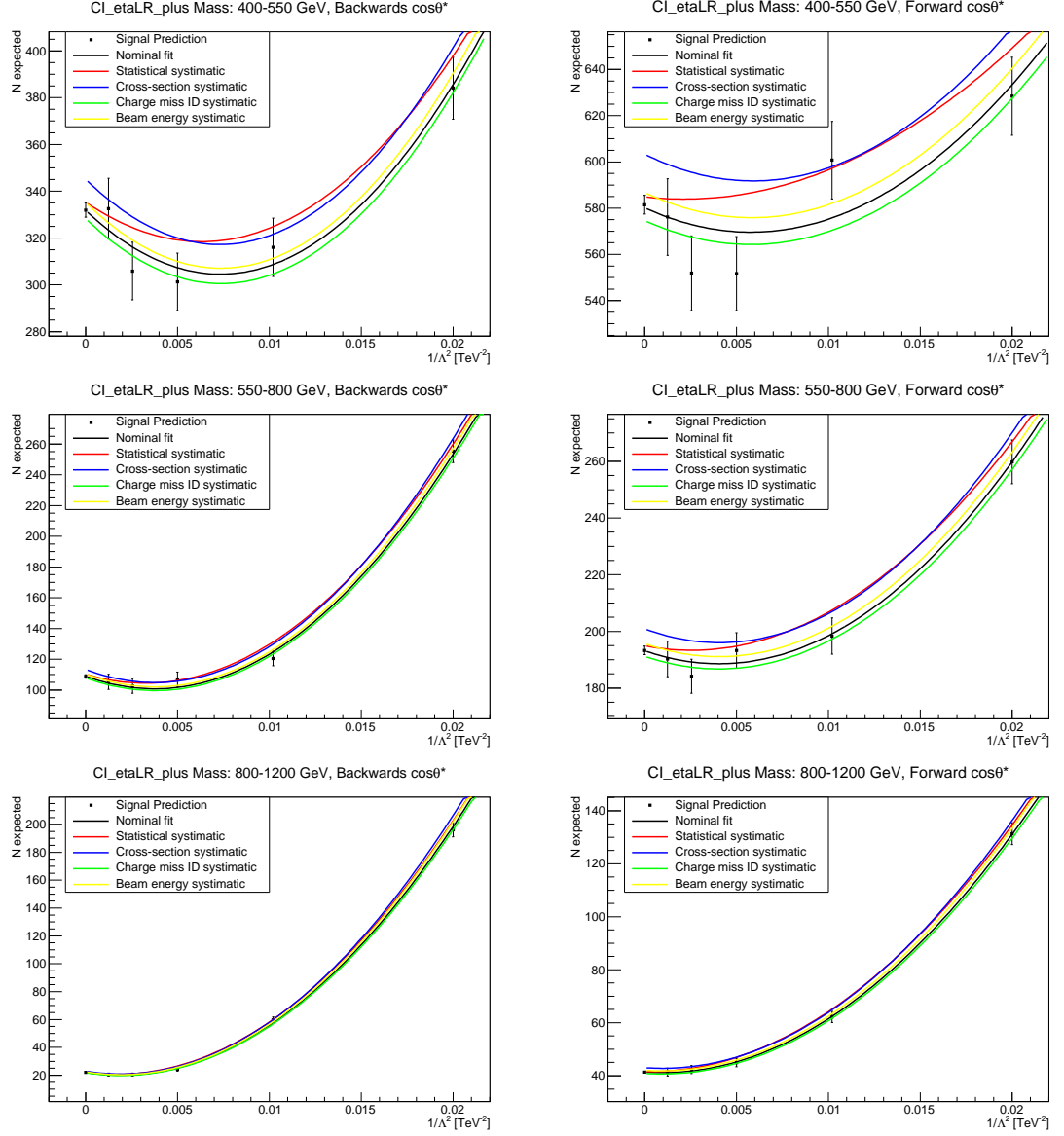


Figure B.11: Signal paramaterisations for the LR formalism with destructive interferences for low mass bins

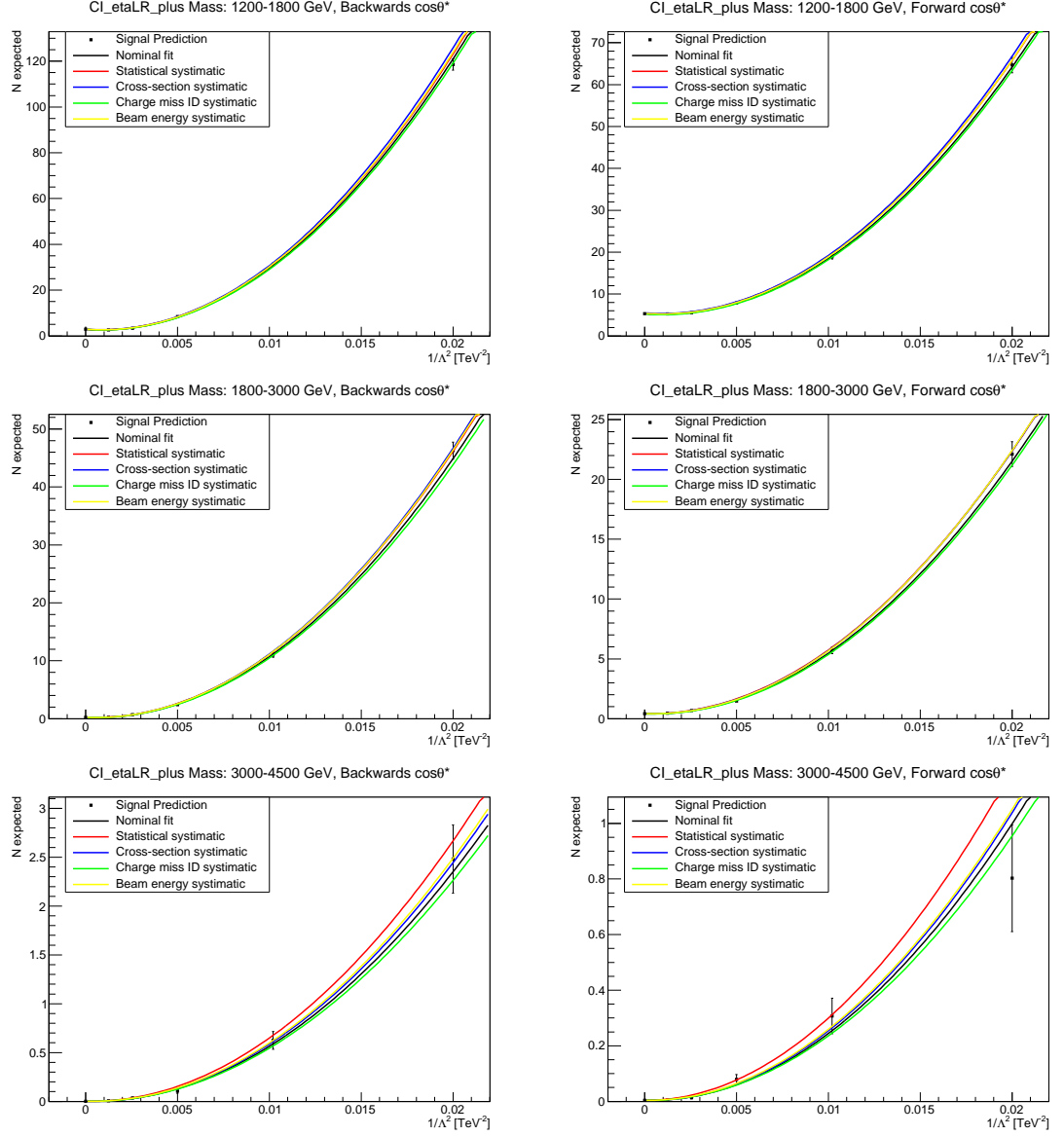


Figure B.12: Signal paramaterisations for the LR formalism with destructive interferences for high mass bins

# Appendix C

## Statistical Analysis Plots

This appendix contains a closer look at the statistical analysis plots. Figures C.1 and C.2 show the LLR distributions for the constructive and destructive signals respectively with the prior  $1/\Lambda^2$  and in figures C.3 and C.4 for the prior  $1/\Lambda^4$ . Figures C.5 and C.6 show the pseudo-experiments distributions with expected and observed limits for constructive and destructive interference respectively with a  $1/\Lambda^2$  prior and in figures C.7 and C.8 for the prior  $1/\Lambda^4$ .

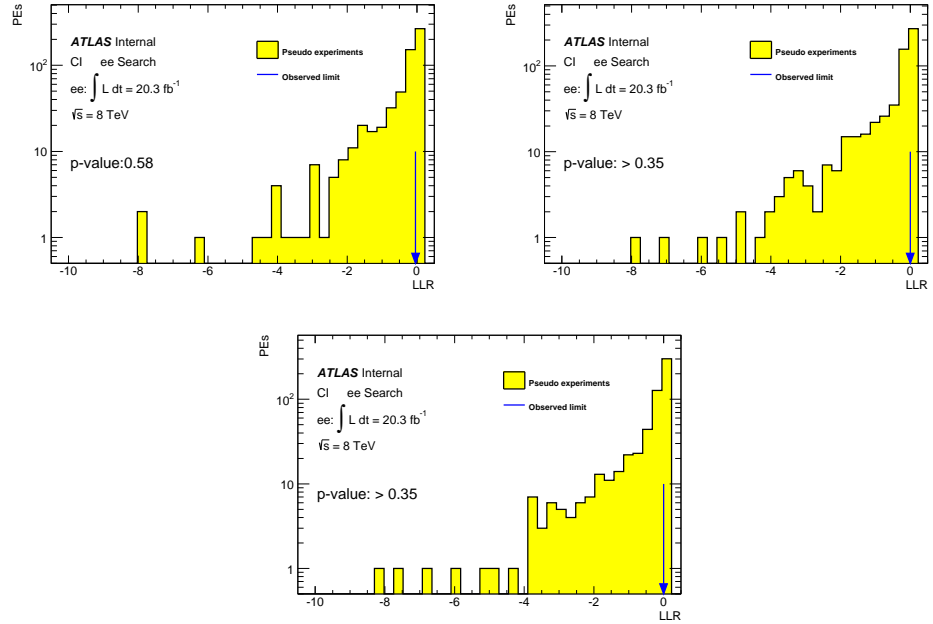


Figure C.1: Distribution of negative Log Likelihood Ratio's for the CI formalisms LL (top left), RR (top right) and LR (bottom) with constructive interference given a uniform positive prior in  $1/\Lambda^2$ .

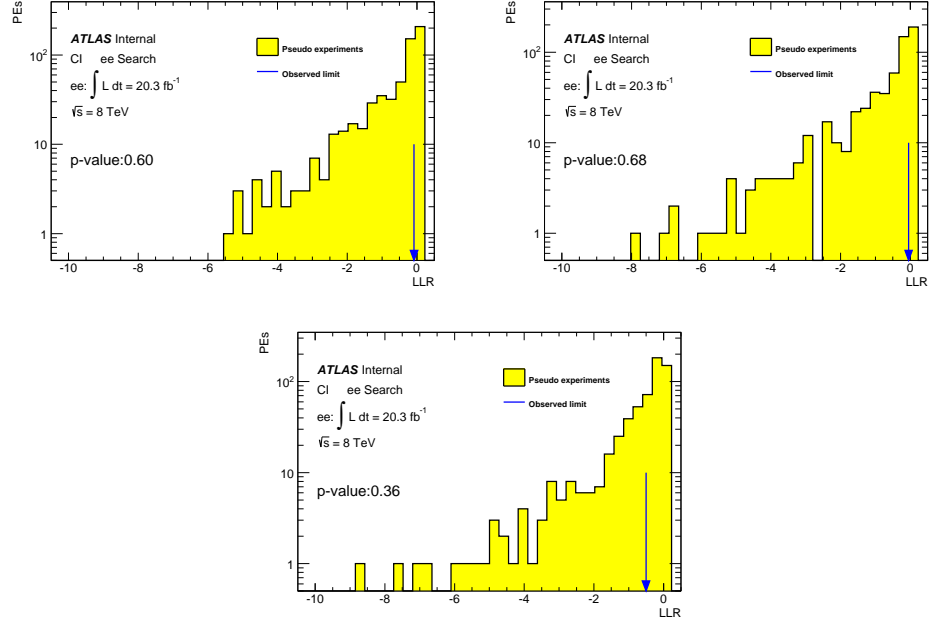


Figure C.2: Distribution of negative Log Likelihood Ratio's for the CI formalisms LL (top left), RR (top right) and LR (bottom) with destructive interference given a uniform positive prior in  $1/\Lambda^2$ .

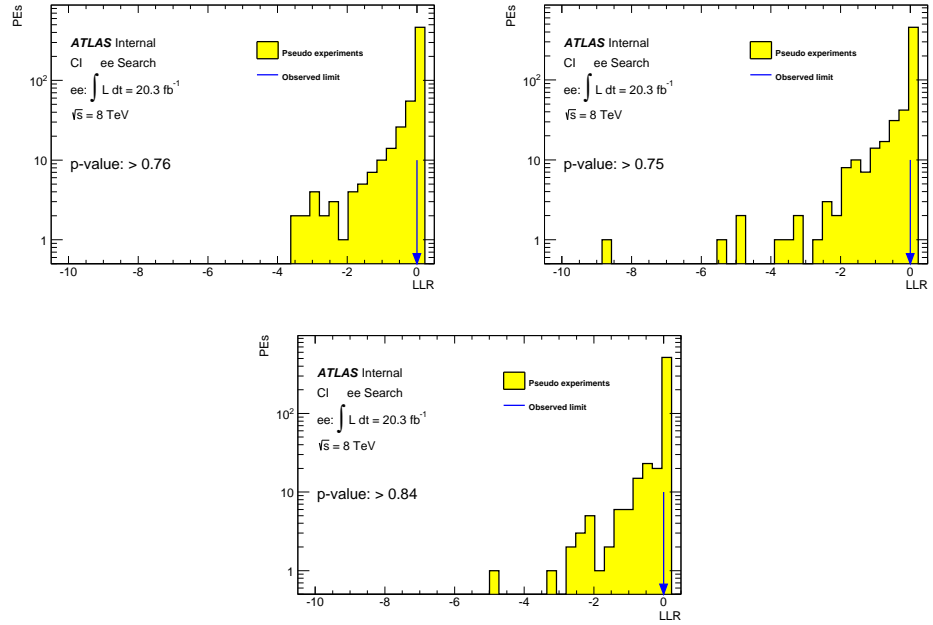


Figure C.3: Distribution of negative Log Likelihood Ratio's for the CI formalisms LL (top left), RR (top right) and LR (bottom) with constructive interference given a uniform positive prior in  $1/\Lambda^4$ .

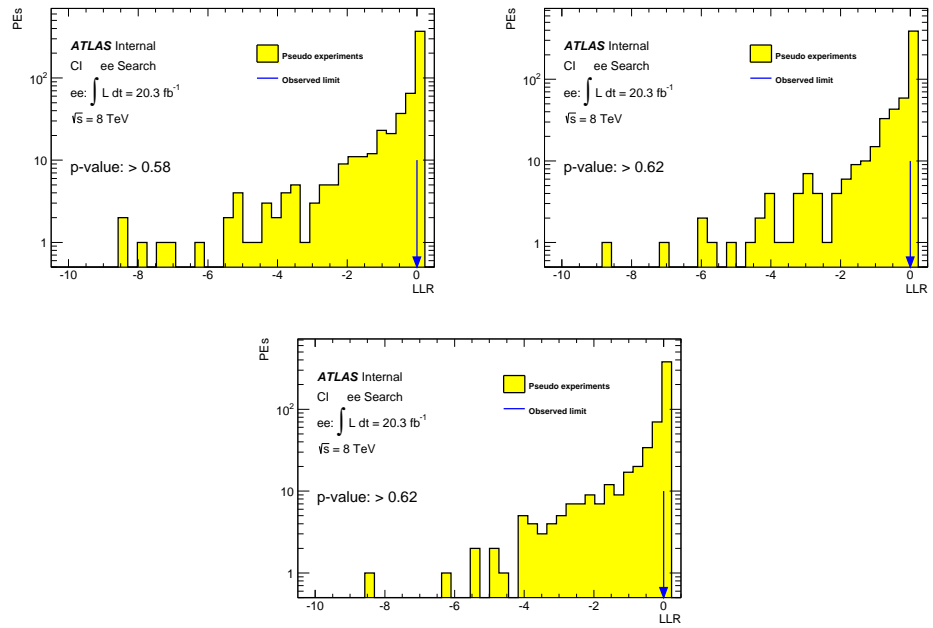


Figure C.4: Distribution of negative Log Likelihood Ratio's for the CI formalisms LL (top left), RR (top right) and LR (bottom) with destructive interference given a uniform positive prior in  $1/\Lambda^4$ .

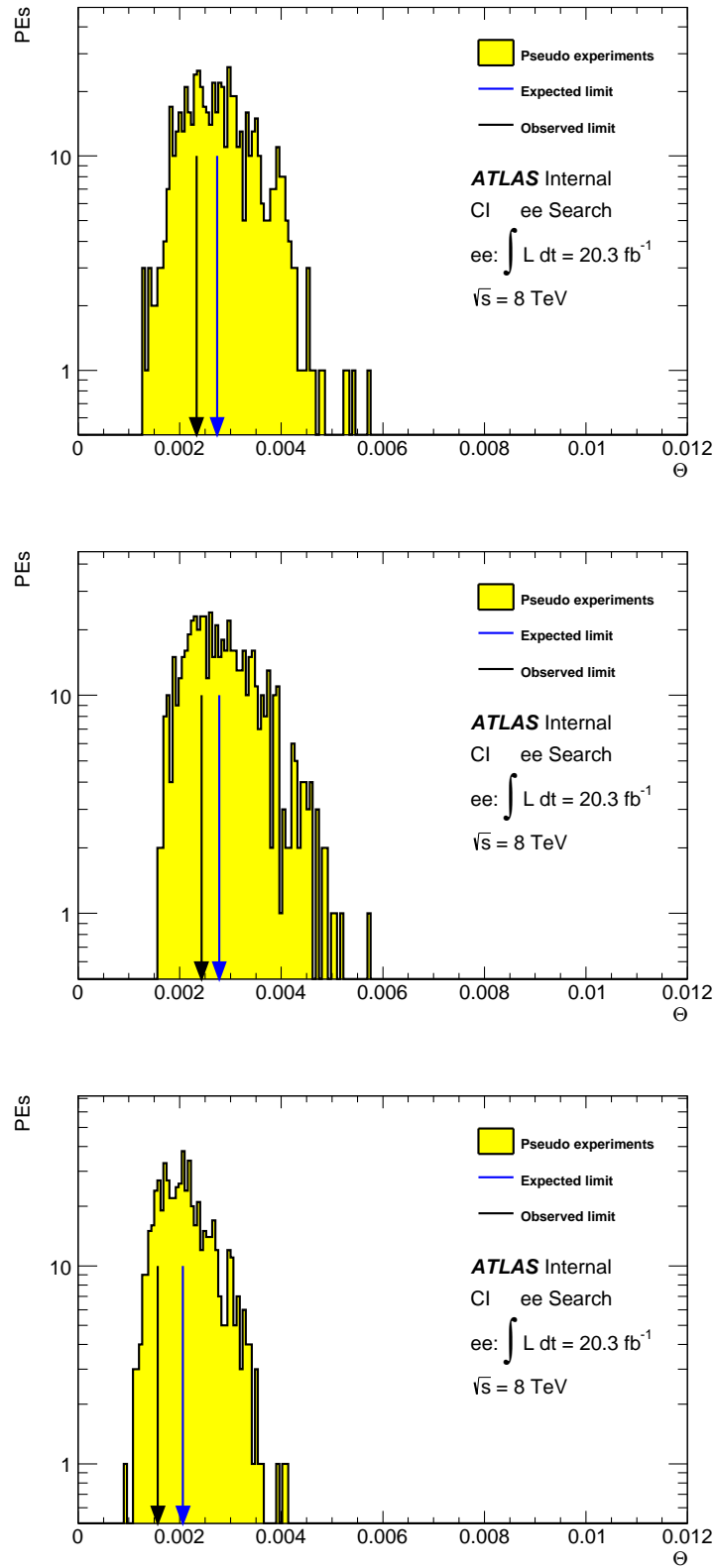


Figure C.5: Distribution of PE's with associated limits for CI formalisms LL (top), RR (middle) and LR (bottom) with constructive interference given a uniform positive prior in  $1/\Lambda^2$ . The mean value is shown as the expected limit for comparison to the observed limit shown.  $\Theta = 1/\Lambda^2$

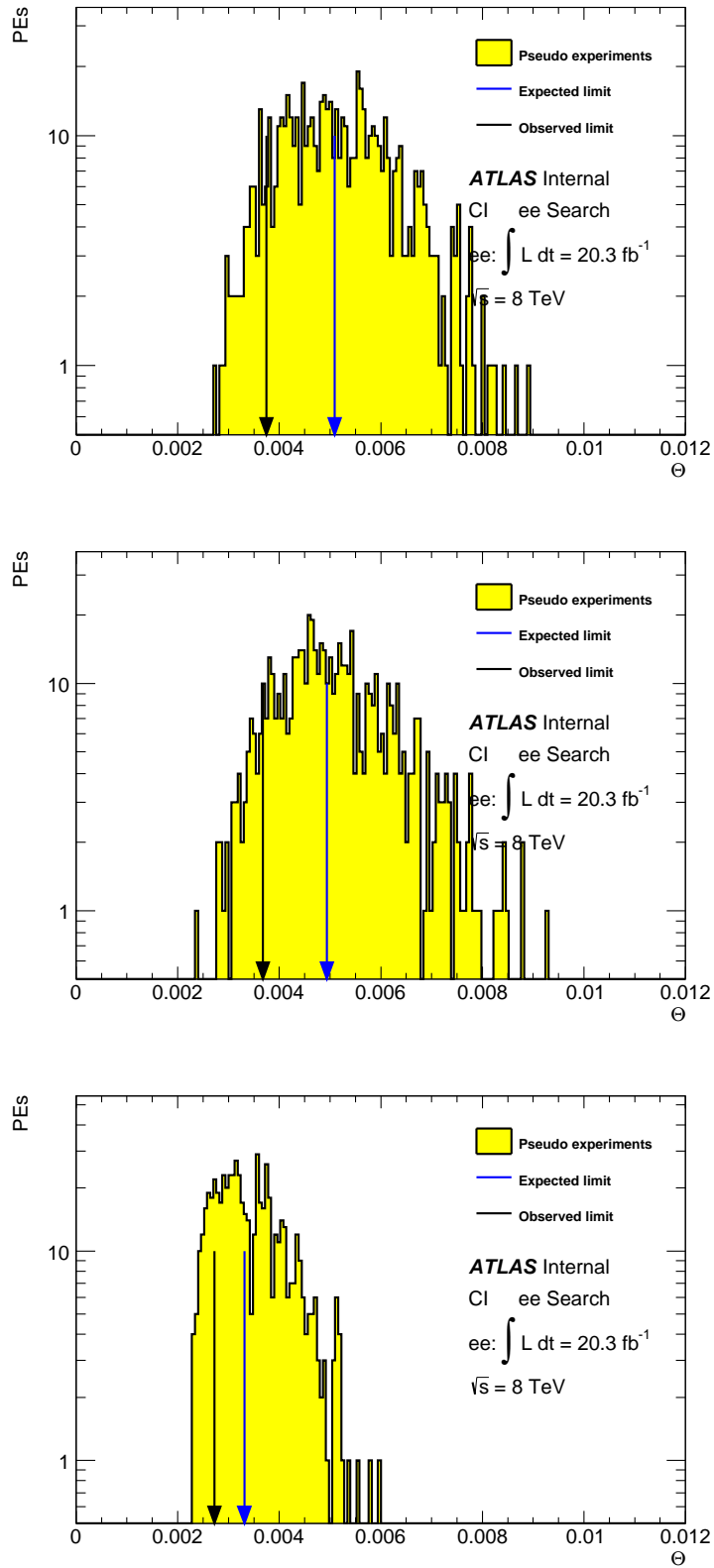


Figure C.6: Distribution of PE's with associated limits for CI formalisms LL (top), RR (middle) and LR (bottom) with destructive interference given a uniform positive prior in  $1/\Lambda^2$ . The mean value is shown as the expected limit for comparison to the observed limit shown.  $\Theta = 1/\Lambda^2$



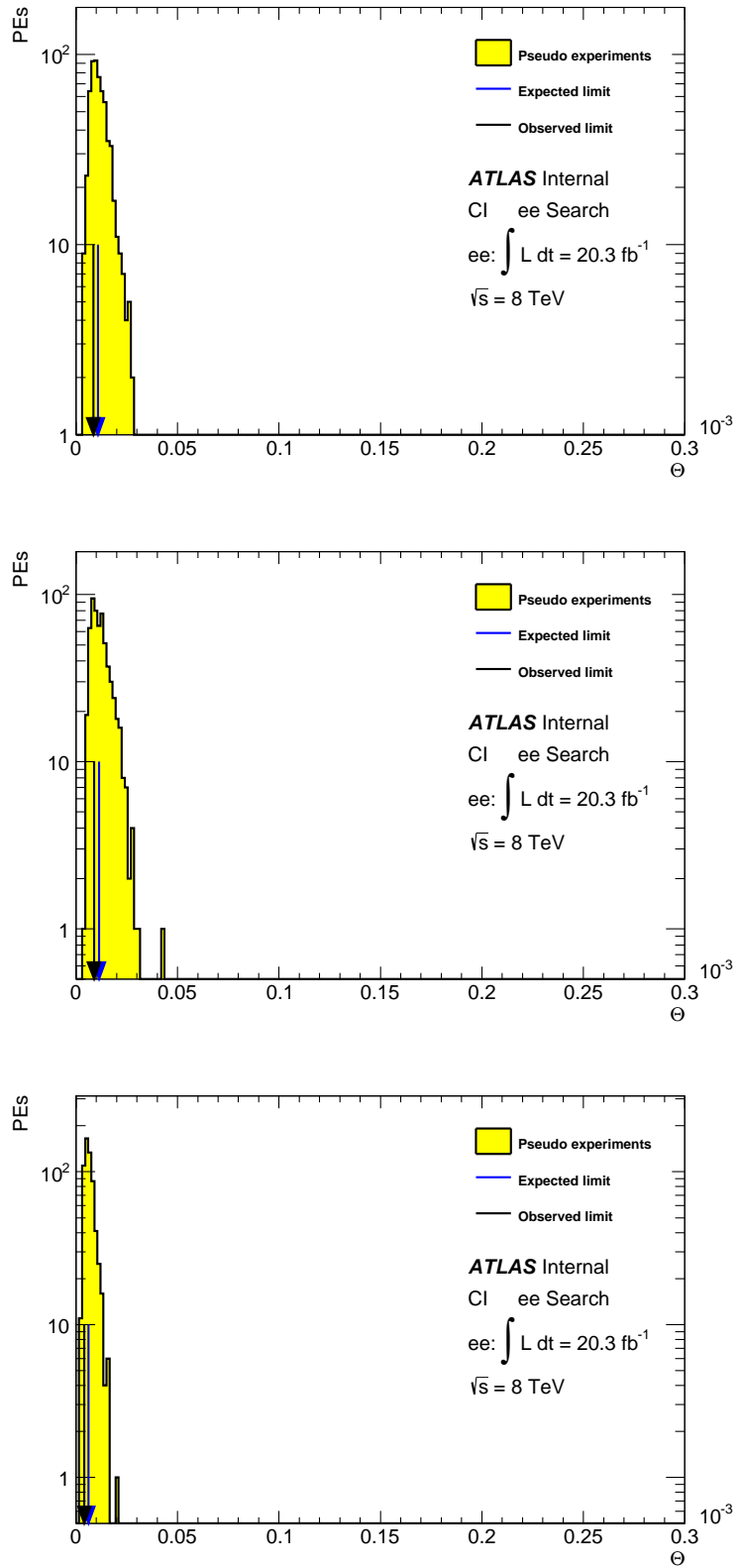


Figure C.7: Distribution of PE's with associated limits for CI formalisms LL (top), RR (middle) and LR (bottom) with constructive interference given a uniform positive prior in  $1/\Lambda^4$ . The mean value is shown as the expected limit for comparison to the observed limit shown.  $\Theta = 1/\Lambda^4$

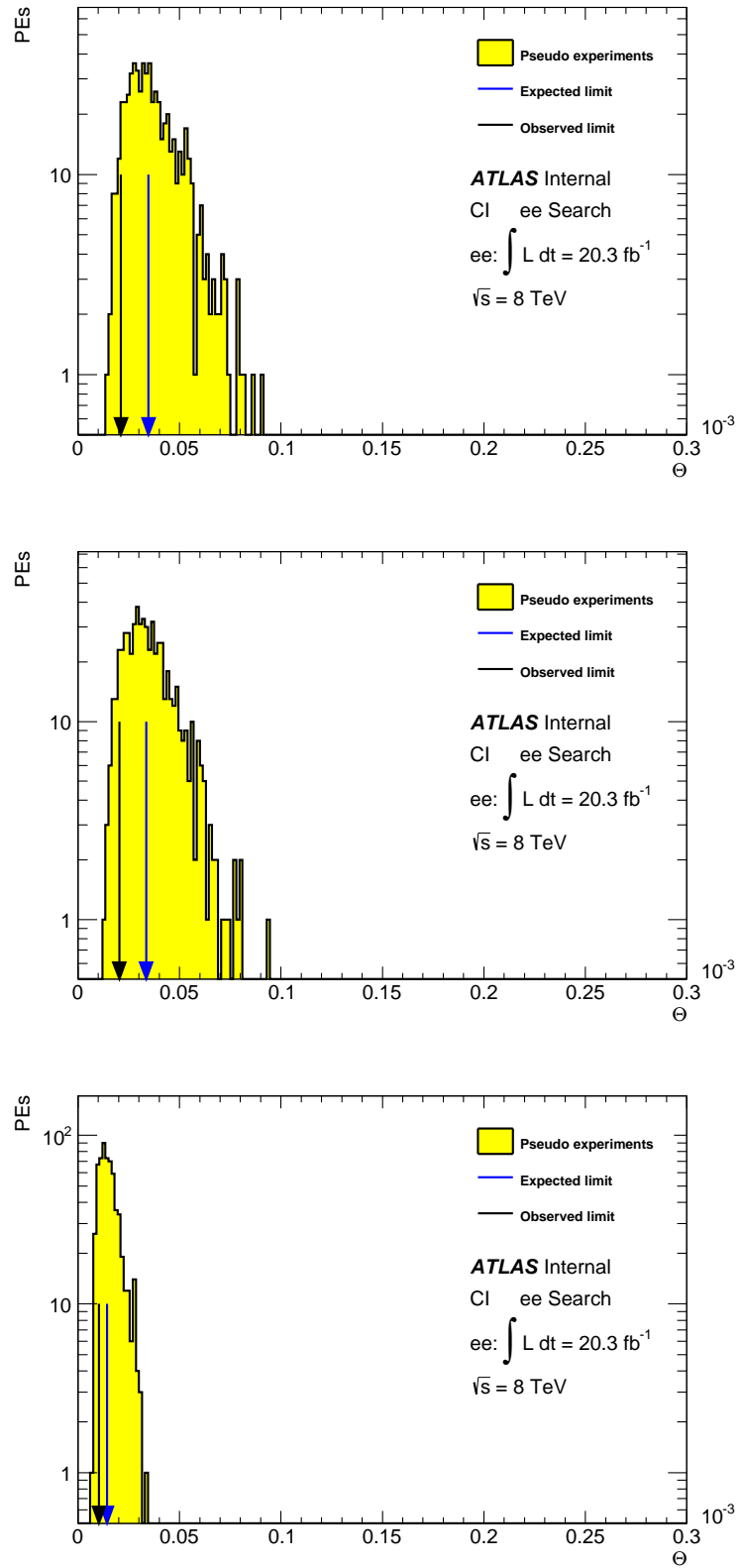


Figure C.8: Distribution of PE's with associated limits for CI formalisms LL (top), RR (middle) and LR (bottom) with destructive interference given a uniform positive prior in  $1/\Lambda^4$ . The mean value is shown as the expected limit for comparison to the observed limit shown.  $\Theta = 1/\Lambda^4$

---

# Bibliography

- [1] G. Aad, et al., Search for contact interactions and large extra dimensions in dilepton events from pp collisions at  $\sqrt{s} = 7$  TeV with the ATLAS detector, Phys. Rev. D **87** (2013) 015010. doi:10.1103/PhysRevD.87.015010. (pages 8, 19, 24, 24, 25, 25, 93, 103, 104).
- [2] Search for contact interactions and large extra dimensions in the dilepton channel using proton-proton collisions at  $\sqrt{s} = 8$  TeV with the ATLAS detector, Tech. Rep. ATLAS-CONF-2014-030, CERN, Geneva (Jun 2014). (page 8).
- [3] G. Aad, et al., Search for high-mass resonances decaying to dilepton final states in pp collisions at  $\sqrt{s} = 7$  TeV with the ATLAS detector, JHEP **1211** (2012) 138. arXiv:1209.2535, doi:10.1007/JHEP11(2012)138. (page 8).
- [4] Search for high-mass dilepton resonances in  $20\text{ fb}^{-1}$  of  $pp$  collisions at  $\sqrt{s} = 8$  TeV with the ATLAS experiment, Tech. Rep. ATLAS-COM-CONF-2013-010, CERN, Geneva (Feb 2013). (page 8).
- [5] Expected photon performance in the ATLAS experiment, Tech. Rep. ATL-PHYS-PUB-2011-007, CERN, Geneva (Apr 2011). (page 8).
- [6] L. Duguid, Performance of the ATLAS Electron and Photon Trigger in p-p Collisions at  $\sqrt{s} = 7$  TeV in 2011, Tech. Rep. ATL-DAQ-SLIDE-2012-283 (May 2012). (page 8).
- [7] D. Griffiths, Introduction to Elementary Particles, 2nd Edition, Wiley-VCH, 2008. (page 12).

- [8] S. L. Glashow, Partial-symmetries of weak interactions, *Nuclear Physics* **22** (4) (1961) 579 – 588. doi:[http://dx.doi.org/10.1016/0029-5582\(61\)90469-2](http://dx.doi.org/10.1016/0029-5582(61)90469-2). (page 16).
- [9] S. Weinberg, A model of leptons, *Phys. Rev. Lett.* **19** (1967) 1264–1266. doi:[10.1103/PhysRevLett.19.1264](https://doi.org/10.1103/PhysRevLett.19.1264). (page 16).
- [10] A. Salam, Weak and electromagnetic interactions *Proc. of the 8th Nobel Symposium on ‘Elementary Particle Theory, Relativistic Groups and Analyticity’*, Stockholm, Sweden, 1968, edited by N. Svartholm, p. 367-377. (page 16).
- [11] F. Englert, R. Brout, Broken symmetry and the mass of gauge vector mesons, *Phys. Rev. Lett.* **13** (1964) 321–323. doi:[10.1103/PhysRevLett.13.321](https://doi.org/10.1103/PhysRevLett.13.321). (page 17).
- [12] P. W. Higgs, Broken symmetries and the masses of gauge bosons, *Phys. Rev. Lett.* **13** (1964) 508–509. doi:[10.1103/PhysRevLett.13.508](https://doi.org/10.1103/PhysRevLett.13.508). (page 17).
- [13] G. S. Guralnik, C. R. Hagen, T. W. B. Kibble, Global conservation laws and massless particles, *Phys. Rev. Lett.* **13** (1964) 585–587. doi:[10.1103/PhysRevLett.13.585](https://doi.org/10.1103/PhysRevLett.13.585). (page 17).
- [14] G. Aad, et al., Observation of a new particle in the search for the standard model higgs boson with the ATLAS detector at the LHC, *Phys. Lett. B* **716** (1) (2012) 1 – 29. doi:<http://dx.doi.org/10.1016/j.physletb.2012.08.020>. (page 17).
- [15] S. Chatrchyan, et al., Observation of a new boson at a mass of 125 gev with the CMS experiment at the LHC, *Phys. Lett. B* **716** (1) (2012) 30 – 61. doi:<http://dx.doi.org/10.1016/j.physletb.2012.08.021>. (page 17).
- [16] E. Eichten, K. D. Lane, M. E. Peskin, New Tests for Quark and Lepton Substructure, *Phys. Rev. Lett.* **50** (1983) 811–814. doi:[10.1103/PhysRevLett.50.811](https://doi.org/10.1103/PhysRevLett.50.811). (page 18).
- [17] V. M. Abazov, et al., Measurement of dijet angular distributions at  $s=1.96\text{TeV}$  and searches for quark compositeness and extra spatial dimensions, *Phys. Rev. Lett.* **103** (2009) 191803. doi:[10.1103/PhysRevLett.103.191803](https://doi.org/10.1103/PhysRevLett.103.191803). (pages 19, 24, 25).

- [18] A. Abulencia, et al., Search for  $Z' \rightarrow e+e-$  using dielectron mass and angular distribution, *Phys. Rev. Lett.* **96** (2006) 211801. doi:10.1103/PhysRevLett.96.211801. (pages 19, 24, 24).
- [19] J. C. Collins, D. E. Soper, Angular distribution of dileptons in high-energy hadron collisions, *Phys. Rev. D* **16** (1977) 2219–2225. doi:10.1103/PhysRevD.16.2219. (page 20).
- [20] N. Arkani-Hamed, S. Dimopoulos, G. Dvali, The Hierarchy problem and new dimensions at a millimeter, *Phys.Lett.* **B429** (1998) 263–272. arXiv:hep-ph/9803315, doi:10.1016/S0370-2693(98)00466-3. (page 21).
- [21] G. F. Giudice, R. Rattazzi, J. D. Wells, Quantum gravity and extra dimensions at high-energy colliders, *Nucl.Phys.* **B544** (1999) 3–38. arXiv:hep-ph/9811291, doi:10.1016/S0550-3213(99)00044-9. (page 23).
- [22] T. Han, J. D. Lykken, R.-J. Zhang, Kaluza-Klein states from large extra dimensions, *Phys. Rev. D* **59** (1999) 105006. doi:10.1103/PhysRevD.59.105006. (page 23).
- [23] J. L. Hewett, Indirect collider signals for extra dimensions, *Phys. Rev. Lett.* **82** (1999) 4765–4768. doi:10.1103/PhysRevLett.82.4765. (page 23).
- [24] L. Randall, R. Sundrum, Large mass hierarchy from a small extra dimension, *Phys. Rev. Lett.* **83** (1999) 3370–3373. doi:10.1103/PhysRevLett.83.3370. (page 23).
- [25] G. Aad, et al., ATLAS search for new phenomena in dijet mass and angular distributions using  $pp$  collisions at  $\sqrt{s} = 7$  TeV, *JHEP* **1301** (2013) 029. arXiv:1210.1718, doi:10.1007/JHEP01(2013)029. (page 24).
- [26] S. Chatrchyan, et al., Search for contact interactions in  $\mu+\mu-$  events in  $pp$  collisions at  $s=7$  TeV, *Phys. Rev. D* **87** (2013) 032001. doi:10.1103/PhysRevD.87.032001. (page 24, 24).
- [27] S. Chatrchyan, et al., Search for contact interactions using the inclusive jet  $p_T$  spectrum in  $pp$  collisions at  $s=7$  TeV, *Phys. Rev. D* **87** (2013) 052017. doi:10.1103/PhysRevD.87.052017. (page 24).

- [28] T. Affolder, et al., Search for quark-lepton compositeness and a heavy  $W'$  boson using the  $e\nu$  channel in  $p\bar{p}$  collisions at  $s=1.8$  TeV, *Phys. Rev. Lett.* **87** (2001) 231803. doi:10.1103/PhysRevLett.87.231803. (page 24).
- [29] B. Abbott, et al., Measurement of the high-mass drell-yan cross section and limits on quark-electron compositeness scales, *Phys. Rev. Lett.* **82** (1999) 4769–4774. doi:10.1103/PhysRevLett.82.4769. (page 24).
- [30] F. Abe, et al., Limits on quark-lepton compositeness scales from dileptons produced in 1.8 TeV  $p\bar{p}$  collisions, *Phys. Rev. Lett.* **79** (1997) 2198–2203. doi:10.1103/PhysRevLett.79.2198. (page 24).
- [31] G. Abbiendi et al., Multi-photon production in  $ee$  collisions at  $\sqrt{s} = 181\text{--}209$  {GeV}, *The European Physical Journal C - Particles and Fields* **26** (3) (2003) 331–344. doi:10.1140/epjc/s2002-01074-5. (pages 24, 25).
- [32] G. Abbiendi et al., Tests of the standard model and constraints on new physics from measurements of fermion-pair production at 189 gev at lep, *The European Physical Journal C - Particles and Fields* **13** (4) (2000) 553–572. doi:10.1007/s100520000315. (pages 24, 25).
- [33] S. Chekanov, et al., Search for contact interactions, large extra dimensions and finite quark radius in  $ep$  collisions at HERA, *Physics Letters B* **591** (12) (2004) 23 – 41. doi:http://dx.doi.org/10.1016/j.physletb.2004.03.081. (pages 24, 25).
- [34] C. Adloff, et al., Search for compositeness, leptoquarks and large extra dimensions in  $eq$  contact interactions at HERA, *Physics Letters B* **479** (4) (2000) 358 – 370. doi:http://dx.doi.org/10.1016/S0370-2693(00)00332-4. (pages 24, 25).
- [35] C. Adloff, et al., Search for new physics in  $e\pm q$  contact interactions at HERA, *Physics Letters B* **568** (12) (2003) 35 – 47. doi:http://dx.doi.org/10.1016/j.physletb.2003.06.034. (page 24).
- [36] J. Abdallah, et al., A study of  $b\bar{b}$  production in  $e+e^-$  collisions at  $\sqrt{s} = 130 - 207$  GeV, *The European Physical Journal C* **60** (1) (2009) 1–15. doi:10.1140/epjc/s10052-009-0917-2. (page 24).

- [37] S. Schael, et al., Fermion pair production in e+e- collisions at 189-209 GeV and constraints on physics beyond the standard model, *The European Physical Journal C* **49** (2) (2007) 411–437. doi:10.1140/epjc/s10052-006-0156-8. (page 24).
- [38] J. Abdallah, et al., Measurement and interpretation of fermion-pair production at LEP energies above the Z resonance, *The European Physical Journal C* **45** (3) (2006) 589–632. doi:10.1140/epjc/s2005-02461-0. (page 24).
- [39] G. Abbiendi, et al., Tests of the standard model and constraints on new physics from measurements of fermion-pair production at 189-209 GeV at LEP, *The European Physical Journal C* **33** (2) (2004) 173–212. doi:10.1140/epjc/s2004-01595-9. (page 24).
- [40] M. Acciarri, et al., Search for manifestations of new physics in fermion-pair production at LEP, *Physics Letters B* **489** (12) (2000) 81 – 92. doi:http://dx.doi.org/10.1016/S0370-2693(00)00887-X. (page 24).
- [41] K. McFarland, Neutral currents and strangeness of the nucleon from the nutev experiment, *The European Physical Journal A - Hadrons and Nuclei* **24** (2) (2005) 161–164. doi:10.1140/epjad/s2005-04-041-y. (page 24).
- [42] G. Aad, et al., Search for Extra Dimensions using diphoton events in 7 TeV proton-proton collisions with the ATLAS detector, *Phys.Lett.* **B710** (2012) 538–556. arXiv:1112.2194, doi:10.1016/j.physletb.2012.03.022. (page 25).
- [43] S. Chatrchyan, et al., Search for large extra dimensions in dimuon and dielectron events in pp collisions at, *Physics Letters B* **711** (1) (2012) 15 – 34. doi:http://dx.doi.org/10.1016/j.physletb.2012.03.029. (page 25).
- [44] S. Chatrchyan, other, Search for signatures of extra dimensions in the diphoton mass spectrum at the large hadron collider, *Phys. Rev. Lett.* **108** (2012) 111801. doi:10.1103/PhysRevLett.108.111801. (page 25).
- [45] V. Abazov, et al., Search for Large extra spatial dimensions in the dielectron and diphoton channels in  $p\bar{p}$  collisions at  $\sqrt{s} = 1.96$ -TeV, *Phys.Rev.Lett.* **102** (2009)

051601. arXiv:0809.2813, doi:10.1103/PhysRevLett.102.051601. (page 25, 25).
- [46] V. M. Abazov, B. Abbott, M. Abolins, B. S. Acharya, M. Adams, T. Adams, M. Agelou, J.-L. Agram, et al., Search for large extra spatial dimensions in dimuon production with the d0 detector, *Phys. Rev. Lett.* **95** (2005) 161602. doi:10.1103/PhysRevLett.95.161602. (page 25).
- [47] M. Acciarri, et al., Search for extra dimensions in boson and fermion pair production in e+e interactions at LEP, *Physics Letters B* **470** (14) (1999) 281 – 288. doi:http://dx.doi.org/10.1016/S0370-2693(99)01310-6. (page 25).
- [48] M. Acciarri, et al., Search for low scale gravity effects in e+e collisions at LEP, *Physics Letters B* **464** (12) (1999) 135 – 144. doi:http://dx.doi.org/10.1016/S0370-2693(99)01011-4. (page 25).
- [49] P. Abreu, et al., Measurement and interpretation of fermion-pair production at LEP energies of 183 and 189 GeV, *Physics Letters B* **485** (13) (2000) 45 – 61. doi:http://dx.doi.org/10.1016/S0370-2693(00)00675-4. (page 25).
- [50] P. Abreu, et al., Determination of the e+e() cross-section at centre-of-mass energies ranging from 189 GeV to 202 GeV, *Physics Letters B* **491** (12) (2000) 67 – 80. doi:http://dx.doi.org/10.1016/S0370-2693(00)01013-3. (page 25).
- [51] L. Evans, The large hadron collider, *New Journal of Physics* **9** (9) (2007) 335. (page 27).
- [52] O. S. Brning, P. Collier, P. Lebrun, S. Myers, R. Ostojic, J. Poole, P. Proudlock, LHC Design Report, CERN, Geneva, 2004. (page 26).
- [53] Total integrated luminosity and data quality in 2011 and 2012 (2013).  
URL <https://twiki.cern.ch/twiki/bin/view/AtlasPublic/LuminosityPublicResults> (page 28).
- [54] G. Aad, et al., The ATLAS Experiment at the CERN Large Hadron Collider, *Journal of Instrumentation* **3** (2008) S08003. 437 p, also published by CERN Geneva in 2010. (pages 29, 29, 30, 30, 31, 31, 32, 34, 35, 36, 37, 38, 39, 44, 45).



- [55] Performance of the ATLAS Electron and Photon Trigger in p-p Collisions at  $\sqrt{s} = 7$  TeV in 2011, Tech. Rep. ATLAS-CONF-2012-048, CERN, Geneva (May 2012). (pages 47, 48).
- [56] Trigger operation public results (2011).  
URL <https://twiki.cern.ch/twiki/bin/view/AtlasPublic/TriggerOperationPublicResults> (page 48).
- [57] I. Antcheva, et al., ROOT a C++ framework for petabyte data storage, statistical analysis and visualization, Computer Physics Communications **180** (12) (2009) 2499 – 2512, 40 YEARS OF CPC: A celebratory issue focused on quality software for high performance, grid and novel computing architectures. doi:<http://dx.doi.org/10.1016/j.cpc.2009.08.005>. (pages 50, 81).
- [58] S. Agostinelli, et al., Geant4a simulation toolkit, Nuclear Instruments and Methods in Physics Research Section A: Accelerators, Spectrometers, Detectors and Associated Equipment **506** (3) (2003) 250 – 303. doi:[http://dx.doi.org/10.1016/S0168-9002\(03\)01368-8](http://dx.doi.org/10.1016/S0168-9002(03)01368-8). (pages 50, 62).
- [59] Number of interactions per crossing (2012).  
URL <https://twiki.cern.ch/twiki/bin/view/AtlasPublic/LuminosityPublicResults> (page 51).
- [60] G. Aad, et al., Luminosity Determination in  $pp$  Collisions at  $\sqrt{s} = 7$  TeV Using the ATLAS Detector at the LHC, Eur.Phys.J. **C71** (2011) 1630. arXiv:1101.2185, doi:10.1140/epjc/s10052-011-1630-5. (page 51).
- [61] G. Aad, et al., Electron performance measurements with the ATLAS detector using the 2010 LHC proton-proton collision data, Eur.Phys.J. **C72** (2012) 1909. arXiv:1110.3174, doi:10.1140/epjc/s10052-012-1909-1. (page 53).
- [62] Electron efficiency measurements with the ATLAS detector using the 2012 LHC proton-proton collision data, Tech. Rep. ATLAS-CONF-2014-032, CERN, Geneva (Jun 2014). (pages 58, 64).

- [63] S. Alioli, P. Nason, C. Oleari, E. Re, A general framework for implementing NLO calculations in shower Monte Carlo programs: the POWHEG BOX, *JHEP* **1006** (2010) 043. arXiv:1002.2581, doi:10.1007/JHEP06(2010)043. (page 62).
- [64] S. Alioli, P. Nason, C. Oleari, E. Re, NLO vector-boson production matched with shower in POWHEG, *JHEP* **0807** (2008) 060. arXiv:0805.4802, doi:10.1088/1126-6708/2008/07/060. (page 62).
- [65] T. Sjostrand, S. Mrenna, P. Z. Skands, A Brief Introduction to PYTHIA 8.1, *Comput.Phys.Commun.* **178** (2008) 852–867. arXiv:0710.3820, doi:10.1016/j.cpc.2008.01.036. (pages 62, 62, 71).
- [66] H.-L. Lai, M. Guzzi, J. Huston, Z. Li, P. M. Nadolsky, et al., New parton distributions for collider physics, *Phys.Rev.* **D82** (2010) 074024. arXiv:1007.2241, doi:10.1103/PhysRevD.82.074024. (pages 62, 63, 72).
- [67] R. Gavin, Y. Li, F. Petriello, S. Quackenbush, FEWZ 2.0: A code for hadronic Z production at next-to-next-to-leading order, *Comput.Phys.Commun.* **182** (2011) 2388–2403. arXiv:1011.3540, doi:10.1016/j.cpc.2011.06.008. (page 62).
- [68] A. Martin, W. Stirling, R. Thorne, G. Watt, Parton distributions for the LHC, *Eur.Phys.J.* **C63** (2009) 189–285. arXiv:0901.0002, doi:10.1140/epjc/s10052-009-1072-5. (pages 62, 63, 71, 84, 95).
- [69] A. Martin, R. Roberts, W. Stirling, R. Thorne, Parton distributions incorporating QED contributions, *Eur.Phys.J.* **C39** (2005) 155–161. arXiv:hep-ph/0411040, doi:10.1140/epjc/s2004-02088-7. (pages 62, 95).
- [70] G. Corcella, I. Knowles, G. Marchesini, S. Moretti, K. Odagiri, et al., HERWIG 6.5 release note arXiv:hep-ph/0210213. (pages 62, 63, 94, 94).
- [71] J. Pumplin, D. Stump, J. Huston, H. Lai, P. M. Nadolsky, et al., New generation of parton distributions with uncertainties from global QCD analysis, *JHEP* **0207** (2002) 012. arXiv:hep-ph/0201195, doi:10.1088/1126-6708/2002/07/012. (page 62).

- [72] J. M. Campbell, R. Ellis, MCFM for the Tevatron and the LHC, Nucl.Phys.Proc.Suppl. **205-206** (2010) 10–15. arXiv:1007.3492, doi:10.1016/j.nuclphysbps.2010.08.011. (page 63).
- [73] S. Frixione, B. R. Webber, The MC@NLO 3.4 Event Generator arXiv:0812.0770. (pages 63, 94).
- [74] J. Butterworth, J. R. Forshaw, M. Seymour, Multiparton interactions in photo-production at HERA, Z.Phys. **C72** (1996) 637–646. arXiv:hep-ph/9601371, doi:10.1007/s002880050286. (pages 63, 94).
- [75] M. Czakon, P. Fiedler, A. Mitov, Total Top-Quark Pair-Production Cross Section at Hadron Colliders Through  $O(\alpha_s^4)$ , Phys. Rev. Lett. **110** (25) (2013) 252004. arXiv:1303.6254, doi:10.1103/PhysRevLett.110.252004. (page 63).
- [76] M. Cacciari, M. Czakon, M. Mangano, A. Mitov, P. Nason, Top-pair production at hadron colliders with next-to-next-to-leading logarithmic soft-gluon resummation, Phys. Lett. **B710** (2012) 612–622. arXiv:1111.5869, doi:10.1016/j.physletb.2012.03.013. (page 63).
- [77] T. Gleisberg, S. Hche, F. Krauss, M. Schnherr, S. Schumann, F. Siegert, J. Winter, Event generation with sherpa 1.1, Journal of High Energy Physics **2009** (02) (2009) 007. (pages 72, 94).
- [78] A. Caldwell, D. Kollr, K. Krninger, BAT - The Bayesian analysis toolkit, Computer Physics Communications **180** (11) (2009) 2197 – 2209. doi:http://dx.doi.org/10.1016/j.cpc.2009.06.026. (page 81).
- [79] S. Alekhin, J. Bluemlein, S. O. Moch, ABM11 PDFs and the cross section benchmarks in NNLO, PoS **LL2012** (2012) 016. arXiv:1302.1516. (page 84).
- [80] S. G. Bondarenko, Saprionov, A. A., NLO EW and QCD proton-proton cross section calculations with mcsanc-v1.01, Comput.Phys.Commun. **184** (2013) 2343–2350. arXiv:1301.3687, doi:10.1016/j.cpc.2013.05.010. (page 84).
- [81] T. Sjstrand, S. Mrenna, P. Skands, Pythia 6.4 physics and manual, Journal of High Energy Physics **05** (2006) 026. (page 94, 94).

- [82] M. L. Mangano, M. Moretti, F. Piccinini, R. Pittau, A. D. Polosa, ALPGEN, a generator for hard multiparton processes in hadronic collisions, *JHEP* **0307** (2003) 001. [arXiv:hep-ph/0206293](#), [doi:10.1088/1126-6708/2003/07/001](#). (page 94).